universität wien

MASTERARBEIT

Titel der Masterarbeit

Narrow-band few photon filter and phase lock control for EIT with Cs in a nanofiber dipole trap

Verfasserin

Silvia B. ARROYO CAMEJO, B.Sc.

angestrebter akademischer Grad

Master of Science (M.Sc.)

While I was enrolled at the University of Vienna as a Master student and a co-registered student at the Vienna University of Technology this thesis was performed in the group of Prof. Dr. Arno Rauschenbeutel as an external thesis at the Institute of Atomic and Subatomic Physics, which is affiliated to the Vienna University of Technolgy.

University of Vienna

Vienna University of Technology

Institute of Atomic and Subatomic Physics
of the Vienna University of Technology

Vienna Center for Quantum Science and Technology

Therefore, I want to acknowledge all institutions very much for supporting and enabling this inter-institutional work!

Summary

The coherent manipulation of atomic states is both a fascinating playground for fundamental atomic physics as well as a gate to a completely new key technology in quantum sciences with good prospects. Photons are perfectly suited carriers for the long distance distribution of quantum information [1, 2, 3, 4]. However, photon-photon interactions are naturally extremely weak [5], which renders information processing and storage practically infeasible without further ado. By coherent atomic manipulation effective interactions between photons can be introduced. Specifically, the coherent effect of electromagnetically induced transparency (EIT) provides a way toward nonlinear optics at the few-photon levels [6] and thereby may possess manifold applications from the realization of photon processing quantum gates to well-directed photonic quantum information storage and revival [7].

This thesis was performed around an experiment aiming at the investigation of the optical properties of approximately $2 \cdot 10^3$ laser cooled Cesium atoms dipole trapped in the evanescent field of an optical nanofiber [8, 9]. By driving a Λ scheme in Cesium (Cs) under the influence of a control laser tuned to the $6^2S_{1/2}$ $F = 3$ to $6^2P_{3/2}$ $F' = 4$ transition, a coherently applied few photon probe signal on the $6^2S_{1/2}F = 4$ to $6^2P_{3/2}F' = 4$ transition is expected to be subject to a suppression of absorption, while experiencing a steep positive slope of the refractive index. While EIT has already been successfully demonstrated in atomic vapor cells up to room temperature and above, in dipole trapped Alkali atoms [10], in metamaterials [11], in optomechanical systems [12] and even solid state systems [13, 14], the great advantage of the setup in the Rauschenbeutel group lies in the fact, that the Cs atoms are intrinsically fiber-coupled and mode-matched to the optical nanofiber. That way, this particular system is perfectly compatible with modern optical fiber based communication technology.

This Master thesis covers two parts of the total experiment. The focus of the first part is the beam preparation of the EIT control and probe lasers which ensures a phase stable joint performance of both beams necessary for the implementation of EIT. This is achieved by an optical phase-locked loop (OPLL) locking the probe to the control laser. The latter is frequency stabilized to the respective Cs transition via a polarization spectroscopy. The performance of this OPLL which was developed in [15] is examined with an out-of-loop phase noise measurement. The performed experimental investigations prove that the residual phase noise between control and probe laser is reasonably small so that the laser system is now ready for the investigation of EIT-related phenomena in Cs atoms trapped around the nanofiber.

The second part of this thesis concerns the efficient detection of the prospective few-photon EIT probe signal, which will be immersed in a broadband noise background. The noise originates from the fluorescence induced by one of the Cs trapping laser field in the nanofiber substrate. While the weak EIT probe signal ($\leq$ pW power) is expected to be extremely narrow-band (Hz to kHz) the disturbing fluorescence signal has a power of approximately 5 pW within a wavelength window of 10 nm around the probe wavelength. Conventional optical filters fail in efficiently separating the signal from the fluorescence. Thus, in this second part two strategies are elaborated both theoretically and experimentally aiming at a reasonable solution for narrow-band few-photon filtering. One rather elementary attempt is employing a diffraction grating and taking advantage of the frequency selectiveness of diffraction. A slightly more elaborate technique involves the homodyne detection principle exploiting its high phase and amplitude sensitivity, respectively. Both options are considered and weighted up on the basis of their achievable contribution to the improvement of the signal-

to-noise ratio of the probe signal. Experimental proposals for narrow-band filters based on both options are made. These theoretical considerations are concluded by an experimental realization and analysis of a compact test setup — a homodyne saturation spectroscopy — for the purpose of testing the power of homodyne detection.

Contents

II. Experiment and Measurements 53

5. Experimental Setup and Characterization of the OPLL 55

6. Proposal for a Narrow-band Diffraction Grating Filter 67

7. Experimental Investigation of a Homodyne Saturation Spectroscopy 77

8. Outlook 91

Acknowledgments 105

1. Introduction and Motivation

Ever since the birth of quantum theory at the beginning of the 20th century the utter contrast of quantum phenomena and the classical world has intrigued many of the great minds of those days. The discovery of such genuine quantum features as the superposition principle [16], entanglement [17, 18, 19], quantum randomness [20, 21] and the impact of a measurement [22, 23] etc. not only opened the door toward fundamental new physics, but furthermore spanned a whole new world of unique possibilities for applications. While the gross formulation of quantum theory took about 30 years, actual applications based on quantum theory only slowly developed during the subsequent decades. Certainly, the invention of the laser in the sixties [24, 25] was one product of quantum theory, which has had a tremendous impact in scientific research, technology and even medicine ever after. Even more, one cannot imagine today's world without the latest advances in semiconductor and nanotechnology etc., all of which are based on quantum theory to some extent. Nonetheless, these examples seem to be just a slight hint of what is still to be realized in the near and far future.

Modern quantum optics and atomic physics experiments provide wonderful opportunities for the investigation of the interactions between matter and light. They do so with such incredibly high accuracy and precision, not even the founding fathers of quantum mechanics were keen enough to envision. Nevertheless, still much theoretical and experimental effort has to be spend until the fruits of dozens of promising proposals can be harvested, enabling massive parallel and distributed quantum computing and intrinsically secure quantum communication networks. These technologies will lead to a huge technological upheaval with big impacts on many branches of science and industry just like the invention of the computer once did.

1.1. A call for quantum memories

Quantum networks open a path toward fascinating new technologies like intrinsically secure communication via quantum cryptographic protocols [26, 27] or distributed quantum computing [28, 29] by implementing entanglement swapping [30, 31] and teleportation of quantum states [30, 32]. Photonic qubits appear most suited for the long-distance distribution of quantum states in such networks. Controlled manipulation and processing of quantum information on the contrary requires additional effort, as photons couple to each other insignificantly [5]. One solution allowing for the processing of photonic quantum information in a purely optical fashion is based on one-way cluster-state quantum computation protocols [33, 34]. Here, projective measurements lead to an effective nonlinearity. Against initial allegations it was proven theoretically that linear optics quantum computation (LOQC) is possible [35]. Experimental LOQC implementations [36, 37] still leak that feature, though, and thus its integration into distributed networks remains doubtful. But most importantly in LOQC, storage of those flying qubits is the major, still unresolved problem.

In order to achieve both strong photon-photon coupling and qubit storage devices one has to rely on the assistance of ancillary atoms, performing local operations on the qubits. In quantum networks, the generation, processing, storage of qubits is performed locally at the nodes. These nodes are linked by quantum channels, which transport quantum states from site to site distributing entanglement across the entire network. Hence, there is a strong need for what one may call a 'quantum interface' moderating between these photonic qubits on
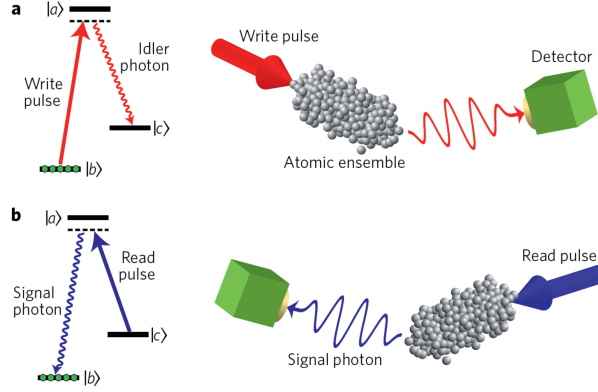
Figure 1.1.: Quantum memory based on the DLCZ-protocol (reprint from [42])

the one hand and those atomic processing and storage units on the other [38]. This interface needs to possess perfectly coherent performance in that the fragile quantum state persists over mapping it from one physical representation to the other and vice versa. Additionally, this mapping process needs to exhibit an on demand performance.

The need for reliable long time storage arises especially in the context of distributed quantum networks. Although entangled states represent an essential resource for operations in quantum networks, their generation and distribution over long distances poses one of the biggest challenges for an implementation of quantum communication protocols. This is mainly due to exponential losses of the degree of entanglement scaling with the distribution length. In practice, optical fibers allow for entanglement distribution on the scale of only $l \approx 100$ km. Furthermore, this entanglement loss cannot be fully compensated for based on genuine purification schemes [32, 39].

Notwithstanding, quantum memories would also contribute valuably to the search for a deterministic single-photon source [40, 41]. In fact, a quantum memory could transform a heralded single-photon source into a single-photon source operating on-demand and hence solve another big challenge in today's quantum technology.

1.2. Quantum memories as crucial elements for quantum repeaters

In a seminal paper by Briegel et al. in 1998 [39], the concept of the quantum repeater was introduced. This device is based on a cascaded entanglement-purification protocol in which the required overhead in communication time increases with distance only polynomially, while the number of ancillary qubits depends logarithmically on the distance. The distinguished paper by Duan, Lukin, Cirac and Zoller in 2001 furthermore illuminated in-depth how the single steps in a quantum repeater sequence can be performed on the physical basis of linear optics and atomic ensembles (DLCZ-protocol) [2]. Here, entanglement is generated by probing a Raman transition in a Λ-type level scheme in an atomic ensemble and collecting the forward-scattered Stokes photon which is entangled with the collective excitation among the atomic ensemble (see fig. 1.1a)). If two such Stokes photons from atomic ensembles of two neighboring nodes are subject to a joint Bell measurement, an entanglement between the two nodes is introduced. In a probabilistic fashion a pairwise entanglement generation between all nodes lying in the intermediate range between A and B is performed. Finally, entanglement between A and B can be realized by piecewise entanglement swapping among each segment of the quantum channel.

Though the DLCZ-protocol solves the fundamental problem, this scheme relies on an array of quantum memory devices as one essential requisite during the cascaded entanglement-

purification procedures. For the generation of entanglement between distant qubits one has to store qubits sufficiently long until — according to the DLCZ-protocol — all required joint Bell measurements between the segments in the channel have been performed and the qubits' entanglement has been proven, respectively. As all purification schemes are of probabilistic nature one afterwards has to maintain only those qubits in the chain for usage for which the qubits' entanglement could be generated and repeat the protocol for those segments were it failed. This way the necessity for a quantum memory with a preferably long storage time arises, since clearly the entanglement distribution range critically depends on the memory's storage time.

Since the proposal of the quantum repeater in [39] there is the challenge to conceptualize a system, that can store a photon state and release exactly the same state after a desirable time. Spin states of atoms are known to be reliable, long-lived representatives of quantum states. One interesting attempt to complete the job is therefore to map a photon state to a long-lived spin state and vice versa in a coherent fashion. Mapping the photon state to a collective excitation in an atomic ensemble instead of mapping it to a single atom turns out to be more promising [2, 43].

The DLCZ-protocol suggests a realization of quantum memory in a way, closely related to photon storage via electromagnetically induced transparency (EIT) [44, 43, 7]. EIT is a nonlinear optical phenomenon generically seen in atomic systems with a three-level Λ-scheme (lambda)[1]. Fundamentally, it is a phenomenon induced by an interference of different optical transition paths. While one transition is strongly driven by a control laser beam of high intensity, another weak (at the single to few photon level) probe beam — set on the opposing transition — experiences a characteristic transparency of the medium traversed, i.e. a suppression of absorption. At the same time, the probe undergoes an especially steep variation of the refractive index giving rise to extraordinary small group velocities of the probe pulse [48]. This is even possible down to a complete stop and retrieval using metastable dark-state polaritons as memory resource [49, 38]. Interestingly, in the optimized EIT-based quantum memory scheme the optical depth αL (i.e. the product of the absorbtion coefficient α and the length of the EIT medium L) is the only parameter that defines the storage efficiency [50].

Even though the DLCZ-protocol based quantum memory also uses the spin wave concept as storage resource, the collective atomic excitation is not generated by an incident single probe photon, but rather by the ensemble interacting with a classical write field, sent in on one transition of the Λ-scheme. The generation of the atomic excitation is heralded by an idler photon, emitted on the other transition of the Λ-scheme (see fig. 1.1 a). After the desired storage time, the excitation can be retrieved by the application of a classical read field in the reverse direction of the original write field so that a signal photon exits the medium on the other side (see fig. 1.1b).

In contrast to the EIT-based photon storage the DLCZ-scheme quantum memory does not directly support single-photon storage in a "plug and play" fashion. However, by exploiting quantum teleportation an equivalent 'black box quantum memory' device can be obtained [51].

---

[1]Principally, 'transparency effects' can also be observed in three-level V-schemes (vee) and Ξ-schemes (ladder). Contrary to the former common perception, recent theoretical investigations [45, 46] claim that actual EIT only appears in Λ-schemes and upper-level driven Ξ-schemes. In contrast, the similar looking, but distinct transparency effects observed in V-schemes and lower-level driven Ξ-schemes were determined to be solely due to Autler-Townes splitting [47].

1.3. Toward the realization of quantum memories

The first systematic experimental investigations of EIT were performed in cold atomic ensembles [52]. A big breakthrough was achieved in 1999 when this effect could experimentally be demonstrated to slow down the group velocity of light pulses to the value of 17 m/s [48]. Actual storage and successive retrieval of photons was accomplished in 2001 both in cold Na [53] and in hot Rb ensembles [54]. On the search for more convenient and scalable physical systems over the following years, EIT phenomena were observed in diverse many-body systems, e.g. in metamaterials [11] and optomechanical systems [12]. While most EIT attempts are based on the mapping of photon states onto collective excitations of an atomic ensemble, only recently a single-atom based quantum memory could be demonstrated in a cavity system [55]. Finally, quantum memory experiments were successfully carried out in solid-state systems [13, 14]. While these last achievements represent important steps on the way toward the actual realization of quantum networks, the efficient coupling between photon channels and matter nodes still turn out to be problematic.

In this respect, the attempt perused in the Rauschenbeutel group could prove to be an appropriate solution. The advantage of this system lies in its intrinsic compatibility to the state of the art fiber based information technology. Here, the EIT is proposed to be conducted in cold Cs atoms dipole trapped within the evanescent field of an optical nanofiber [8]. While the special geometry of the optical fiber dipole trap confines the atoms in a 1d optical lattice beaded along the nanofiber in a ~ 200 nm distance to the fiber surface the nanofiber light mode experiences a strong overlap with the Cs interaction cross section. From this perspective, this system is a promising candidate for a plug-and-play fiber coupled quantum memory.

1.4. Aim of the work performed in this thesis

On the route to the realization of an intrinsically fiber coupled quantum memory, many experimental challenges are to be solved. This thesis focuses on two parts of the total experiment. The first part of the thesis focuses on the laser beam preparation of both the EIT control and probe lasers. Since EIT relies on the coherent application of two light fields to an atomic system it is of crucial importance to ensure a phase stable performance of the control and probe laser. Within the context of this thesis, an optical phase-locked loop (OPLL) stabilizing the probe laser to the control laser had to be partly rebuilt and completely readjusted after the group's move from Mainz to Vienna in November 2010. Before, this OPLL was designed, built up and first characterized in the context of a Diplom thesis in 2010 [15]. After its reconstruction the quality of the OPLL performance had to be inspected. The quality check presented in this thesis was for the first time conducted by means of an out-of-loop measurement, i.e. an analysis of the beat signal outside of the actual phase control loop. This out-of-loop measurement is inherently more objective than an in-loop measurement, which is received observing the error signal of the phase controller. An additional, parallelly conducted in-loop measurement should enable a direct comparison between the in and out-of-loop detected signal. In order not to affect the original OPLL performance by these additional measurement setups, the latter have to access the OPLL in a minimally invasive fashion.

The second part of this thesis deals with investigations on the detection of the prospective few-photon probe field which is experiencing the transparency. In the Rauschenbeutel experiment, the EIT probe signal detection is hampered due to broad-band fluorescence light which is induced by one of the Cs trap laser field in the nanofiber substrate. A significant part of this fluorescence co-propagates spatially mode-matched with the EIT probe signal. Within

a wavelength window of ± 5 nm around the EIT resonance on the Cs D2 line at ~ 852.3 nm, both fluorescence and EIT signal have a power in the same order of magnitude (some pW). As a sufficient suppression of the fluorescence light is not realizable by means of optical filters in this regime in this thesis two possible options toward the realization of a narrow-band few to single photon filter were investigated theoretically. The first, experimentally rather easy option relies on exploiting the wavelength-dependent diffraction by a diffraction grating and subsequent spatial filtering. The second, experimentally more challenging option would be a filter based on heterodyne/homodyne detection. Here, either the frequency conversion through optical mixing and a successive narrow-band electronic filtering or the sensitive detection of the coherence properties of the signal can be employed for the purpose of a narrow-band signal detection. Both ways are theoretically investigated. For the experimental investigation of the homodyne detection principle a, homodyne saturation spectroscopy test setup is realized rounding off the theoretical investigations.

Part I.

Theory

2. Theory of Atom-Photon Interaction

2.1. Introduction to the physical basis of slow and fast light

This chapter gives an introduction to the theoretical background of the prospective EIT experiment, which is planned to be performed in the Rauschenbeutel group. After an introduction to the concepts of fast and slow light, the classical understanding of the dielectric susceptibility is established as the underlying concept behind the refractive index and absorption in dielectric media. On this basic understanding, the microscopic foundation of the dielectric susceptibility, i.e. the interaction of light with a two-level system is explored. In a subsequent discussion, an extension to a three-level system is performed, giving rise to coherent atomic features like EIT.

2.1.1. The velocity of light in media

The speed at which the wavefronts of a monochromatic beam of light with frequency ω move through a material is given as the phase velocity

$$v_{ph}(\omega) = \frac{\omega}{k} = \frac{c}{n} \ , \tag{2.1}$$

with the norm of the wave vector $k = |\vec{k}|$ and the refractive index n. A realistic light wave, however, has a finite pulse duration, i.e. it is a finite wave train and therefore necessarily has a finite spectral width. Composed of an infinite number of monochromatic wave components with varying weights $A(k)$, the shape and location of the envelope of a wave packet

$$u(x,t) = \frac{1}{\sqrt{2\pi}} \int_{-\infty}^{+\infty} A(k) e^{i(kx - \omega(k)t)} \mathrm{d}k \tag{2.2}$$

is determined by constructive and destructive interference among the wave's components. When the pulse propagates through a material system, each mode travels at a specific $v_{ph}(\omega)$ in accordance with the wavelength dependance of the refractive index $n(\omega)$. This results in a shift of the regions of constructive and destructive interference, if compared to propagation in vacuum, and eventually leads to pulse distortion. In the case of sufficiently short propagation distances however, the effect of pulse distortion can be considered to be small [56, 57]. Then the propagation velocity of the pulse with the central frequency ω_{g_0} is described by the group velocity

$$v_g(\omega_{g_0}) = \left.\frac{\mathrm{d}\omega}{\mathrm{d}k}\right|_{\omega=\omega_{g_0}} = \frac{c}{n_g} = \frac{c}{n(\omega_{g_0}) + \omega \left.\frac{\mathrm{d}n(\omega)}{\mathrm{d}\omega}\right|_{\omega=\omega_{g_0}}} \tag{2.3}$$

with the group refractive index

$$n_g(\omega_{g_0}) = n(\omega_{g_0}) + \omega \left.\frac{\mathrm{d}n}{\mathrm{d}\omega}\right|_{\omega=\omega_{g_0}} . \tag{2.4}$$

In the vast majority of situations, the group velocity is most closely related to the signal velocity of information. Conventionally, the labeling 'slow' and 'fast' light refer to the group velocity of a light wave. In these terms, slow light corresponds to the regime with $v_g \ll c$,

whereas fast light denotes the regime with $v_g \gg c$. Furthermore, in very special cases, a negative index of refraction can be realized, which gives rise to so called backwards light with $v_g < 0$ [58, 59]. For these extreme cases, were v_g approximates or exceeds the vacuum light velocity and for negative v_g, the equivalence between the group velocity and the velocity of information brakes [60, 61, 62, 57, 63]. Extreme values of the group velocity, far off the velocity of light in vacuum are mainly due to the contribution of the second term in eq. (2.4), i.e. the dispersive response of the material, which results from the frequency dependence of the refractive index. It is for this reason that extreme values of the group velocity are usually associated with the resonant or near-resonant response of material systems.

2.2. Classical approach to the dielectric susceptibility as the origin of the refractive index

In order to investigate the frequency dependence of the refractive index, the origin of the refractive index in matter has to be explored. The physical basis for the refractive index of a material lies in the dielectric polarizability α_e of its constituents. The polarizability, normally expressed by the dielectric susceptibility $\tilde{\chi} = \alpha_e/\epsilon_0$ can be seen as the mediating prefactor between the incident electric field $\vec{E}$ and the polarization $\vec{P}$, representing the response of the material to the applied electric field. The first order susceptibility

$$\vec{P} = N\alpha_e\vec{E} = N\epsilon_0\tilde{\chi}\vec{E} \tag{2.5}$$

epitomizes the linear response of the medium. Here, N stands for the number of oscillators per unite volume. The dielectric susceptibility likewise represents the dielectric polarizability of any material and generally is a complex quantity

$$\tilde{\chi} = \chi' + i\chi'' \ . \tag{2.6}$$

The characteristic form of the susceptibility of conductors differs dramatically from that one of dielectric materials [64]. This distinct deviation is due to an additional term in Maxwell's equations for conductors, which accounts for the displacement current. In this treatment, however, the susceptibility of dielectrics is to be considered only. Indeed, gaseous ensembles of few metal atoms can be treated as genuine dielectrics as their conductive properties emerge only in bulk.

Lorentz model of the classical dielectric susceptibility

By definition, a dielectric is an electrical insulator. While the term "insulator" refers to a low degree of electrical conduction, the term "dielectric" is typically used to describe materials with a high polarizability (expressed through the dielectric constant). By the application of an external electric field to a dielectric, the negatively charged electrons and oppositely charged nuclei are spatially displaced and a dipole moment is generated. (To simplify matters media with polar molecules are neglected here.) Practically, the nuclei can be considered quasi-static and much heavier than the electrons. The susceptibility is then determined by the characteristic motion of electrons forced by and as a response to the external electric field $\vec{E}(t)$. The according equation of motion of the electrons — denoted as the Lorentz oscillator model — reads [64]

$$m_e\ddot{\vec{x}} + m_e\Gamma\dot{\vec{x}} + m_e\omega_0^2\vec{x} = -e\vec{E}(t) \ , \tag{2.7}$$

with a mass dependent acceleration term, a phenomenological damping constant Γ in the velocity term and a restoring force term determined by the resonance frequency ω_0. For an
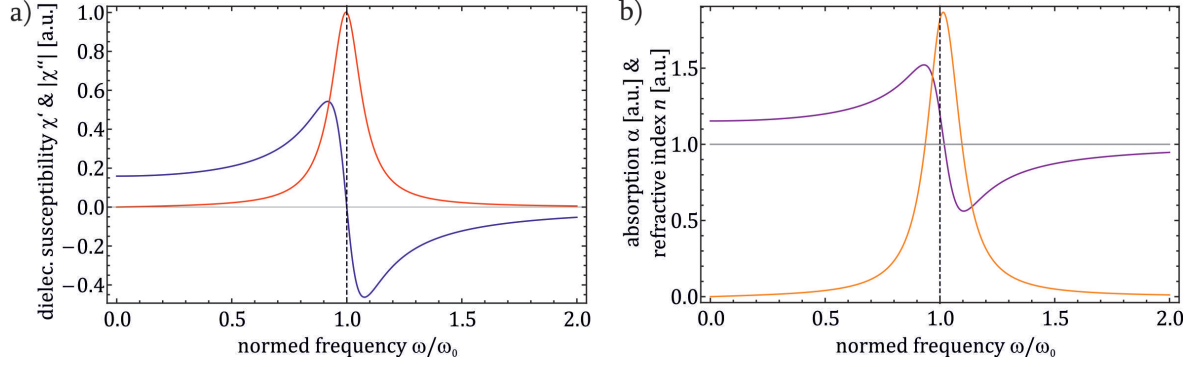
Figure 2.1.: a) Dielectric susceptibility χ' (blue) and χ'' (red) and b) Dielectric refractive index n (purple) and absorption κ (orange)

oscillating electric field $\vec{E}(t) = \vec{E}(\omega)e^{i\omega t}$ the stationary solution for the equation of motion (2.7) is

$$\vec{x}(\omega) = \frac{-e}{m_e} \frac{1}{(\omega_0^2 - \omega^2) + i\omega\Gamma} \vec{E}(\omega) \ . \tag{2.8}$$

The polarization $\vec{P}(\omega)$ results as the response of the material to an external electric field $\vec{E}(\omega)$, which couples to the dipoles $\vec{d} = e\vec{x}$ in the material:

$$\vec{P}(\omega) = \frac{Ne^2}{m_e} \frac{1}{(\omega_0^2 - \omega^2) + i\omega\Gamma} \vec{E}(\omega) \ . \tag{2.9}$$

The proportionality factor between the incident electric field and the material response contains the dielectric susceptibility

$$\tilde{\chi}(\omega) = \frac{Ne^2}{\epsilon_0 m_e} \frac{1}{(\omega_0^2 - \omega^2) + i\omega\Gamma} \tag{2.10}$$

with the real and imaginary parts

$$\chi'(\omega) = +\frac{Ne^2}{\epsilon_0 m_e} \frac{(\omega_0^2 - \omega^2)}{(\omega_0^2 - \omega^2)^2 + \omega^2\Gamma^2} \tag{2.11}$$

$$\chi''(\omega) = -\frac{Ne^2}{\epsilon_0 m_e} \frac{\omega\Gamma}{(\omega_0^2 - \omega^2)^2 + \omega^2\Gamma^2} \ . \tag{2.12}$$

In fig. 2.1 both χ' (blue) and $|\chi''|$ (red) are displayed on a characteristically normalized frequency axis ω/ω_0. The obvious asymmetry of χ' regarding ω_0 is due to a distinct oscillatory behavior in the different frequency regimes. While for $\omega \gg \omega_0$ light cannot excite the oscillator, far red detuned beams $\omega \ll \omega_0$ manage to couple to the oscillators to some extent, giving evidence of the finite static polarizability $P(\omega = 0) = \frac{Ne^2}{m_e}$.

From the dielectric susceptibility two very fundamental properties characterizing the propagation of electromagnetic waves in a medium can be extracted: these are the index of refraction n and the extinction coefficient κ, which is closely related to the absorption coefficient α. It is convenient to introduce the complex index of refraction [64]

$$\tilde{n} = n - i\kappa = \sqrt{1 + \tilde{\chi}} = \sqrt{\epsilon' + i\epsilon''} \tag{2.13}$$

with the complex permittivity

$$\tilde{\epsilon} = 1 + \tilde{\chi} = \epsilon' + i\epsilon'' \ . \tag{2.14}$$

The real part of the complex refractive index n indicates the phase velocity (i.e. the propagation velocity of a monochromatic wave) while κ represents the amount of absorption when

11

the electromagnetic wave propagates through the material. Both n and κ are dependent on frequency and follow as

$$n(\omega) \;=\; \sqrt{\frac{1}{2}\left(\sqrt{\epsilon'^2 + \epsilon''^2} + \epsilon'\right)} \tag{2.15}$$

$$\kappa(\omega) \;=\; \sqrt{\frac{1}{2}\left(\sqrt{\epsilon'^2 + \epsilon''^2} - \epsilon'\right)} \;. \tag{2.16}$$

In the practically frequent case where n and κ are both small, their relations to ϵ' and ϵ'' reduce to

$$n(\omega) \;\xrightarrow{\kappa \ll 1}\; \sqrt{\epsilon'} \tag{2.17}$$

$$\kappa(\omega) \;\xrightarrow{n \simeq 1}\; -\frac{\epsilon''}{2n} \;. \tag{2.18}$$

Taking this into account, in the literature oftentimes χ' and χ'' are denominated as refractive index and extinction coefficient themselves, respectively.

By inserting the z-component of complex wave vector $\tilde{k} = \tilde{n}\omega/c$ into the electromagnetic wave, the meaning of its real and complex component are visualized

$$\vec{E}(z,t) = \vec{E}_0 e^{i(\tilde{k}z - \omega t)} = \vec{E}_0 e^{i(nz\omega/c - \omega t)} e^{-\kappa z \omega/c} \;. \tag{2.19}$$

The refractive index acts as a wave retarder and the extinction coefficient as an exponential damping to the wave amplitude. The absorption coefficient

$$\alpha = 2\kappa k_0 = \frac{2\kappa\omega}{c} \tag{2.20}$$

then defines a penetration depth l after which the wave intensity [64]

$$I(x) = I(0)e^{-\alpha x} \tag{2.21}$$

has been reduced to $1/e$ of its original value.

2.3. Controlling light with atoms

In the previous sections, the first-order susceptibility was introduced as the response of a medium to the coupling of a continuous electromagnetic wave to the materials dipolar oscillators. In this section, it is shown how the dispersive properties of an atomic system can be modified by optical manipulation of the atomic system. The coherent optical preparation of atomic ensembles brings about new interesting effects, e.g. the non-linear optical effects of electromagnetically induced transparency.

2.3.1. Rabi oscillations in two-level systems

In the simple case of a two level system (e.g. represented by to atomic energy levels $|g\rangle$ and $|e\rangle$ see fig. 2.2a)) driven on its resonance at ω_0 by a monochromatic laser beam with frequency ω the coherent evolution gives rise to an oscillatory population transfer between both levels. Here, we want to give a short overview of the Rabi model [65, 66] which beautifully describes this population oscillation. Starting with the time dependent Hamiltonian of the joint atom-field system

$$H(t) = H_0 + H_{int}(t) \;, \tag{2.22}$$
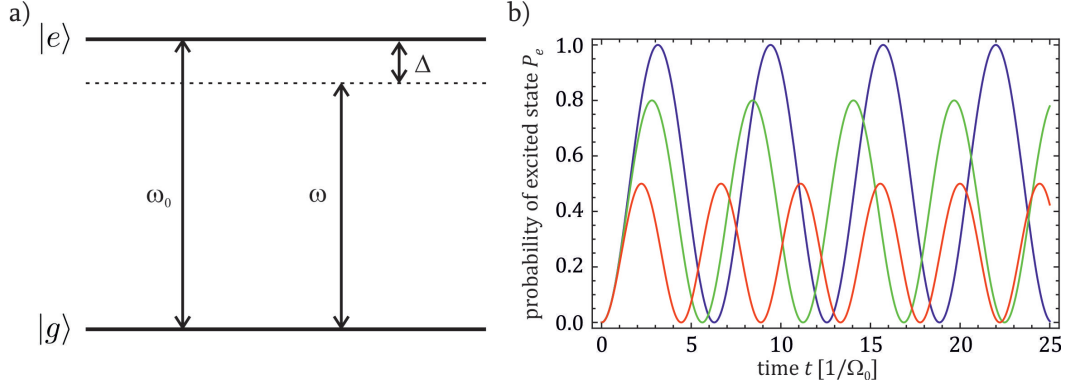
Figure 2.2.: a) Scheme of a two-level system (ω_0: resonance frequency, ω: laser frequency, $\Delta = \omega_0 - \omega$: detuning from resonance) and b) Rabi oscillations of the excited state population for different ratios $\Delta/\Omega_0 = 0.0$ (blue curve), $\Delta/\Omega_0 = 0.5$ (green curve) $\Delta/\Omega_0 = 1.0$ (red curve).

consisting of the time independent free atom Hamiltonian

$$H_0 = \frac{1}{2}\hbar\omega_0\big(|e\rangle\langle e| - |g\rangle\langle g|\big) \tag{2.23}$$

and the time-dependent interaction Hamiltonian of the atom plus light field

$$H_{int}(t) = -\vec{d}\cdot\vec{E}_0\cos\omega t \;, \tag{2.24}$$

where $\vec{d}$ is the dipole moment operator of the atom and $\vec{E}_0$ the electric field amplitude. Solving the time-dependent Schrödinger equation

$$i\hbar\frac{\partial|\psi(t)\rangle}{\partial t} = H(t)|\psi(t)\rangle \tag{2.25}$$

with the ansatz

$$|\psi(t)\rangle = c_g(t)e^{-i\omega_g t}|g\rangle + c_e(t)e^{-i\omega_e t}|e\rangle \tag{2.26}$$

where the coefficients $c_g(t)$ and $c_e(t)$ are time dependent and $\omega_0 = \omega_e - \omega_g$, results in a coupled set of equations describing the population of both levels:

$$\dot{c}_g = \frac{i}{\hbar}\langle g|\vec{d}\cdot\vec{E}_0|e\rangle\cos\omega t\; e^{-i\omega_0 t}c_e \;, \tag{2.27}$$

$$\dot{c}_e = \frac{i}{\hbar}\langle e|\vec{d}\cdot\vec{E}_0|g\rangle\cos\omega t\; e^{+i\omega_0 t}c_g \;. \tag{2.28}$$

According to the rotating wave approximation (RWA) the fast oscillating terms in the exponential expansion of the cosine in eqns. (2.27) and (2.28) can be neglected so that

$$\dot{c}_g = \frac{i}{2\hbar}\langle g|\vec{d}\cdot\vec{E}_0|e\rangle e^{+i(\omega-\omega_0)t}c_e \tag{2.29}$$

$$\dot{c}_e = \frac{i}{2\hbar}\langle e|\vec{d}\cdot\vec{E}_0|g\rangle e^{-i(\omega-\omega_0)t}c_g \;. \tag{2.30}$$

For the sake of simplicity and without loss of generality the ground state can be assumed to be fully occupied $c_g(0) = 1$ and $c_e(0) = 0$ at time $t = 0$. By eliminating c_e the following differential equation is obtained:

$$\ddot{c}_g - i(\omega - \omega_0)\dot{c}_g + \frac{\langle(\vec{d}\cdot\vec{E}_0)^2\rangle}{4\hbar^2}\,c_g = 0 \;. \tag{2.31}$$
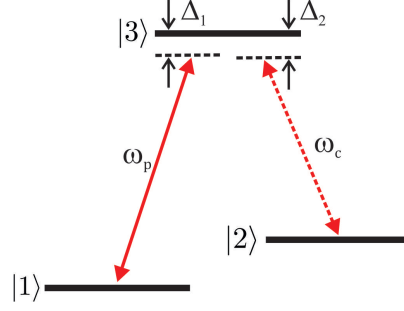
Figure 2.3.: Scheme of a three-level system. The applied fields and their detunings from the resonances are denominated.

The Rabi frequency Ω_0 is defined via $\Omega_0^2 = \langle (\vec{d} \cdot \vec{E}_0)^2 \rangle / \hbar^2$.
By solving eq. (2.31) one gets the solutions for the rates as follows:

$$c_e(t) = e^{-i\Delta t/2} \frac{i}{\hbar \Omega_R} \langle e|\vec{d} \cdot \vec{E}_0|g \rangle \sin(\Omega_R t/2) \tag{2.32}$$

$$c_g(t) = e^{-i\Delta t/2} \Big(\cos(\Omega_R t/2) + i\frac{\Delta}{\Omega_R} \sin(\Omega_R t/2) \Big) . \tag{2.33}$$

with the generalized Rabi frequency

$$\Omega_R = \sqrt{\Delta^2 + \Omega_0^2} \tag{2.34}$$

and $\Delta = \omega_0 - \omega$. For an increase of the detuning Δ from resonance the Rabi oscillations get faster and become smaller in amplitude (i.e. for $\Delta \neq 0$ the oscillations do not go all the way up to the purely excited state). The probability that the population is in state $|e\rangle$ at time t is given by

$$P_e(t) = |c_e(t)|^2 = \frac{\Omega_0^2}{\Omega_R^2} \sin^2(\Omega_R t/2) \tag{2.35}$$

as one may immediately verify by eq. (2.32). An illustration of the time dependence of $P_e(t)$ for different values of the detuning Δ is shown in fig. 2.2b).
Note, that these expressions were derived in a semiclassical picture. In eq. (2.24) the electromagnetic field was assumed to be sufficiently strong to operate in the classical regime. For the case of very low photon numbers, however, a full quantum mechanical calculation is necessary [66]. Taking field quantization into account basically results in a photon number dependent quantum Rabi frequency $\Omega_R(n)$ [67].
Note, that spontaneous emission has not been taken into account so far. Each spontaneous emission event will eventually lead to a disruption of the respective Rabi cycle and enforce an instantaneous "reset" of the atom to the ground state, followed by the start of a new Rabi cycle. Thus, spontaneous emission will introduce a dephasing of the collective Rabi oscillations in an atomic ensemble (decoherence).

2.3.2. Coherent optical manipulation of three-level systems and EIT

Expanding the two-level Rabi model to a coherently driven three-level system introduces a new stage of complexity with two additional degrees of freedom. Now — as depicted in fig. 2.3 — there are two driving fields independently tunable in intensity and frequency detuning from resonance. The coherent manipulation of this three-level scheme gives rise to a wide range of new phenomena such as Autler-Townes splitting [47], coherent population trapping (CPT) [68, 69, 70], stimulated Raman adiabatic passage (STIRAP) [71, 72], lasing without inversion

(LWI) [73, 74, 75] and electromagnetically induced transparency (EIT) [44, 43, 7], all of which are different manifestations of the same physical concept and closely related to each other. The prominent Λ-type three-level system depicted in fig. 2.3 shows the two lower states $|1\rangle$ and $|2\rangle$ which are supposed to be long-lived and represent a dipole forbidden transition. These states are coupled to the meta-stable upper state $|3\rangle$ via two electromagnetic fields, the control field ω_c and the probe field ω_p with a detuning Δ_1 and Δ_2 to the resonances at $\omega_{31} = \omega_3 - \omega_1$ and $\omega_{32} = \omega_3 - \omega_2$. For generic EIT, the fields ω_p and ω_c are applied resonant to the respective transitions, while for Raman-type schemes (as desired in the DLCZ-protocol [2]) the fields have large detunings from the atomic transition frequencies ω_{13} and ω_{23} [76]. The name electromagnetically induced transparency (EIT) originally introduced by Harris et al. in 1990 [44] refers to a quantum interference effect in which the absorption of a weak probe laser beam resonant with a two-level system is suppressed by the simultaneous application of another laser beam of much higher intensity denoted as the control beam. While CPT refers to a modification of the material states in an optically thin sample, EIT on the contrary is specifically observed only in optically dense samples and comes along with a modification of both the material states and the optical fields (EIT) [7].

In a rotating frame (after RWA), the light-matter interaction is described by the three state Hamiltonian [7]

$$H_{\text{int}} = -\frac{\hbar}{2} \begin{pmatrix} 0 & 0 & \Omega_p \\ 0 & -2(\Delta_1 - \Delta_2) & \Omega_c \\ \Omega_p & \Omega_c & -2\Delta_1 \end{pmatrix} \tag{2.36}$$

with the probe laser Rabi frequency Ω_p and control laser Rabi frequency Ω_c. For $\Delta = \Delta_1 = \Delta_2$ the eigenstates of this system written by means of the bare atom states appear as

$$
\begin{align}
|\psi^+\rangle &= \sin\theta\sin\phi|1\rangle + \cos\theta\sin\phi|2\rangle + \cos\phi|3\rangle \tag{2.37} \\
|\psi^0\rangle &= \cos\theta|1\rangle + \sin\theta|2\rangle \tag{2.38} \\
|\psi^-\rangle &= \sin\theta\cos\phi|1\rangle + \cos\theta\cos\phi|2\rangle - \sin\phi|3\rangle \tag{2.39}
\end{align}
$$

with the two mixing angles

$$
\begin{align}
\theta &= \arctan\left(\Omega_p/\Omega_c\right) , \tag{2.40} \\
\phi &= \frac{1}{2}\arctan\left(\sqrt{\Omega_p^2 + \Omega_c^2}/\Delta\right) . \tag{2.41}
\end{align}
$$

While the $|\psi^0\rangle$ state remains at zero energy, the states $|\psi^+\rangle$ and $|\psi^-\rangle$ are shifted by

$$\hbar\omega^\pm = \frac{\hbar}{2}\left(\Delta \pm \sqrt{\Delta^2 + \Omega_p^2 + \Omega_c^2}\right) \tag{2.42}$$

due to the application of the control field [7]. These new states in eq. (2.37) to eq. (2.39) are referred to as dressed states [77]. Most remarkably, $|\psi^0\rangle$ does not possess any contribution from level $|3\rangle$ and thus neither an excitation to nor emission from the upper level is possible:

$$\langle 3|H_{\text{int}}|\psi^0\rangle = 0 . \tag{2.43}$$

For this reason, $|\psi^0\rangle$ is called dark state. This dark state represents a stationary, non-radiatively decaying quantum state. Hence, it is the aim of EIT-based quantum memories to transfer a photonic qubit into such a dark state followed by an on-demand retrieval [53, 54]. The transition from a photonic excitation to a spin excitation in an atomic ensemble bringing about a dramatically reduced propagation velocity is most accurately described by the full quantum mechanical treatment via second quantization [38]. Here, the existence of a quasiparticle representing a mixture of electromagnetic and collective atomic excitations
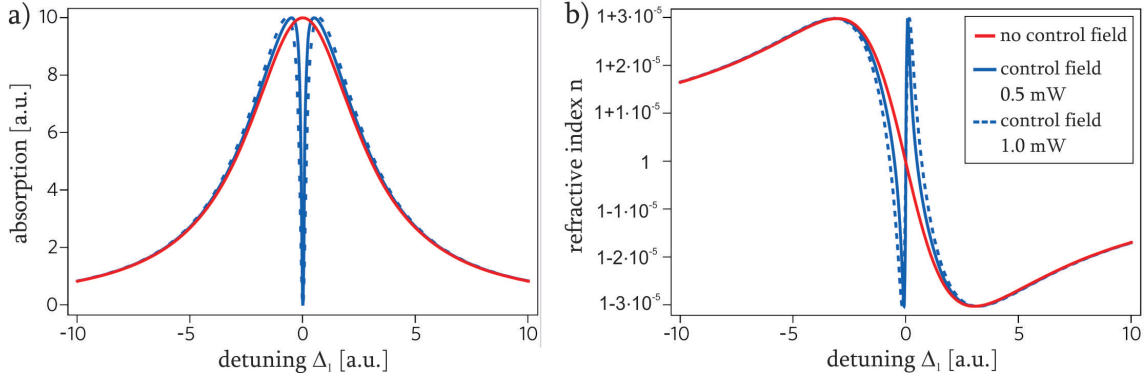
Figure 2.4.: Characteristic theoretical frequency dependence of a) the absorptive and b) the refractive properties on a normal atomic resonance (red line) and an atomic transition featuring EIT (modified; original from [42])

called dark state polaritons is predicted. The mixing angle determines the effective group velocity of that dark state polariton and can be seen as a representation of the dielectric susceptibility, which is directly dependent on the applied control field. As an illustration of the observed modification of the dispersive properties in an EIT medium, fig. 2.4 shows a) the absorption and b) the refractive index on both a normal resonance (red line) and an EIT resonance (blue lines). The narrow-band suppression of absorption on resonance shown in fig. 2.4a) is characteristic for EIT due to the missing coupling of the dark state to the upper level $|3\rangle$. This dramatic modification of the absorption is accompanied by a steep positive slope of the refractive index as displayed in fig. 2.4b), giving rise to low group velocities of the probe pulse.

Thus, at the heart of (virtually all) storage schemes lies the mapping of a photon state $|\psi\rangle_{\mathrm{ph}}$ to the collective excitation of an ensemble of N atoms with state $|\psi\rangle_{\mathrm{ae}}$. The joint state thus undergoes the trapping procedure [43]

$$|\Psi\rangle = |\psi\rangle_{\mathrm{ph}}|\psi\rangle_{\mathrm{ae}} = |1\rangle|g_1,\ldots g_N\rangle \ \longrightarrow \ |0\rangle\sum_{i=1}^{N}|g_1,\ldots,s_i,\ldots,g_N\rangle \qquad (2.44)$$

with the single photon state $|1\rangle$, the vacuum state $|0\rangle$, the atomic ground state $|g_i\rangle$ and flipped spin state $|s_i\rangle$ of the i-th atom. The advantage of such collective spin excitations states lies in their robustness against decoherence and particle loss compared to single-atom storage or other kinds of collectively excited entangled states, as e.g. GHZ states [43].

2.4. Controlling atoms with light

One of the most important advances in the field of atomic physics was the discovery of optical dipole forces and their utility for the optical manipulation, trapping, and even cooling of atoms. Even beyond atomic physics this technique — called optical tweezers [78] — became an indispensable tool for the optical manipulation and investigation of small objects in biochemistry, biophysics and biomedicine [79, 80, 81, 82].

In 1978 Ashkin reported a technique for the trapping of atoms by means of the pressure exerted by the application of resonance radiation [83]. About ten years later Chu et al. observed the first successful trapping of a laser cooled Sodium atom [84]. In this section a very short review of the principle underlying these techniques shall be given.

An electromagnetic field $\vec{E}$ of intensity I inducing a dipole moment $\vec{d}$ in an atomic system
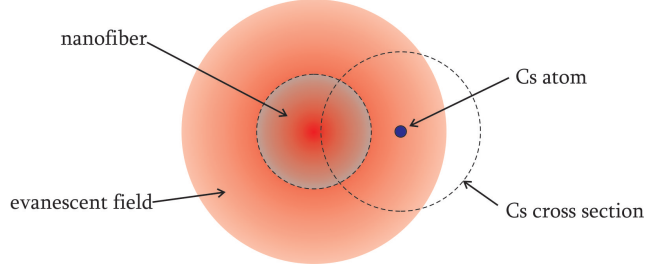
Figure 2.5.: Scheme of a Cs atom's cross section in the evanescent field around an optical nanofiber.

gives rise to the interaction dipole potential [85]

$$U_{\text{dipole}} = -\frac{1}{2}\langle \vec{d}\vec{E}\rangle = -\frac{1}{2c}\mathfrak{Re}\{\tilde{\chi}\}I \tag{2.45}$$

with the complex dielectric susceptibility $\tilde{\chi}$ and the speed of light in vacuum c (the brackets $\langle\ldots\rangle$ denote the vacuum expectation value). If the field intensity is spatially not homogeneous, i.e. if $I = I(\vec{r})$ then the resulting gradient of the dipole potential $U_{\text{dipole}}(\vec{r})$ brings about a dipole force [85]

$$\vec{F}_{\text{dipole}}(\vec{r}) = -\nabla U_{\text{dipole}}(\vec{r}) = \frac{1}{2c}\mathfrak{Re}\{\tilde{\chi}\}\nabla I(\vec{r}) \ . \tag{2.46}$$

This force results from the dispersive properties of the dipole moment mediated by the real part of the dielectric susceptibility. For a normal refractive index profile around an atomic resonance (i.e. $n > 1$ for $\omega < \omega_0$ and $n < 1$ for $\omega > \omega_0$), the dipole force is attractive for $\omega < \omega_0$ and repulsive for $\omega > \omega_0$. As a result, atoms with a resonance at ω_0 will be attracted to intensity maxima of a red detuned light field ($\omega < \omega_0$) and pushed toward intensity minima of a blue detuned light field ($\omega > \omega_0$).

In virtue of the dipoles' absorptive properties represented by the imaginary part of the dielectric susceptibility, another force — the so called scattering force — is introduced. It arises due to the scattering rate [85]

$$\Gamma_{\text{scattering}}(\vec{r}) = \frac{1}{2\hbar c}\mathfrak{Im}\{\tilde{\chi}\}I(\vec{r}) \tag{2.47}$$

and is attributed to an effective momentum transfer to the dipole due to the non-equilibrium between directed absorption and the undirected nature of spontaneous emission in the presence of a field intensity $I(\vec{r})$.

If the spatial gradient of the light intensity and the light detuning are appropriately tuned, it is possible to design atomic traps of diverse geometries. One very interesting dipole trap design is based on optically detuned modes of an optical nanofiber [86, 87, 9]. For a suitably chosen nanofiber diameter, the large evanescent field around an optical nanofiber is ideal for both trapping atoms and investing the optical properties of those atoms due to the large interaction cross section between the probing light and the atomic cross section as displayed in fig. 2.5. The two-color fiber optical atom trap employed in the Rauschenbeutel nanofiber experiment is explained more detailed in sec. 5.1.

3. Phase and Frequency Stabilization of Lasers

In this chapter, an overview on the phase and frequency stabilization of lasers is given. Following a short introduction to the basic elements of control theory, a technique for laser stabilization to a given optical transition is presented. Two possible strategies–phase and frequency stabilization–are outlined and their differences are explained. The chapter concludes by giving an objective criterion for the evaluation of control loop performance.

3.1. Introduction to control theory

There are many effects that may lead to a time dependent variation of frequency in lasers. Some are due to experimental insufficiencies, others due to fundamental physical processes. However, regardless of their origin, these variations in frequency need to be accounted for in order to perform high precision experiments in quantum optics. Here, control theory [88, 89, 90, 91] offers a systematic approach, providing the means to stabilize certain quantities in an experimental setup (e.g. the spatial distance between two cavity mirrors, or the injection current running through a laser diode).

At the heart of any stabilizing control lies the control loop depicted in fig. 3.1. In this context, the physical state of the system $x(t)$ which is to be stabilized is generally referred to as the control variable, and its desired value x_{set} as the set point. Any external disturbance, denoted by $z(t)$, will cause a deviation of the control variable from the set point. The controller first measures the control variable $x(t)$ and translates it into an actual value $\tilde{x}(t)$[1]. Afterwards the comparator generates the difference between the actual value and the externally provided set value, i.e. the so called error signal

$$\tilde{e}(t) = \tilde{x}_{\text{set}} - \tilde{x}(t) \ . \tag{3.1}$$

This error signal is then amplified by the controller's gain factor a_c and sent back to the physical system to form the actuating variable

$$y(t) = a_c \tilde{e}(t) \ . \tag{3.2}$$

The sum over actuating variable and disturbance value iteratively leads to a stabilization of the control variable of the physical system

$$x(t) = a_s(y(t) + z(t)) \tag{3.3}$$

toward the set point. Here, the factor a_s represents the characteristic transfer function of the physical system. The more the command action $\partial x / \partial x_{\text{set}}$ approaches 1, the better the stabilization of the control value $x(t)$ becomes. Therefore, the total control loop gain

$$g = a_c a_s = \frac{\partial \tilde{x}}{\partial(\tilde{x}_{\text{set}} - \tilde{x})} \tag{3.4}$$

---

[1]For the sake of clarity we will in the following highlight all electronic quantities inside the controller with a tilde "$\tilde{\cdot\cdot}$".
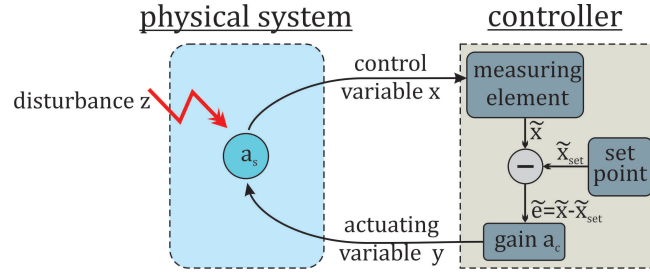
Figure 3.1.: General scheme of a control loop

should ideally be made as big as possible by choosing a_c appropriately. However, each control element entails an inevitable, frequency dependent phase shift on the signal. The specific form of the phase response is characteristic for each controller type (e.g. P, I or D controller or their combinations [88]) and is most suitably displayed in a Bode plot. In general, the higher the loop amplification gets, the bigger the phase shift between the actual value and actuating value of the degenerative feedback at fixed frequency (see e.g. [88] sec. 5.2.7 and ch. 22). At a certain threshold phase shift the negative feedback from the controller turns into a positive feedback leading the control loop to resonant oscillation. A phase shift of 180° between the physical system phase $\phi_s(f)$ (i.e. the control loop input phase) and the control loop output phase $\phi_c(f)$ in combination with a loop gain $g = 1$ ends in an effective resonance disaster. The frequency at which the loop gain approaches 1 is called the critical frequency f_{cr}. At this point, the characterizing parameter called phase margin

$$\phi_{\mathrm{margin}} = 180° - |\phi_g(f_{cr})| = 180° - |\phi_c(f_{cr}) + \phi_s(f_{cr})| \tag{3.5}$$

is defined. It is specific to each controller type and indicates the "phase buffer" remaining between the feedback phase shift $\phi_g(f_{cr})$ and the critical value of 180°. For ϕ_{margin} approaching 0° positive feedback is reached. Each controller type features a different characteristic phase response and therefore an intricate combination of different controller types will eventually lead to a reasonable compromise between loop gain, phase margin and a reasonable transient response.

3.2. Frequency stabilization of lasers

A large number of experiments in atomic physics require a precise frequency stabilization of a laser either directly onto an optical atomic transition or to a stable reference cavity. There exists a manifold of effects which cause the frequency and phase of a laser to vary over time. Some of which are of fundamental physical nature others are due to experimental insufficiencies. One obvious source are mechanical vibrations on the optical table or sound waves in the air, which have to be damped passively as well as possible. In some cases, it is — in excess of a appropriately damped optical table — necessary to isolate the laser case from sound waves, e.g. through a box lined with foamed plastic. Other noise sources can be more specific to the nature of the chosen laser type.

In the following, the three main paths toward frequency tuning and stabilization of diode lasers are explored. The necessary steps to ensure a reliable performance are described.

3.2.1. Frequency stabilization via injection current and temperature control

In terms of frequency stabilization, diode lasers have proven to be especially practical. Due to the underlying physics regarding the generation of inversion at the semiconductor junction,
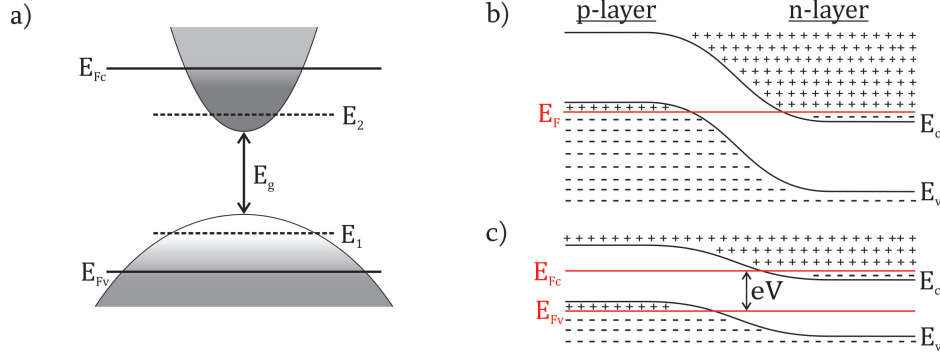
Figure 3.2.: Occupancies of the a) semiconductor band structure (bright shading: low electron occupancy; dark shading: high electron occupancy) b) diode band structure in equilibrium and c) with an applied voltage eV

diode lasers provide both an option for frequency fine-tunability and deliver easy access to frequency stabilization against short term fluctuation by controlling the injection current.

In order to obtain a stable frequency performance, this requires a meticulous control of that variable. The carrier density is proportional to the diode's injection current. Thus, inevitable rapid fluctuations of the diode injection current change the carrier density on small time scales. This in turn modifies the diode's gain, which is directly dependent on the occupancy of the valence and conduction bands [92]. Ultimately, this gives rise to an unwanted modulation of the laser frequency, which has to be compensated for by means of a dedicated current controller.

Furthermore, a direct temperature control of a laser diode is indispensable. Thermal short term fluctuations and long term drifts in the semiconductor material lead to frequency deviations in three ways. First, the thermally induced volume change of the diode material leads to a variation of the laser cavity lengths, directly changing the lasing wavelength. Second, due to the temperature dependance of the refractive index itself the effective optical length of the cavity is changed by temperature variations of the material (see e.g. [93] for Si and Ge). Third, the Fermi-Dirac distribution of the charge carriers in the semiconductor bands varies with temperature giving rise to a modified occupancy of the valence and conduction band

$$f_v(E_1) = \frac{1}{e^{(E_1 - E_{F_v})/(k_B T)} + 1} \qquad f_c(E_2) = \frac{1}{e^{(E_2 - E_{F_c})/(k_B T)} + 1} \; , \qquad (3.6)$$

respectively (E_1 denotes an unoccupied valence band level, while E_2 represent an occupied level in the conduction band and $E_{F_{v,c}}$ are the valance and conduction band's Fermi energy). In fig. 3.2a) an illustration of the bands occupancy and the corresponding denominations are given. The photon emission frequency defined by [94]

$$\hbar \omega = E_g + \frac{\hbar^2 k^2}{2m_e^*} + \frac{\hbar^2 k^2}{2m_h^*} \qquad (3.7)$$

(with the the effective electron and hole masses m_e^* and m_e^*) lies according to the Bernard-Duraffourg condition [95]

$$E_{F_c} - E_{F_v} > \hbar \omega > E_g \qquad (3.8)$$

between the energy difference of the valence and conduction band's Fermi levels and the gap energy E_g (see fig. 3.2c)). The net transition rates between the two bands is given by

$$R = R_{ij}(f_c(1 - f_c)) \; , \qquad (3.9)$$
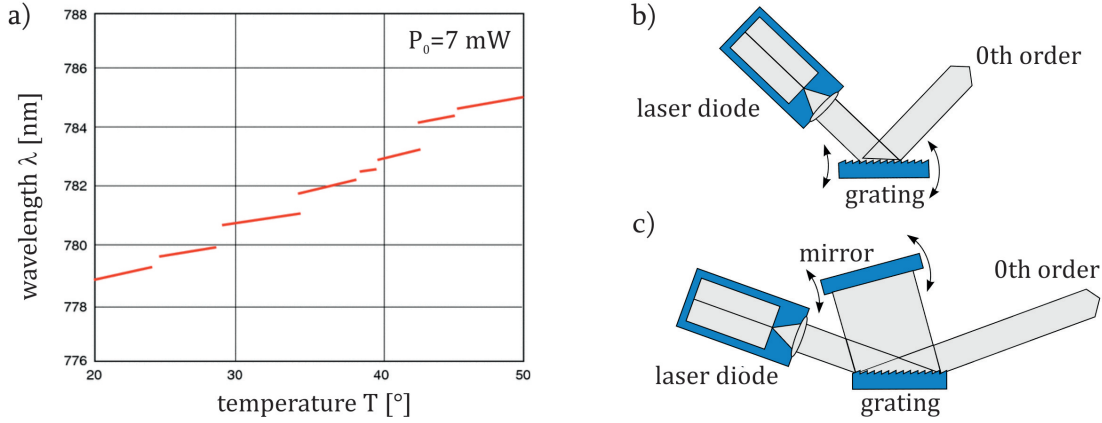
Figure 3.3.: a) Characteristic mode hopping of a laser diode occurring by varying the laser diode temperature (modified; original from [97])
b) Littrow and c) Littman-Metcalf configuration of external cavity diode lasers (both modified; original from [98])

where R_{ij} denotes the transition rates between the respective bands i and j [94]. An alteration in the band occupancies in eq. (3.6) thus leads to a modification of the emission frequency distribution. Especially troublesome is the discontinuous frequency mode hopping of semiconductor lasers occurring during a variation of the diode material's temperature [96] (see fig. 3.3b)).

These disturbances can only be handled by means of a dedicated temperature controller compensating for potential temperature drifts by actuating a Peltier element attached to the laser diode or its mount. Both the laser diode current and temperature controller need to be specifically designed and fine-tuned for the respective laser diode, its mount and their coupling to the thermal bath (normally the optical table).

3.2.2. Laser diode frequency tunability and stabilization via optical feedback

Diode lasers are usually passively and actively frequency stabilized by providing optical feedback. For that purpose the desired frequency is sent back into the laser resonator, thus enhancing the stimulated emission into that frequency mode [99]. Typically, optical feedback is provided by the application of a suitable diffraction grating in front of the laser diode aperture (an introduction to gratings will follow in sec. 4.1). Depending on the chosen configuration, one diffraction order is reflected into the laser resonator (either directly or by means of an additional mirror), while the 0th diffraction order propagates forward as the actual laser output beam. This technique is based upon the application of an external cavity to the laser diode. That is why diode lasers supported by such an additional feedback grating are called external cavity diodes laser (ECDL). Two possible grating geometries are the Littrow and the Littman-Metcalf configuration. In Littrow configuration (see fig. 3.3b)) the incidence angle on the grating is chosen such that the 1st order (less often the 2nd order) of the desired wavelength is diffracted back into the laser diode. The frequency tunability is realized by tilting the grating slightly, causing the feedback of another frequency component. This is in principle a simple method, however, the tilting always comes along with a change in the diffraction angle of the 0th order, necessitating a readjustment of all subsequent optics in the worst case.[2]

From this perspective, the Littman-Metcalf configuration (see fig. 3.3c)) provides a more convenient means of optical feedback [101]. Here, the laser diode beam comes at grazing

---

[2]One tricky option to overcome this problem is presented in [100].

incidence to the grating causing the 1st order diffracted beam to be nearly normal to the grating plane. A mirror then reflects the 1st order the same way back to the grating such that it is diffracted back into the laser resonator. The laser output is formed by the 0th order beam. The difference to Littrow configuration constitutes in that it is the tilt of the mirror, not the grating that entails the frequency selection. Therefore, in Littman-Metcalf configuration the diffraction angle of the laser output beam stays invariant under frequency variation. In satisfying this condition, high demands apply to the mounting assembly and geometric alignment of the mirror.

In order to smoothly scan over a specified wavelength range in both configuration cases, a specific turning point (also called 'pivot point') geometry has to be met [102, 103].

ECDLs serve well as frequency adjustable coherent light sources on a range of several nm up to some hundred nm in special cases [104], which makes them perfectly suitable for spectroscopic scans over Alkali hyperfine lines [105]. The big advantage, however, is that by actuating the grating/mirror tilt over an optical frequency-locked loop, both the laser linewidth [106] and the frequency stability of ECDLs is significantly improved over those of simple laser diodes.

3.2.3. Optical frequency-locked loops (OFLL)

As outlined above, diode lasers enjoy great popularity due to their accessability for frequency control over the following three paths: the diode's temperature, the diode injection current and the external cavity angle setting. Now, the issue shall be broached of how to realize the actual control loop, which measures the system variable's state, derives the error signal, and prepares an adequate actuating signal to be fed back to the laser. Optical frequency-locked loops (OFLL) can be realized in many different ways. Often it is desired to stabilize two lasers with respect to each other. This can be accomplished via stabilizing a transfer cavity to one of the lasers and subsequently locking the other laser to the transfer cavity. Common techniques for locking lasers to cavities and vice versa are the Pound-Drever-Hall method [107, 108, 109, 110] or the Hänsch-Couillaud technique [111]. The Pound-Drever-Hall method relies on a lock-in based technique. For this method, the laser beam is modulated by an EOM before it is sent into a cavity and either the transmission or absorption profile is observed. Using the lock-in technique, locking onto the symmetric transmission/absorption peaks of the resonator is enabled. The Hänsch-Couillaud technique in contrary gets along without any modulation of the laser beam, but instead requires the presence of a birefringent medium in between the cavity mirrors. In the easiest case this would be a $\lambda/4$ phase retarder. Another option for relative frequency stabilization of two lasers is generating a beat signal of the two lasers. This option assumes one of the two lasers (the master laser) to be a normal. The frequency of the other laser (the slave laser) is then corrected such, that the difference frequency of the beat signal equals the reference frequency of an electronic local oscillator of high frequency stability [112].

For an absolute frequency stabilization locking a laser to an atomic or molecular transition is most suitable. This is usually done by the generation of a sub-Doppler absorption spectroscopy signal, e.g. based on saturation spectroscopy [113], frequency modulation spectroscopy [114, 115] or polarization spectroscopy [116, 117, 118, 119].

Principle of Polarization spectroscopy

The principle of polarization spectroscopy relies — like normal saturation spectroscopy — on a strong pump and a weak probe beam counter-propagating through the atomic sample. However, the interesting feature in polarization spectroscopy is the birefringence induced in the atomic medium by the circularly polarized pump beam. This birefringence is proportional to the pump beam intensity and is gathered by the weak probe beam in the form of an angular
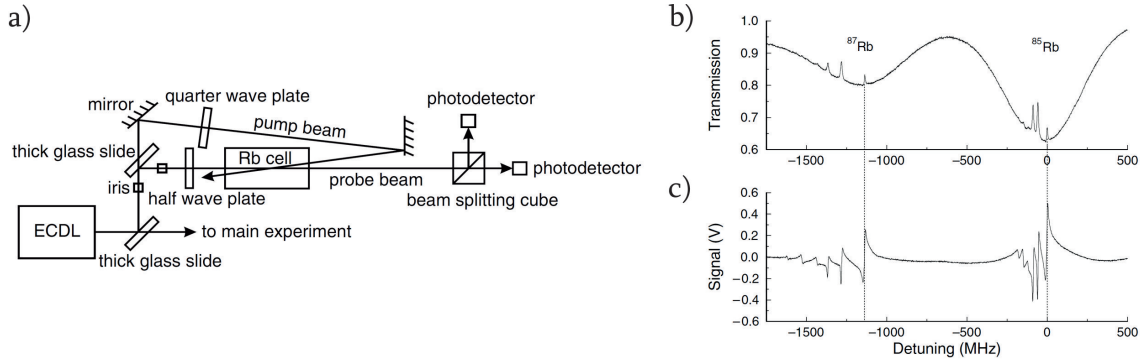
Figure 3.4.: a) Experimental setup for polarization spectroscopy using a polarizer at $45°$ instead of two crossed polarizers and the resulting curves for b) saturation and c) polarization spectroscopy of ^{87}Rb and ^{85}Rb [118].

rotation $\Delta\phi$ during propagation through the pumped medium. First experiments [116] used crossed polarizers — one in front of the atomic sample the other behind — for the subsequent detection of the penetrated probe intensity. A method yielding an approximately two times higher signal is to send the probe beam on a polarizing beam splitter (in a basis rotated by $45°$ around the optical axis) and separately detecting the transmitted and reflected probe intensities I_x and I_y, respectively. The difference signal $I_y - I_x = I_0\Delta\phi$ conveys the desired phase shift information [118]. In fig. 3.5 a compact version of this polarization spectroscopy setup is depicted (as demonstrated in [120]). Here, the probe beam is basically a recycled part of the pump beam. After propagation through the medium the pump is sent through a polarization filter at $45°$ (or a polarizing beam splitter rotated by $45°$ around the optical axis of the transmitted beam). Following the reflection at an imperfect mirror (representing a built-in attenuator) it is reflected back into the medium, but now in the role of the probe beam. The probe's polarization components are detected behind a polarization beam splitter as in [118]. The resulting difference signal is of a similar character as that obtained in the conceptually similar Hänsch-Couillaud technique [111]. It encodes the dispersion experienced by the probe near the hyperfine transitions shown in fig. 3.4c) [118]

$$I_{\text{diff}} = I_y - I_x = I_0 e^{-\alpha L - 2\alpha_w} \sin\left(\Delta\phi + \frac{\omega}{c}\Delta n_w\right) , \qquad (3.10)$$

where I_0 is the probe intensity (without cell), α the absorption coefficient of the atomic/molecular sample, L the length of the sample cell and α_w and Δn_w denote the contribution of the absorption and refractive index of the cell's windows.

This makes polarization spectroscopy a perfect way to generate the error signal needed for laser frequency locking. Specifically, locking on widths smaller than the natural laser linewidth is possible. One disadvantage of this method, however, is that the zero crossings of the difference signal from both PBS outputs I_{diff} does not necessarily coincide with the exact line position [118]. A way to circumvent this drawback is comparing the I_{diff} signal with the sum signal $I_{\text{sum}} = I_y + I_x$ which is effectively a normal saturation spectroscopy signal indicating the line positions.

3.3. Phase locking of lasers

Even a decently frequency-locked laser will suffer from a residual frequency distribution. This is mainly due to phase fluctuations on short time scales. One inherent source of phase fluctuations in a laser is the occurrence of spontaneous emission events leading to an interruption of the coherent Rabi cycle and stimulated emission process. Additional phase noise is caused by
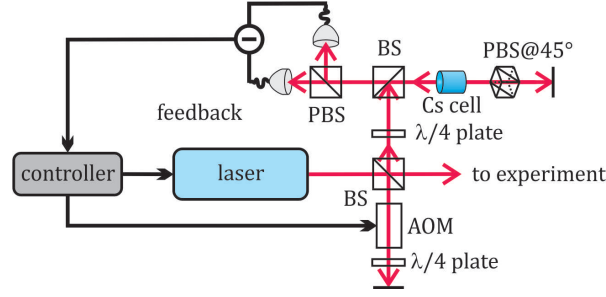
Figure 3.5.: An abstract scheme of an optical frequency-locked loop based on polarization spectroscopy including offset locking option over AOM detuning.

thermal fluctuations and variations in the injection current in a similar fashion as discussed for the sources of frequency variations in sec. 3.2.3, but on much shorter time scales. Before the more specific principle of an optical phase lock will be examined the general concept behind an electronic phase-locked loop is outlined in the following subsection.

3.3.1. Principle of phase-locked loops (PLL)

A phase-locked loop (PLL) [121, 122] basically consists of three instances:

1. A voltage controlled oscillator (VCO) which represents the oscillating unit in need of phase stabilization

2. A phase sensitive detector (PSD)

3. A loop filter.

In fig. 3.6a) an abstract scheme of a phase-locked loop (PLL) is presented. The output frequency of the voltage controlled oscillator is adjustable via an input voltage.[3] Here, the VCO is taken to generate the signal

$$v(t) = v_0 \cos(\omega_0 t + \phi_0) \ , \tag{3.11}$$

where without loss of generality $\omega_0 = const.$, and the phase $\phi_0 = \phi_0(t)$ is time dependent. Thus, the instantaneous phase of the VCO output can be written as

$$\Phi(t) = \omega_0 t + \phi_0(t) \ . \tag{3.12}$$

In order to stabilize $\Phi(t)$ the VCO signal is fed into a PSD which compares the instantaneous phase $\Phi(t)$ with a reference phase Φ_{LO} provided by a very stable local oscillator (LO). The PSD basically multiplies both inputs and thus creates the output signal

$$v_{\text{PSD}}(t) \propto \cos\left((\omega_0 - \omega_{\text{LO}})t + (\phi_0(t) - \phi_{\text{LO}})\right) + \cos\left((\omega_0 + \omega_{\text{LO}})t + (\phi_0(t) + \phi_{\text{LO}})\right) \tag{3.13}$$

which consists of oscillations at the difference and sum frequencies. By a subsequent low pass filtering of the $v_{\text{PSD}}(t)$ signal in the so called loop filter the unwanted sum frequency (called the ripple) can be removed and the error signal which is dependent on the phase difference $\Phi(t) - \Phi_{\text{LO}}$ can be obtained. The loop filter finally turns the error signal into the actuating signal to be fed back to the VCO correcting for its phase deviations from the set phase defined by the LO.

---

[3]Later, the VCO will be represented by a laser and the PLL will not work voltage based only, but take the "detour" over the optical path starting with the VCO's lasing process and ending in photodetection.

Figure 3.6.: An abstract scheme of a) a general phase-locked loop and b) an optical phase-locked loop between a master laser and a slave laser with frequency down mixing preceding the phase sensitive detection.

3.3.2. Basic principle of an optical phase-locked loop (OPLL)

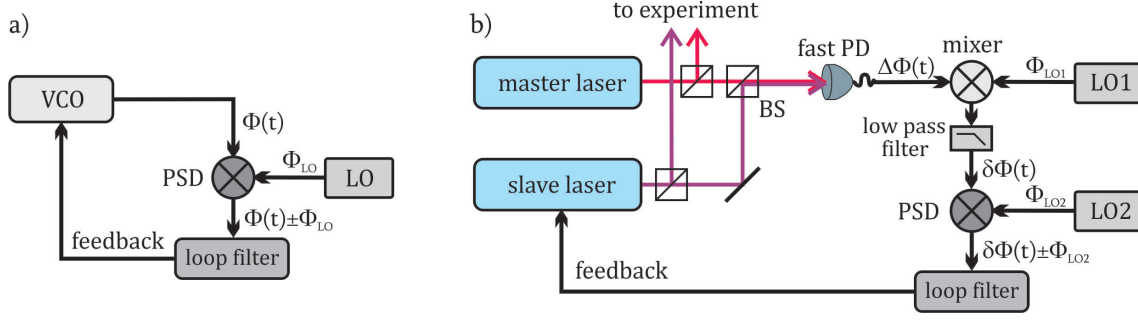In order to perform a coherent manipulation of atoms a phase stable performance of the applied laser fields is necessary. In EIT experiments for example this necessary condition applies both to the strong control field and the weak probe field. Thus, an *optical* phase locked-loop (OPLL) has to be implemented, such that the one laser, which is chosen to be the slave laser is phase stabilized to the so called master laser. After the first demonstration of an OPLL performed in 1965 [123] the technique has become a standard tool for coherent preparation of atomic and molecular systems.

An optical phase locked-loop can be seen as an extended or refined version of an OFLL presented above. Beyond frequency stabilization the OPLL determines the phase difference between both lasers and electronically process this error value in order to provide an actuating variable. The latter is fed back to the slave laser correcting for its phase deviation from the set value which is defined by the master laser phase.

The complex electric field of the master and slave is written as

$$E_m(t) = |A_m|e^{i\phi_m} \ e^{i\omega_m t} \qquad \text{and} \qquad E_s(t) = |A_s|e^{i\phi_s} \ e^{i\omega_s t} \ , \qquad (3.14)$$

where the phase $\phi_s(t)$ is taken to be time dependent. The frequency ω_m and phase $\phi_m(t)$ of the master laser field needs to be reasonably constant. Note, that generally for the frequencies $\omega_m \neq \omega_s$ holds.

Applying the PLL principle of sec. 3.3.1 to the phase locking of one laser to another raises two possible problems: First, the optical field oscillations have to be converted into electrical signals, but optical signals in the visible or infrared cannot directly be detected phase sensitively — not even by very fast photodetectors. Ultra-fast photodetectors can resolve the oscillation of electromagnetic waves only up to the GHz regime. Beyond the GHz scale only a determination of the average photon flux through the detector would be measurable.[4]

Second, the requirement for relative phase stability between to oscillators of different frequencies might seem peculiar. A phase sensitive detector cannot compare the independently oscillating phases of two signals at different frequencies directly and generate a useful error signal for phase stable frequency offset locking.

Remarkably, a simultaneous solution to both of these problems can be found by making use of heterodyne detection, i.e. a detection technique where instead of separately detecting the master and slave laser beams the superposition signal of both is measured (in sec. 4.2 a more thorough introduction to heterodyne detection is given). In order to detect the signal in a heterodyne fashion a precise alignment of both fields in a spatially mode-matched

---

[4]Typically, the rise and fall time of excitations on an ultra-fast photodetector are at least limited to the picosecond scale.

superposition is required (e.g. by superimposing them on a 50/50 beam splitter or an optical fiber directional coupler). The intensity incident on the photodetector then follows as

$$
\begin{aligned}
I &\propto |E_m(t) + E_s(t)|^2 & (3.15)\\
&= |A_m|^2 + |A_s|^2 + |A_m||A_s|\left(e^{i(\omega_m-\omega_s)t+i(\phi_m-\phi_s)} + e^{-i(\omega_m-\omega_s)t-i(\phi_m-\phi_s)}\right) & (3.16)\\
&= |A_m|^2 + |A_s|^2 + 2|A_m||A_s|\cos\Delta\Phi(t) \ , & (3.17)
\end{aligned}
$$

where the oscillatory term is driven by the instantaneous phase difference

$$
\Delta\Phi(t) = \Phi_m(t) - \Phi_s(t) = \Delta\omega t + \Delta\phi(t) \tag{3.18}
$$

which oscillates at the difference frequency $\Delta\omega = \omega_m - \omega_s$ and carries the time dependance on the slave phase $\Delta\phi(t) = \phi_m - \phi_s(t)$. The time derivative of the instantaneous phase difference defines the instantaneous frequency difference $\Delta\Omega = \mathrm{d}(\Delta\Phi)/\mathrm{d}t$. A coherent performance of master and slave laser can be achieved provided $\mathrm{d}(\Delta\phi)/\mathrm{d}t = 0$ so that the instantaneous frequency difference satisfies [124]:

$$
\Delta\Omega = \frac{\mathrm{d}}{\mathrm{d}t}\left(\Delta\omega t + \Delta\phi(t)\right) = \Delta\omega = const. \ . \tag{3.19}
$$

Thus, the time dependance of the slave's instantaneous phase $\Phi_s(t)$ can be continuously readjusted by the OPLL by driving the difference frequency $\Delta\omega(t)$ to the desired set difference frequency $\Delta\omega^{\mathrm{set}}$ supplied by a local oscillator.

Phase sensitive detectors are mainly available from the MHz to GHz domain. In many experimental configurations, however, the set difference frequency $\Delta\omega^{\mathrm{set}}$ between master and slave laser is orders of magnitudes too high for being phase sensitively detected right away (e.g. if $\Delta\omega^{\mathrm{set}}$ is above the GHz range). In this case the difference frequency signal $\Delta\Phi(t)$ needs to be down-converted — as shown in fig. 3.6b) — via a mixing with a local oscillator LO1 at a frequency $\omega_{\mathrm{LO1}} = \Delta\omega^{\mathrm{set}} - \omega_{\mathrm{LO2}}$ which is slightly detuned from the set difference frequency $\Delta\omega^{\mathrm{set}}$ e.g. by a ω_{LO2} at around 100 MHz. That way the signal behind the mixer and after passing a low-pass filtered reads

$$
v(t) \propto \cos\left((\Delta\omega - \omega_{LO1})t + (\Delta\phi - \phi_{LO1})\right) \ , \tag{3.20}
$$

such that only the difference frequency

$$
\delta\omega = \Delta\omega - (\Delta\omega^{\mathrm{set}} - \omega_{\mathrm{LO2}}) \ , \tag{3.21}
$$

or more precisely, the signal phase

$$
\delta\Phi(t) = \Delta\Phi(t) - (\Delta\Phi^{\mathrm{set}} + \Phi_{\mathrm{LO2}}) \tag{3.22}
$$

goes into the phase sensitive detector. The PSD compares the phase of $\delta\Phi(t)$ with a second, extremely stable local oscillator LO2 of instantaneous phase Φ_{LO2} at ω_{LO2} and generates an error signal

$$
\begin{aligned}
v_{\mathrm{PSD}}(t) &\propto \cos\left((\Delta\omega - \omega_{\mathrm{LO1}} + \omega_{\mathrm{LO2}})t + (\Delta\phi - \phi_{\mathrm{LO1}} + \phi_{\mathrm{LO2}})\right) & (3.23)\\
&+ \cos\left((\Delta\omega - \omega_{\mathrm{LO1}} - \omega_{\mathrm{LO2}})t + (\Delta\phi - \phi_{\mathrm{LO1}} - \phi_{\mathrm{LO2}})\right) \ . & (3.24)
\end{aligned}
$$

As for the standard PLL the error signal is now fed into the loop filter which prepares the actuating value to be fed back to the actuating element of the diode laser rendering the necessary phase correction. In fact, there can be different final control elements, each being suited for specific time-scale regimes. Thus, the loop filter would in such a case split the actuating value depending on the time scale of the occurring phase fluctuation and distribute the correcting value among the available actuating elements in a suitable fashion, respectively.

3.4. Characterization of the phase noise of an OPLL

Determining the performance of a phase-locked loop is most suitably done by determining the short term stability of the system, i.e. the phase noise of the oscillator. For that purpose different conceptual as well as experimentally convenient measures for the phase noise performance of a phase lock are presented in the following.

3.4.1. Phase noise measures

Ideally the beat signal between master and slave laser will result in a pure sinusoidal wave with oscillation frequency $\Delta\omega^{\mathrm{set}}$. In the frequency representation this corresponds to a delta function shaped peak. Residual phase noise $\phi(t)$, however, leads to random phase shifts on the detected beat signal observed with a spectrum analyzer as voltage

$$v(t) \propto \cos(\Delta\omega^{\mathrm{set}}t + \phi(t)) \ . \tag{3.25}$$

Thereby, the power spectral density of the beat signal obtains a finite width. The phase noise distribution is fundamentally defined over the power spectral density of the phase fluctuations within a bandwidth B of 1 Hz at a frequency offset f from the carrier frequency at $\Delta\nu^{\mathrm{set}}$

$$S_\phi^{\mathrm{DSB}}(f) = \frac{1}{B}\int_{f-B/2}^{f+B/2} |\phi(f')|^2 \mathrm{d}f' \ . \tag{3.26}$$

This is the double sideband (DSB) power spectral density given in units of $\mathrm{rad}^2/\mathrm{Hz}$. The power spectral density is in direct correspondence with the auto-correlation function of the phase fluctuations

$$C(\tau) = \overline{\phi(t)\phi(t+\tau)} \tag{3.27}$$

where the overbar denotes time-averaging [125]. In particular, the Wiener-Khintchine theorem [126, 127] states that the Fourier transform of the auto-correlation function be equivalent to the power spectral density, i.e.

$$S_\phi^{\mathrm{DSB}}(f) = \int_{-\infty}^{\infty} C(\tau)e^{i2\pi f\tau}\mathrm{d}\tau \ . \tag{3.28}$$

For practical purposes the power spectral density is more conveniently represented in terms of the frequency noise [128]

$$S_\omega^{\mathrm{DSB}}(f) = f^2 S_\phi^{\mathrm{DSB}}(f) \ . \tag{3.29}$$

While the double sideband power spectral density is defined for both positive and negative frequencies f from a physical point of view the definition of a single sideband power spectrum appears more convenient:

$$S_\phi^{\mathrm{SSB}}(f) = 2S_\phi^{\mathrm{DSB}}(f) = 2|\phi(f)|^2 \ , \qquad f > 0 \ . \tag{3.30}$$

For a better visualization of small noise peaks the power spectral density is often given on a logarithmic scale and in a form normalized to its peak value S_{carrier} [129, 130]

$$\mathcal{L}^{\mathrm{SSB}}(f) = 10\log\left(\frac{S^{\mathrm{SSB}}}{S_{\mathrm{carrier}}}\right) \ . \tag{3.31}$$

It is given in units of decibels below the carrier per Hz bandwidth (dBc/Hz).
The phase noise variance σ_ϕ^2 corresponding to a Gaussian shaped phase noise distribution can easily be extracted from experimental data over the power fraction in the carrier compared to the total power of the phase noise distribution [131, 132]

$$\eta = \frac{S_{\mathrm{carrier}}}{\int_0^\infty S^{\mathrm{SSB}}(f)\mathrm{d}f} \simeq e^{-\sigma_\phi^2} \ . \tag{3.32}$$

4. Narrow-band Filtering Suitable for Few Photon Detection

Building fast and reliable single-photon counting detectors of high efficiency is extremely challenging on its own. However, in many practical applications it is furthermore necessary to reduce background radiation to a reasonable level. If a narrow-band few photon signal is "hidden" in a broad-band noise background very fine-selective frequency filtering can help improve the signal-to-noise ratio significantly. Conventional few photon detectors do not provide intrinsic narrow-band detection, but possess rather wide detection bandwidths in the order of several hundred nm. Thus, additional effort is required, i.e. the realization of a narrow-band frequency filter specifically designed for the desired few photon wavelength.

In this chapter possible experimental techniques for such a narrow-band detection of optical signals at low intensities down to the single photon level within broad-band backgrounds are outlined. Two filtering methods are compared: the first one by means of spatially selecting the signal diffracted by a grating, the second performed by heterodyne detection of the signal. First, the theoretical principles underlying both diffraction gratings and heterodyne detection are introduced. Subsequently, advantages and disadvantages as well as experimental requirements and possible difficulties of both techniques are discussed.

4.1. Diffraction grating filter

In this section we examine the basic principles of diffraction gratings. Important parameters and quantities are introduced, which are useful for the characterization of the performance of a diffraction grating for filter applications. Finally, several criteria are shown for choosing the most suitable grating for a desired filter application.

4.1.1. Basic Principle

Diffraction gratings act as devices impressing a periodical phase modulation on an incident light beam. The grating equation

$$d(\sin\alpha + \sin\beta_m) = m\lambda \, , \qquad m \in \mathbb{Z} \tag{4.1}$$

gives the condition for the formation of the mth diffraction order into a diffraction angle β_m of a light wave of wavelength λ, incident with an angle α on a grating with grating period d (see fig. 4.1a)) [133, 134]. The grating period d is the spatial period of the blazed grating structure, i.e. the groove-to-groove distance. Grating manufacturers conventionally specify the grating period in terms of the groove density $G = 1/d$ in units of the number of grooves per mm, i.e. 1/mm. Diffraction into an angle β_m will occur for all settings where the optical path difference Δs (see fig. 4.1b)) between two rays incident on the grating with a distance of the grating parameter d equals an multiple integer of the wavelength, i.e.

$$\Delta s = d(\sin\alpha + \sin\beta_m) = m\lambda \, . \tag{4.2}$$

Here, the sign convention for the angles is the following: positive on the side of the incident beam, negative on the other side of the grating normal. Note furthermore, that the sign of the
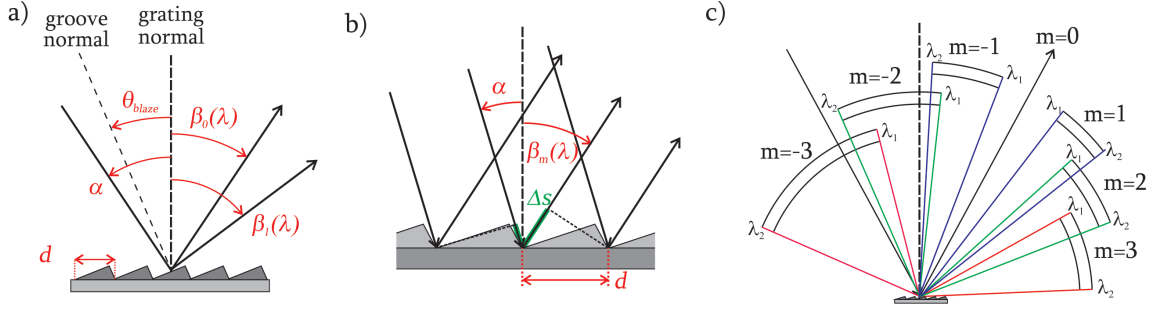
Figure 4.1.: a) Scheme of a diffraction grating with its characterizing parameters $d = 1/G$ and θ_{blaze} and two diffraction orders $m = 0$ and $m = 1$ for a monochromatic beam of light.
b) Illustration of the optical path difference Δs occurring for two beams incident on the grating with a distance of the groove-to-groove distance d.
c) Illustration of the formation of the first three diffraction orders and the occurring overlap for a beam with a spectral width from λ_1 to λ_2 ($\lambda_1 < \lambda_2$).

diffraction orders m is a matter of convention too, and is tied to the angular sign convention. In fig. 4.1c) the version is displayed resulting from the sign convention mentioned above. The signs of the diffraction orders are given with respect to the angular position of the 0th order diffracted beam:

$$m \begin{cases} > 0 & \text{if } \beta_m < \beta_0 \\ < 0 & \text{if } \beta_m > \beta_0 \end{cases} . \tag{4.3}$$

The respective angles of diffraction β_m for a given geometric configuration follow according to eq. (4.1) as

$$\beta_m = \arcsin\left(\frac{m\lambda}{d} - \sin\alpha\right) . \tag{4.4}$$

A special geometric configuration often used for gratings employed as an external cavity for diode lasers is known as Littrow configuration (see fig. 3.3b) in sec. 3.2.2), where the incident and diffracted beam of a specific order coincide: $\beta(\lambda)_m^{\text{Litt}} = \alpha(\lambda)_m^{\text{Litt}}$. In that case the grating equation becomes

$$2\sin\beta_m^{\text{Litt}}(\lambda) = \frac{m\lambda}{d} , \tag{4.5}$$

and the Littrow angle for the mth order is given by

$$\beta_m^{\text{Litt}}(\lambda) = \arcsin\left(\frac{m\lambda}{2d}\right) . \tag{4.6}$$

Accordingly, performance in Littrow configuration (at a given wavelength and order) requires a grating period d specifically designed for that purpose. Furthermore, to be examined in detail in sec. 4.1.5, the blaze angle θ_{blaze} of the grating has to be adapted to this specific geometric situation as well (see fig. 4.1a)).

4.1.2. Fundamental and experimental constraints for grating parameters

Both fundamental as well as experimental restrictions apply to the domain of physical and reasonable grating parameters, respectively. In the following these working values shall be explained.

Fundamental restrictions:

At first, the only physical lower bound for the grating period is, that no d for which
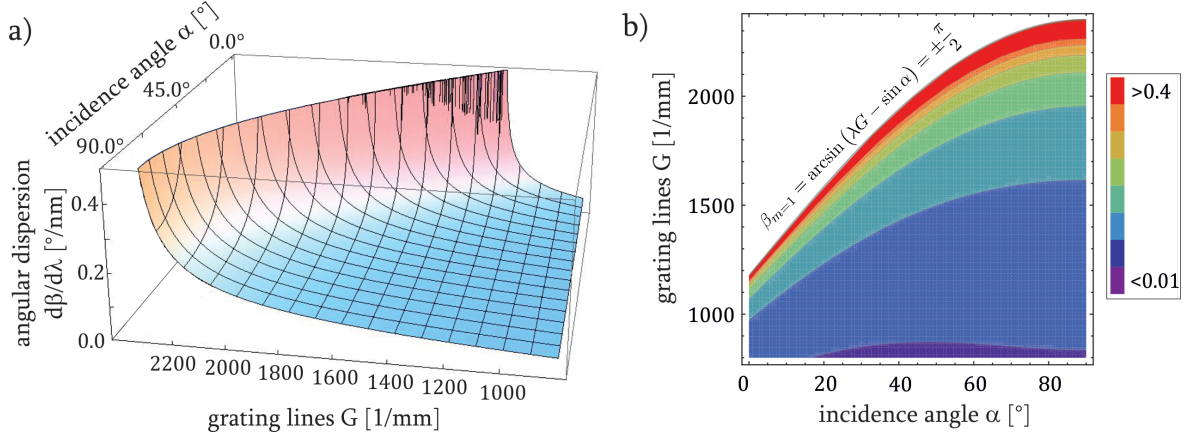
$$\frac{\lambda}{2} > d \tag{4.7}$$

Figure 4.2.: Displayed is the angular dispersion experienced by a first order diffracted ray at a wavelength of 852.347 nm (the Cs D2 transition) plotted in dependance on the number of grating lines per nm G and the incidence angle α: a) shows the range and gradient of the angular dispersion while the contour plot in b) illustrates the domain of incidence angles and grating periods.

applies, can diffract a wavelength λ; a wave simply "can't see" a grating with a grating period smaller than half its wavelength. Apart from this fundamental constraint, in principle, diffraction gratings with any grating period d can be used at any incident angle α. However the argument of the arcsine in eq. (4.4) will only reveal real (i.e. physical) diffraction angles, if

$$-1 < \frac{m\lambda}{d} - \sin\alpha < 1 \ . \tag{4.8}$$

This constraint in return puts restrictions on the choice of suitable incident angles α for each given grating period d.

Further restrictions apply for the domain of m, so that the formation of higher orders (see fig. 4.1c)) can be suppressed either partly or fully. Going back to the grating eq. (4.1) one concludes, that $|m\lambda/d| < 2$ needs to be satisfied, as $|\sin\alpha + \sin\beta| > 2$ is not possible. Thus, there exists a minimal d for each wavelength for the formation of diffraction up to a desired order m. This of course leads to the convenient side effect that — the other way round — by choosing suitable ratio of λ and d the formation and therefore the angular overlapping of different diffraction orders (see fig. 4.1c)) can be suppressed.

A measure of the spectral resolution can be found in terms of the angular dispersion, which describes how the differential angular splitting of different wavelengths scale. It is derived by differentiating the diffraction angle in eq. (4.4) with respect to the wavelength:

$$\frac{\mathrm{d}\beta_m}{\mathrm{d}\lambda} = \frac{m}{d\cos\beta_m} = \frac{\sin\alpha + \sin\beta_m}{\lambda\cos\beta_m} \ . \tag{4.9}$$

Generally, the angular dispersion $\mathrm{d}\beta_m/\mathrm{d}\lambda$ of a grating increases with decreasing grating period d for a fixed incident angle α and order m.

The plots in fig. 4.2 reveals that the angular dispersion increases with the groove density and with the inverse incidence angle up to some value where the dispersion hits a singularity. Beyond these particular values no diffraction orders can be formed. The boundary values are determined at those points where the cosine in eq. (4.9) becomes zero. This is the case when

$$\beta_m = \arcsin\left(m\lambda G - \sin\alpha\right) = \pm\frac{\pi}{2} \ . \tag{4.10}$$

Subsequently, for a fixed grating density G the minimum incidence angle follows as

$$\alpha_{\min}\Big|_{\text{fixed } G} = \arcsin\left(m\lambda G \pm 1\right) \tag{4.11}$$

and for a fixed incidence angle α the maximum groove density is

$$G_{\max}\Big|_{\text{fixed }\alpha} = \frac{\sin\alpha \pm 1}{m\lambda} \ . \tag{4.12}$$

Here again, the upper limit for G for a fixed operation wavelength λ can be derived as

$$\max\left\{G_{\max}\Big|_{\text{fixed }\lambda}\right\} = \frac{2}{\lambda} \tag{4.13}$$

in a more rigorous fashion than already suggested in the argumentation around eq. (4.7). Fig. 4.2a) and especially the upper right edge in fig. 4.2b) demonstrate this to be a hard criterion.

Experimental restrictions:

The grating equation furthermore specifies possible combinations of grating periods and corresponding angles α and β, which lead to desirably high values of angular dispersion. For the sake of clarity in fig. 4.2 the angular resolution from eq. (4.9) has been plotted in dependance on incidence angle and grating period. In order to reach high angular dispersion one wants to find experimental settings which lead to values sitting as high as possible on the steep slope. In that respect it becomes clear that for practical purposes one will have to preselect gratings with a suitable grating period and adjust the working incident angle accordingly in order to get maximal angular resolution. But even if for one experimental configuration the maximum resolving power was sufficient (for a desired application) and furthermore a grating could be found, which satisfied the conditions for the grating period and incidence angle leading to high angular dispersion (formulated above), the resulting diffraction angle β could arise to be experimentally inconvenient or even imaginary, i.e. the diffracted order does not exist (see fig. 4.2). Specifically, possible difficulties could emerge due to very steep or very flat incidence and diffraction angles necessary in order to achieve high angular dispersion. Quite generally, incident and diffraction angles below $(\alpha, |\beta|) < 5°$ or above $(\alpha, |\beta|) > 85°$ will experimentally be out of question, due to trivial geometric difficulties and a dramatic breakdown of virtually every grating's diffraction efficiency [135].

4.1.3. Measures for the filter characteristic of diffraction gratings

In this account a diffraction grating can be seen as a frequency fine-selective imaging tool. As for all imaging devices it is important to adapt and optimize certain physical quantities for the desired configuration. For narrow-band filtering applications the ratio between the absolute angular splitting of different wavelengths and the actual angular width of a monochromatic wavelength component is the figure of merit. Moreover, the criterion for the minimal angular splitting of two neighboring diffraction peaks has to be considered.
The angular dispersion $\mathrm{d}\beta_m/\mathrm{d}\lambda$ introduced in eq. (4.9) gives the angular spread between two rays of different wavelength. Generally, the angular dispersion of a grating increases with decreasing grating period d for a fixed incident angle α and order m. But in order to determine the actual resolving power of a grating the width of each monochromatic spectral component has to be taken into account as well. For this purpose the intensity distribution $I(\beta_m)$ diffracted into a certain angle $\beta_m(\lambda)$ has to be considered. It follows as [136]

$$I(\beta_m) = I_0 \left(\frac{\sin(N\Delta\phi/2)}{\sin(\Delta\phi/2)}\right)^2 \tag{4.14}$$

where the phase difference $\Delta\phi$ is given by

$$\Delta\phi = \frac{2\pi}{\lambda}\ \Delta s = \frac{2\pi}{\lambda}\ d(\sin\alpha + \sin\beta_m) \tag{4.15}$$
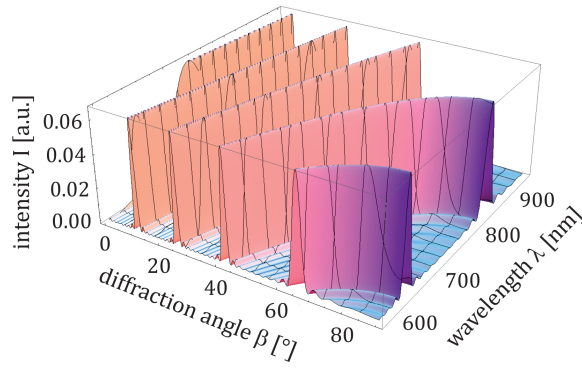
Figure 4.3.: Plot of the intensity distribution $I(\beta_m, \lambda)$ showing the formation of several diffraction orders in both the wavelength and the diffraction angle dependance.

and the corresponding optical path difference Δs defined by the condition for constructive interference in eq. (4.2). A plot of the intensity distribution $I(\beta_m)$ is shown in fig. 4.4a). The angular pulse width $\delta\beta_{\mathrm{pw}}$ of a spectral line is defined as the angular splitting between the nearest zeros on either side of the spectral peak whose center position is given by $\beta_m(\lambda)$ (see fig. 4.4b)). The angular pulse width is determined by the diffraction process at multiple grooves and is given by [134, 136]

$$\delta\beta_{\mathrm{pw}} = \frac{2\lambda}{Nd\cos\beta_m} \ , \tag{4.16}$$

while the angular linewidth (i.e. the FWHM) can be approximated by half the pulse width[1]

$$\delta\beta \simeq \frac{\lambda}{Nd\cos\beta_m} \tag{4.17}$$

(see fig. 4.4b)). Note, that the linewidth scales inversely proportional to the illuminated grating width $w = Nd$.

The resolving power $\mathcal{R}$ of a grating is defined as the ratio between wavelength λ and minimal resolvable wavelength difference $\Delta\lambda_{\mathrm{min}}$ as [134]

$$\mathcal{R} = \frac{\lambda}{\Delta\lambda_{\mathrm{min}}} \ . \tag{4.18}$$

The value for $\Delta\lambda_{\mathrm{min}}$ is defined at the limit of resolution. Neglecting distortions by beam forming optics this limit arises under the terms of the Rayleigh criterion when the maximum of one spectral line coincides with the first minimum of the neighboring one (see fig. 4.4b)). Subsequently, the limit is reached, if the angular separation is half the angular pulse width $\delta\beta_{\mathrm{pw}}$ of the spectral component. Thus, the minimal angular spread of two resolvable diffracted wavelengths follows as

$$(\Delta\beta)_{\mathrm{Rayleigh}} = \frac{1}{2}\delta\beta_{\mathrm{pw}} = \frac{\lambda}{Nd\cos\beta_m} \ . \tag{4.19}$$

Together with eq. (4.9) this corresponds to the minimally resolvable wavelength difference

$$(\Delta\lambda)_{\mathrm{Rayleigh}} = \left(\frac{\mathrm{d}\beta}{\mathrm{d}\lambda}\right)^{-1}(\Delta\beta)_{\mathrm{Rayleigh}} = \frac{\lambda}{mN} \tag{4.20}$$

---

[1]This is a reasonably good approximation in that the diffraction peak curves depicted in fig. 4.4b) and the pulse width in eq. (4.16) represent the ideal case. For real reflection gratings, however, (especially for holographic gratings with a sinusoidal groove profile) these linewidths are subject to distortions both in height and shape.
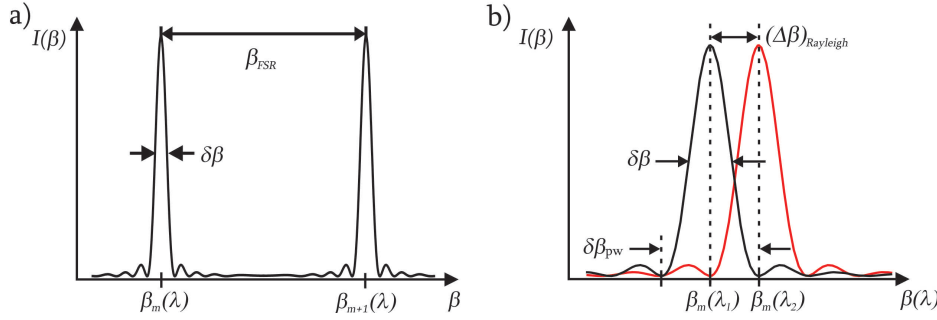
Figure 4.4.: a) Intensity distribution of a monochromatic beam diffracted at a grating with 20 grooves and b) visualization of the Rayleigh criterion at the limit of resolution for two neighboring wavelengths λ_1 and λ_2 with the angular pulse width $\delta\beta_{\text{pw}}$ and angular linewidth $\delta\beta$, respectively.

which gives the resolving power

$$\mathcal{R} = \frac{\lambda}{\Delta\lambda_{\min}} = \frac{\lambda}{(\Delta\lambda)_{\text{Rayleigh}}} = \frac{Nd(\sin\alpha + \sin\beta_m)}{\lambda} = mN \ . \tag{4.21}$$

It is an important result that the resolving power of each diffraction order is determined by the number of illuminated grooves of the grating.

In the special case of Littrow configuration the resolving power takes the form

$$\mathcal{R}_{\text{Litt}} = \frac{2Nd\sin\beta_m^{\text{Litt}}}{\lambda} = mN \ , \tag{4.22}$$

which is equivalent to the result in eq. (4.21) only at first sight. Mind, that more specific restrictions apply to the set of possible values for the angles α and order m compared to the general case of eq. (4.21).

The theoretical maximum resolving power is reached under the extremal condition of $\sin\alpha + \sin\beta_m = 2$ (corresponding to the maximal mathematically feasible angles of $\alpha = \beta = \pi/2$), i.e.

$$\mathcal{R}_{\max} = \max\left(\frac{\lambda}{(\Delta\lambda)_{\text{Rayleigh}}}\right) = \frac{2Nd}{\lambda} = \frac{2w}{\lambda} \ . \tag{4.23}$$

For a homogenously illuminated grating the grating width w can be identified with the light beam diameter or to a first approximation with the Gaussian beam waist. The grating width illuminated by the beam therefore gives rise to an upper bound for the resolution of the grating–beam configuration, which is independent of the specific parameters of the grating and angle setup.

In the following sections it will become clear, that this maximum resolving power is to be seen solely as a theoretical upper bound and not as an actual optimum value. Generally speaking it is not even in the ideal case possible to reach the maximum resolving power. The underlying angular requirement corresponds to the ideal special case of Littrow configuration eq. (4.6), but at grazing incidence $\alpha(\lambda)_{\text{Litt}} = 90°$. In that case special restrictions apply for the grating period, namely

$$d = \frac{m\lambda}{2} \ . \tag{4.24}$$

For the first diffraction order one would therefore need a groove-to-groove distance in the order of half the wavelength, apart from the fundamental geometrical problems arising from the preconditioned grazing incidence. For all practical purposes, satisfying both of these conditions simultaneously is impossible. Even a near maximum power performance is unrealistic for appropriate gratings as the necessary groove density and blaze angle literally do not exist.
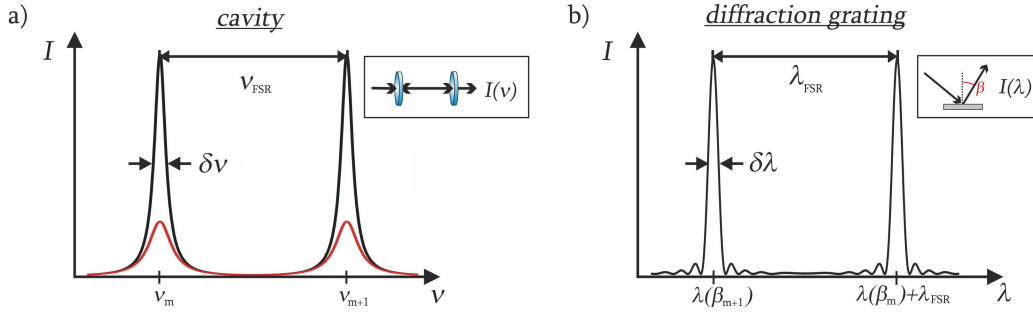
Figure 4.5.: Analogy between a) the cavity and b) the diffraction grating transfer functions.

4.1.4. Transmission properties of diffraction gratings — an analogy to cavities

Despite the very different physics underlying the frequency selectivity occurring at cavities and diffraction gratings there is some remarkable correspondence concerning their transmission function characteristics. The intensity profile of monochromatic diffraction lines drawn in fig. 4.4a) in the angular representation is reminiscent of the transmission function of a cavity described by the Airy formulas for transmission and reflection (see e.g. [133, 134, 136]). Cavities are devices frequently used for filtering applications. They basically consist of two mirrors (preferably of high field reflectivity r) in a Fabry-Pérot configuration. The finesse of a cavity

$$\mathcal{F} = \frac{\lambda_{\text{FSR}}}{\delta\lambda} \tag{4.25}$$

is a measure of its filter quality and is given by the ratio between free spectral range λ_{FSR} and linewidth $\delta\lambda$ of the transmitted field. The free spectral range of a cavity is determined by its geometrical configuration, namely the distance of the cavity mirrors l and the refraction index of the medium between them:

$$\nu_{\text{FSR}} = \frac{c}{2nl} \tag{4.26}$$

The linewidth $\delta\lambda$ in contrary is set by the finesse of the cavity

$$\mathcal{F} = \frac{\pi r}{1 - r^2} \quad, \tag{4.27}$$

whose only determining parameter is the mirror reflectivity r causing a linewidth of

$$\delta\nu = \frac{c}{2nl\mathcal{F}} \quad. \tag{4.28}$$

The finesse is connected to the resolving power of the cavity

$$\mathcal{R} = \frac{\lambda}{\Delta\lambda_{\text{min}}} \tag{4.29}$$

via the relation

$$\mathcal{R} = m\mathcal{F} \quad. \tag{4.30}$$

In some sense a comparable signature can be determined for a diffraction grating. The intensity distribution in fig. 4.4a) showing two diffraction orders as a function of the diffraction angle translates into a wavelength dependance as shown in fig. 4.3. This wavelength dependence of the intensity distribution is replotted in fig. 4.5b) where it is directly compared to the Airy transmission function of a cavity in fig. 4.4a). Analogously, the free spectral range

of a grating is defined in the setting, where the diffraction angle of order $m + 1$ at wavelength λ coincides with the diffracted beam of order m at $\lambda + \lambda_{\text{FSR}}$, i.e.

$$d(\sin\beta + \sin\alpha) = (m+1)\lambda = m(\lambda + \lambda_{\text{FSR}}) \ . \tag{4.31}$$

The free spectral range follows as

$$\lambda_{\text{FSR}} = \frac{\lambda}{m} \ . \tag{4.32}$$

The spectral linewidth $\delta\lambda$ is approximately given by half the angular pulse width in eq. (4.16) multiplied by the angular dispersion of eq. (4.9):

$$\delta\lambda \simeq \left(\frac{\mathrm{d}\beta_m}{\mathrm{d}\lambda}\right)^{-1} \delta\beta_{\text{pw}}/2 = \frac{\lambda}{mN} \ . \tag{4.33}$$

Thus, for the grating the number of illuminated grooves turns out to be the factor determining the spectral linewidth compared to the cavity case where the mirror quality is crucial. In analogy to the cavity case we can now derive the finesse of the grating to be

$$\mathcal{F} = N \ . \tag{4.34}$$

This shows that also in the case of a diffraction grating the relation eq. (4.30) between resolving power and finesse holds in good approximation.

4.1.5. Diffraction grating efficiency characteristics

When analyzed more closely one may observe that the intensity distributions $I(\beta, \lambda)$ depicted in fig. 4.3 and fig. 4.4 are subject to modulations. This is mainly due to two effects. One is the contribution of the blazing angle determining the angular characteristics of the grating efficiency. The other is related to the specific grating type and its coating.

Grating types and coatings:

A grating's diffraction efficiency characteristics are bound to the manufacturing process determining its groove profile [135]. Holographic gratings inherently tend to sinusoidal groove profiles, while mechanically ruled gratings have more triangular shaped grooves. This gives rise to a dramatic difference in their diffraction efficiency as a function of the wavelength and diffraction angle. Moreover, efficiency varies for plane reflection gratings, transmission gratings, Echelle gratings and concave gratings as well [135, 137]. It shall be noted that usual transmission gratings with higher grating densities $G > 600/\text{mm}$ suffer strongly in terms of their diffraction efficiencies. That is why they are not suitable for applications necessitating high angular dispersion. Similarly, high grating densities are hardly fabricable on the curved surfaces of concave gratings leading only to restricted angular dispersion values. Echelle gratings again are literally defined as gratings with low periodicity.
Concerning the surface quality holographically fabricated gratings suffer much less from irregularities and eventual surface lesions than mechanically ruled ones. Especially the periodicity of holographic gratings is superior to mechanical gratings, where one groove is formed after the other while the former interferometric gratings have all grooves formed simultaneously.
Another factor principally limiting the grating efficiency is its surface coating. Generally speaking for the optical domain gold coatings are favorable in terms of their high efficiency over standard aluminum coatings [137].

Blazing angle:

When using a diffraction grating it is of crucial importance that it is implemented with respect to its blaze angle

$$\theta_{\text{blaze}} = \frac{\alpha + \beta}{2} \ , \tag{4.35}$$

i.e. the angle under which the grooves are ruled (groove facet angles). This angle is identical to the incidence angle for which optimal diffraction efficiency into the first diffraction order is to be expected. For average commercial gratings, even diffraction angles β deviating from the blaze angle by $5° - 10°$ lead to a fatal breakdown in diffraction efficiency. Likewise big angle differences $|\alpha - \beta_m| > 15°$ are not to be favorized for usual gratings as the respective diffracted order will suffer from strong efficiency suppression.
Certainly, the optimal blaze angle varies for different incident wavelengths. Therefore, grating manufacturers always indicate the blaze wavelength

$$\lambda_{\text{blaze}} = \frac{2}{Nm} \sin \theta_{\text{blaze}} \ \cos(\alpha - \theta_{\text{blaze}}) \tag{4.36}$$

corresponding to a certain blaze angle, respectively. Unless otherwise specified the blaze angle and wavelengths indicated in grating catalogues will refer to the corresponding values in the Littrow configuration.
After all, the choice for a specific diffraction grating will be due to the available blaze angle of the grating grooves either supporting the theoretically determined optimal incidence angle and wavelength or not. The vast majority of diffraction gratings is designed for Littrow configuration and thus they are blazed for the respective Littrow angle of a specific wavelength: $\theta_{\text{blaze}} = \alpha_{\text{Litt}}$. Therefore, special effort is to be taken for finding a suitable grating supporting all needs toward high angular dispersion for narrow-band filtering.

4.2. Narrow-band filtering based on heterodyne/homodyne detection

The concept of heterodyne detection provides different interesting aspects, which can fruitfully be adopted for advanced optical filter applications. First, heterodyne mixing of a signal field with an optical local oscillator field leads to an effective conversion of the signal frequency. This allows for a fine-selective spectral detection at visible and infrared frequencies, which would otherwise be completely unresolvable by direct detection techniques using conventional photodetectors. Due to the heterodyne frequency down-conversion the resulting oscillations of the photodiode currents can be conveniently frequency analyzed by means of standard electronic filtering. Second, in the case of few to single photon signals heterodyne detection can be applied as a technique for single photon correlation spectroscopy. Here, the temporal detection characteristics of photons described by the first order correlation function can be converted into a frequency distribution of those photons via Fourier transformation. In both cases a special configuration of heterodyne detection — called the balanced mixer — provides a built-in low-noise signal amplification by significantly increasing the detected signal via the local oscillator intensity, but using the classical noise cancelation of the balanced detection scheme.

4.2.1. General concept of optical heterodyne/homodyne detection

Conventional photon detection — also called direct detection — determines only the photon flux and is unsusceptible against the phase of light. The historical origin of heterodyne (greek: $\acute{\epsilon}\tau\epsilon\rho o$ = other, different; $\delta\acute{\upsilon}\nu\alpha\mu\eta$ = power) detection lies in the field of early radio communication (known as the "superheterodyne receiver") and goes back to the invention of Reginald Fessenden in 1901 [138]. These days, heterodyne detection concept is experiencing a revival in the field of modern coherent optical communication, where information cannot only be encoded in the real field amplitude, but also in the phase of the light field [139, 140]. Thus, heterodyne/homodyne detection gives rise to a variety of optical information encoding techniques, allowing for phase sensitive keying and frequency sensitive keying besides an improved form of amplitude sensitive keying [140, 141, 142, 143].

Heterodyne detection enables the measurement of the phase information of a signal field of frequency ω_s by mixing it with a reference field of a local oscillator (LO) of frequency ω_l. In the special case where the frequencies are degenerate $\omega_s = \omega_l$ the detection is referred to as being homodyne. The superposition of the signal field with the coherent reference field leads to a temporally varying interference pattern, i.e. a beat signal. A subsequent electronic analysis where the contribution of the reference wave is taken into account allows for the extraction of the complete complex amplitude of the signal wave.

Starting with a classical treatment a signal and local oscillator wave of the form

$$E_s(t) = A_s \ e^{i\omega_s t} \qquad \text{and} \qquad E_l(t) = A_l \ e^{i\omega_l t} \tag{4.37}$$

with the complex amplitudes $A_j = |A_j|e^{i\phi_j}$ can be considered. While the frequency ω_l and phase ϕ_l of the local oscillator field are supposed to be stable, the signal wave has a time dependent phase $\phi_s(t)$. The coherent superposition of both fields — accomplished by perfect mode matching on a 50/50 beam splitter (see fig. 4.6a)) or an 2×2 fiber optic coupler — leads to a resulting intensity

$$\begin{aligned} I \quad &\propto \quad |E_s(t) + E_l(t)|^2 \\ &= \quad |A_s|^2 + |A_l|^2 + |A_s||A_l|\big(e^{i(\omega_s-\omega_l)t+i(\phi_s-\phi_l)} + e^{-i(\omega_s-\omega_l)t-i(\phi_s-\phi_l)}\big) \\ &= \quad |A_s|^2 + |A_l|^2 + 2|A_s||A_l|\cos\big((\omega_s - \omega_l)t + (\phi_s - \phi_l)\big) \end{aligned} \tag{4.38}$$
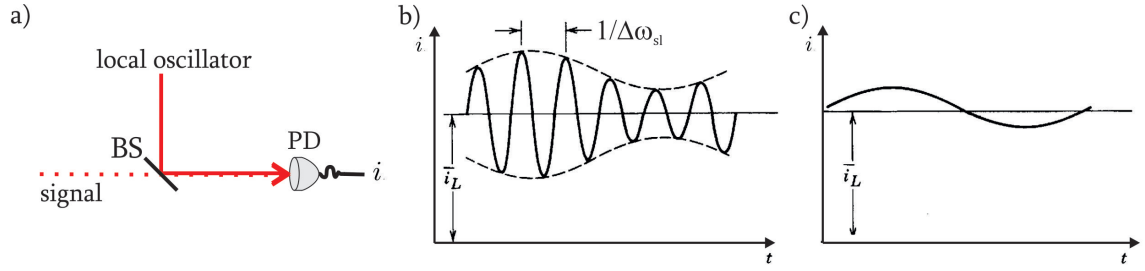
Figure 4.6.: a) Experimental configuration for heterodyne detection
b) Beat signal of the photocurrent in heterodyne detection (modified; original from [133])
c) Beat signal of the photocurrent in homodyne detection (modified; original from [133])

in direct analogy to the beat signal detection in the optical phase-locked loop in eq. (4.38) of sec. 3.3.2. From the cosine term in eq. (4.38) the beat signal oscillates at the difference frequency $\Delta\omega_{sl} = \omega_s - \omega_l$ which is called the heterodyne frequency. A photodetector measuring the superposed signal receives the power

$$P = P_s + P_l + 2\sqrt{P_s P_l} \cos\left(\Delta\omega_{sl} t + \Delta\phi_{sl}\right) \tag{4.39}$$

with the difference phase $\Delta\phi_{sl} = \phi_s - \phi_l$ and the powers of the signal and local osciallator beam P_s and P_l. In a semiconductor photodetector the power corresponds to an electric current [133] which is expressed via the relation

$$\bar{i} = \eta e \Phi = \frac{\eta e}{\hbar\bar\omega} P \ , \tag{4.40}$$

where e is the electron charge, h is Planck's constant and the mean photon flux $\Phi = P/h\bar\nu$ leads to the generation of photoelectrons with an efficiency η. For small $\Delta\omega_{sl}$ the photodetector sees an effective average photon frequency $\bar\omega = (\omega_s + \omega_l)/2$. In clear analogy to eq. (4.39) the detected photocurrent results as

$$\bar{i}^{he} = \bar{i}_s + \bar{i}_l + 2\sqrt{\bar{i}_s \bar{i}_l} \cos\left(\Delta\omega_{sl} t + \Delta\phi_{sl}\right) \ , \tag{4.41}$$

whilst for all practical purposes the DC contribution of the signal photocurrent $\bar{i}_s$ is negligibly small.

In fig. 4.6b) a sketch of the resulting beat signal is shown. It oscillates with the heterodyne frequency $\Delta\omega_{sl}$. A variation of the beat signal envelope (plotted as dashed line) corresponds to an amplitude modulation, i.e. the time dependance of $2\sqrt{\bar{i}_s \bar{i}_l}(t)$ in virtue of a time-dependent $\bar{i}_s(t)$. A variation of the phase difference $\Delta\phi_{sl}(t) = \phi_s(t) - \phi_l$ — which is due to the time dependance of the signal phase $\phi_s(t)$ — leads to a dilatation or squeezing of the fast heterodyne oscillation.[2]

Many modern experiments in quantum optics use hetero/homodyne detection as a method for reading out the phase shift an experiment imprints on a probe beam, e.g. the phase shift which an intracavity field experiences as one of the mirrors moves [144]. In fig. 4.7a) a simple scheme of such a heterodyne phase measurement is depicted. As shown in the graphics a phase lock will generally be necessary providing a coherent performance of the local oscillator and probe laser, such that the phase fluctuations measured by the heterodyne setup are true features of the experiment to be explored. The same holds true for the special case of

---

[2]In the case of a simultaneous time dependance of the field's real amplitude, that time dependance can be separated from the instantaneous phase's time dependance $\Phi(t) = \left(\Delta\omega_{sl} t + \Delta\phi_{sl}(t)\right)$ by separately measuring the signal intensity yielding the squared real amplitude only. This simultaneous measurement can, of course, only be performed for classical signal fields.
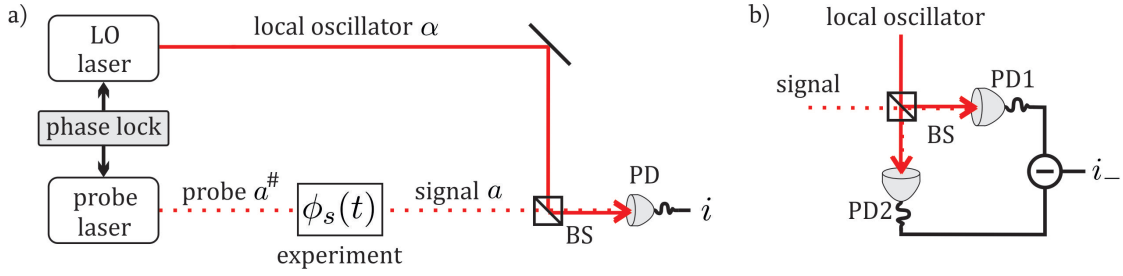
Figure 4.7.: a) Schematic configuration for the heterodyne detection of a phase shift $\phi_s(t)$ imprinted by an experiment on a probe beam.
b) Experimental configuration for balanced heterodyne detection

homodyne detection where probe and local oscillator phases ϕ_p and ϕ_l have to be locked, such that $\Delta\phi_{pl} = \phi_p - \phi_l = \text{const.}$ Thus, after the probe field has undergone eventual phase modulation by propagation through the experiment the residual oscillation gives directly information about the signal phase $\phi_s(t)$. Thus the photocurrent in this special case reads

$$\bar{i}^{ho} = \bar{i}_s + \bar{i}_l + 2\sqrt{\bar{i}_s\bar{i}_l}\cos\Delta\phi_{sl} \; . \tag{4.42}$$

The resulting characteristic homodyne detection signal is depicted in fig. 4.6c).

Accordingly, both heterodyne and homodyne detection lead to a frequency-shifted version of the original phase signal. This shift typically goes from the optic domain at hundreds of THz down to the MHz regime (for heterodyning) or even down to the DC regime (for homodyning). This makes electronic processing of the optical phase information feasible in the first place. For narrow-band filter applications on the other hand this is interesting, in that the frequency conversion enables isolating a frequency component lying arbitrarily close to others [145]. This point is to be investigated in detail later on.

Last but not least, heterodyne detection includes a built-in low-noise amplification. By choosing an appropriately high local oscillator signal the amplitude of the beat signals in eq. (4.41) and eq. (4.42) can be made desirably high.

4.2.2. Balanced configuration of heterodyne/homodyne detection

One drawback of the previous simple heterodyne detection scheme lies in the local oscillator excess noise which directly affects the detected signal. Using a symmetric detection scheme which considers both outputs of the 50/50 beam splitter (or 2×2 fiber optic coupler) is, however, able to circumvent this drawback. This configuration schematically displayed in fig. 4.7b) is called balanced heterodyne detection. It offers a significant advantage over the non-balanced detection in that it is able to discriminate between classical noise (e.g. excess noise of the local oscillator) and quantum noise of a light field and photodetector [146]. Classical excess noise of the local oscillator would reach both photodetectors with equal strength and would be subtracted in the subsequent electronics [147].

The fact, that the signal offset $\bar{i}_s$ rises with increasing local oscillator power can be bypassed by the balanced configuration as well. Note, that the waves propagating toward the photodiodes PD1 and PD2 are subject to a relative phase shift of π in the interference term caused by reflection at the combining beam splitter [148]. This means the currents at photodetector 1 and 2 are

$$\bar{i}_{1,2} = \bar{i}_s + \bar{i}_l \pm 2\sqrt{\bar{i}_s\bar{i}_l}\cos\left(\Delta\omega_{sl}t + \Delta\phi_{sl}\right) \; . \tag{4.43}$$

Following the photodetection one channel is subtracted from the other in a simple electronic circuit in order to yield the balanced signal $\bar{i}_- = \bar{i}_2 - \bar{i}_1$. For balanced heterodyne detection

one finally obtains the signal

$$\bar{i}^{he}_- = 4\sqrt{\bar{i}_s\bar{i}_l}\cos\left(\Delta\omega_{sl}t + \Delta\phi_{sl}\right) \qquad (4.44)$$

and for balanced homodyne detection we have

$$\bar{i}^{ho}_- = 4\sqrt{\bar{i}_s\bar{i}_l}\cos\Delta\phi_{sl} \qquad (4.45)$$

in contrast to the unbalanced configuration of eq. (4.42). Note, however, that for this scheme the beam splitter needs to have an exactly equal partition ratio for the reflected and transmitted waves.

4.2.3. Advantage of heterodyne and homodyne detection in terms of noise

One of the biggest advantages of heterodyning/homodyning over direct detection for few photons lies in its robustness against background noise, which does not mix with the local oscillator. This is mainly due to the strongly exclusive spatial mode matching condition. Moreover, the beat signal strength is mainly determined by the intensity of the local oscillator which can be made arbitrarily strong without suffering from concomitant classical local oscillator noise, if the balanced detection scheme is applied.

Even for simple intensity measurement heterodyne detection offers an advantage in terms of its intrinsic signal amplification providing a signal to noise advantage over direct detection [147, 149]. While in electronic systems the performance at low signal levels is principally limited by thermal noise, in quantum optics quantum noise sets the limit, as the energy of photons in the optical regime ($hc/\lambda \sim 10^{-19}$ J) lies well above thermal energies at room temperature ($k_BT \sim 10^{-21}$ J). There are two main sources for quantum noise: First, there are momentum fluctuations of electrons occurring in the optical frequency domain and second, the quantum fluctuations of the electromagnetic field itself.

The noise appearing in the signal of an optical receiver has the following contributions [133, 150, 151, 152]:

1. **Optical shot noise** (photon noise): The beating of the signal field with quantum vacuum fluctuations leads to so called shot noise fluctuations in the photon flux of optically attenuated and amplified signals (e.g. in lasers). It represents a fundamental lower noise limit[3] and gives rise to the "natural" Poissonian photon statistics with variance

$$\sigma_n = \bar{n} \qquad (4.46)$$

for a mean number of photons $\bar{n}$.

2. **Photoelectron shot noise**: For a photodetector of non-unit quantum efficiency $\eta < 1$ the generation of electron-hole pairs proceeds as a stochastic process. Here the momentum fluctuations of confined electrons at optical frequencies lead to spontaneous currents in the detector. Furthermore thermally induced random electron-hole generation leads to dark-currents even in the absence of photons. The beating of these spontaneous currents with the signal field in turn results in fluctuations of the photon absorption rate, which brings about the so called photocurrent shot noise with a variance

$$\sigma_m = \bar{m} = \eta\bar{n} \qquad (4.47)$$

for the mean number of generated photoelectrons $\bar{m}$.

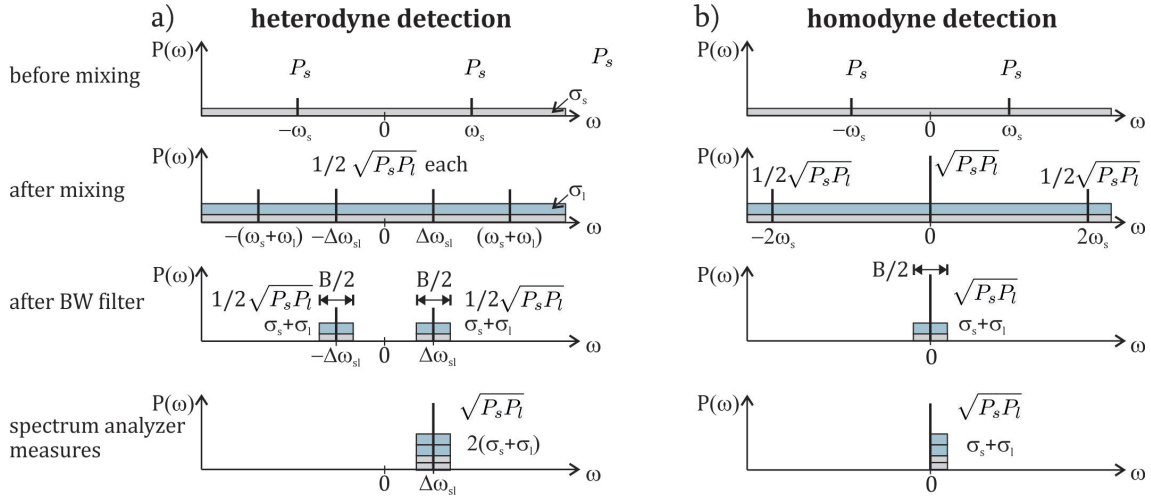[3]outperformed only by squeezed states (see e.g. [153])

Figure 4.8.: Signal and noise strength in a) heterodyne and b) homodyne detection.

3. **Excess noise** (gain noise): Noise that is inherent with the stochastic nature of the amplification process occurring e.g. in certain photodiodes (APDs), in lasers and in tapered amplifiers in the form of spontaneous emission.

4. **Circuit noise** (electronic noise): The receiver electronics processing the photodetector signal will contribute additional noise.

5. Other kinds of noise are a leakage current, $1/f$ noise, partition noise occurring at beam splitters etc.

The last three forms are classical noise. The optical and photoelectron shot noise, however, are of genuine quantum nature and therefore uncorrelated.

Taking this noise into account the mean photocurrent $\bar{i}$ inside a semiconductor photon detector has variance

$$\sigma_{\bar{i}}^2 = \underbrace{\sigma_m^2}_{\text{shot noise}} + \underbrace{\sigma_e^2}_{\text{electronic noise}} . \tag{4.48}$$

The shot noise [133, 154]

$$\sigma_m^2 = 2e\bar{i}_l B \tag{4.49}$$

with B representing the photodetector bandwidth (determined by the detector's sampling time interval $\tau = 1/2B$) is linearly dependent on the mean current $\bar{i}_l$. Thus, by increasing the LO intensity an adequately enhanced $\bar{i}_l$ can always be reached, so that the photon noise term in eq. (4.49) dominates and the circuit noise can be neglected. The signal is then said to be shot noise limited. In this case the signal to noise ratio of the heterodyne detector is given by [133, 154]

$$S/N = \frac{\bar{i}^2}{\sigma_m^2} = \frac{2\bar{i}_s\bar{i}_l}{2e\bar{i}_l B} = \frac{\bar{i}_s}{eB} = 2\bar{m} . \tag{4.50}$$

Compared to direct detection with a non-amplifying pin photodetector of a signal to noise ratio of $S/N = \bar{m}$ or an avalanche photodiode detector with the excess noise factor $F \geq 1$ and a signal to noise ratio of $S/N = \frac{\bar{m}}{F}$ heterodyne detection always provides at least a factor of 2 improvement. This statement holds even for the ideal noise-free direct detection case, where $F = 1$.

At first sight, homodyne detection — as a special case of heterodyne detection — has the same sensitivity and fundamental noise characteristics as the latter. However, a subtle difference arises when analyzed closely. In fig. 4.8 an illustration shows each step of the signal processing

in the frequency representation for both heterodyne and homodyne detection, respectively. Here, for the sake of simplicity ideal balancing is assumed and thus classical noise is omitted. While in the homodyne case the final signal contains only the residual shot noise from both the signal σ_s and the local oscillator beam σ_l integrated over the detection bandwidth $B/2$ (cf. fig. 4.8b)) in the heterodyne case the final signal actually contains the double amount of noise (cf. fig. 4.8a)). This is due to the fact that during the measurement (e.g. by a spectrum analyzer) the image signal at $-\Delta\omega_{sl}$ will be swapped onto the positive frequency side and both signal and noise will add up, such that the heterodyne signal contains the integrated shot noise of a bandwidth of B. Accordingly, homodyne detection needs half as much LO power as heterodyne detection in order do reach the shot noise limit and the intrinsic signal to noise ratio of homodyning offers a factor of two improvement over heterodyning [140, 155]:

$$(S/N)_{ho} = 1/2 \ (S/N)_{he} \ . \tag{4.51}$$

Note, however, practically it is possible that the quantum limit cannot be reached due to the saturation limit of the photodetectors prohibiting sufficiently high local oscillator power.

The theoretical advantage of homodyne over heterodyne detection can be countervailed by experimental conditions. One prominent effect would be $1/f$ noise in the detection and signal processing electronics. Another drawback for measurements aiming at the detection of the frequency distribution of a signal (especially if it is asymmetric) is the fact that the homodyne signal is folded at its central frequency ω_0 such that frequencies at some position $\omega_0 + \delta\omega$ and the corresponding mirror position $\omega_0 - \delta\omega$ appear at the same frequency position on the spectrum analyzer. This could be intervened by setting up the probe laser in a frequency fine-tunable fashion as long as either the probe linewidth is sufficiently narrow or a sufficiently narrow-band electronic filter is available enabling a sequential sampling of the frequency distribution.

In opposition to those complications heterodyne detection principally features the option for positioning the signal in a frequency region were electronic noise (e.g. of the detection system or of the surrounding electronics in the lab) is reduced. Furthermore, if — as in this case — a narrow-band filtering of the signal is desired it is convenient to translate the signal to the MHz regime, were a variety of highly optimized electronic components is available off-the-shelf.

4.2.4. Experimental requirements

The striking advantages of heterodyne and homodyne detection come along with an increase of experimental complexity. There are four main requirements:

1. a particularly stable optical local oscillator (i.e. an additional laser)

2. an optical mixer (e.g. a 50/50 beam splitter or a 2×2 fiber optic coupler)

3. two square-law detectors with identical characteristics

4. an optical phase-locked loop (as needed).

Furthermore, a perfect spatial mode matching of signal and LO beam and a perfect alignment of their polarization planes is necessary. Both signal and LO beam need to run single-mode and especially the local oscillator is required to have only minor phase and intensity fluctuations.

As square-law detector one denotes a device which transforms the AC component of the incoming electric field into a DC output being proportional to the square of the incoming field. Normal semiconductor photodiodes possess adequate square-law detectors in the optical domain. However, for high precision measurements their exact operation characteristic $i(E)$
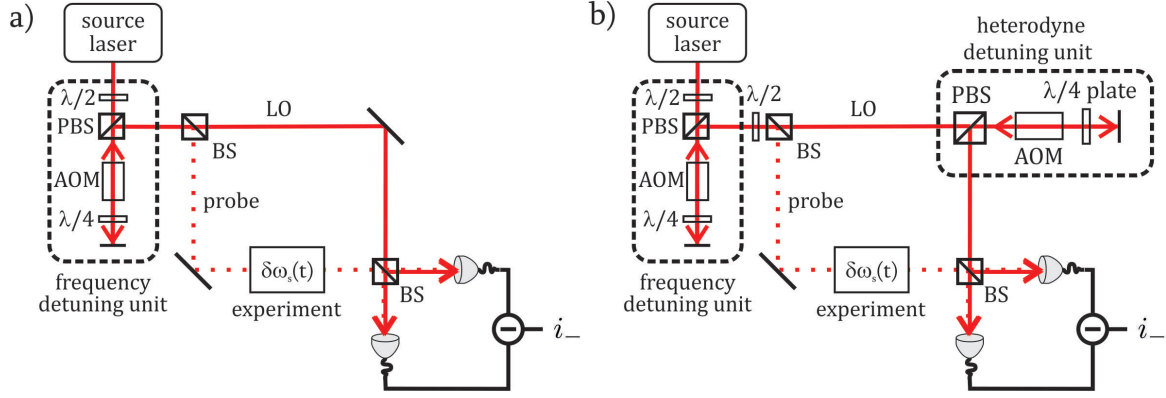
Figure 4.9.: Schematic configuration for a) a balanced homodyne and b) a balanced heterodyne detection of a frequency distribution imprinted on a probe beam by an experiment (e.g. an atomic transition profile).

— the photodiode current in dependance on the incident electric field for a given device temperature has to be taken into account. Most importantly, for balanced detection two photodetectors with exactly the same operation characteristics are necessary, in order to achieve the desired classical noise cancelation in the subtraction current. This includes the frequency response of both photodetectors to be as equivalent as possible.

At the heart of the heterodyne/homodyne detection setup lies the coherent superposition of signal and LO wave. In the general case this coherence has to be provided by an optical phase-locked loop, which accomplishes the constant phase relation between signal and LO wave by subsequently readjusting the phase of the local oscillator with respect to the probe beam phase.

Furthermore if heterodyning is performed it gives rise to the necessity of an additional device, a so called demodulator, i.e. an electronic filter removing the fast difference frequency oscillation $\Delta\omega_{sl}$ from the beat signal revealing both the amplitude modulation on the signal's envelope and the phase modulation of the fast oscillating signal. This can be rendered e.g. by means of an envelope detector. It basically transformes the shape of the heterodyne signal of fig. 4.6b) into that of a homodyne receiver fig. 4.6c).

4.2.5. Filtering on the basis of frequency conversion and electronic filters

As mentioned above heterodyne detection epitomizes not only *the* proper tool for measuring small phase variations, but furthermore offers the possibility to spectrally resolve extremely narrow lying frequency components. This is due to the fact, that electronic filtering is enabled by creating an electronic replica of the original optical signal. In virtue of the LO frequency with respect to the signal frequency the heterodyne signal can be shifted to a frequency region where frequency filtering is most conveniently performed. An electronic filter is able to restrict the signal by a much narrower effective bandwidth than any wavelength filter acting on the original optical signal. Thereby, it features a superior suppression of background light enabling the detection of extremely low signal intensities.

A convenient means of building a homodyne filter setup of low complexity is the configuration proposed in fig. 4.9a). Here, the probe and local oscillator beam originate from the same source laser and are eventually separated from each other at an unequal beam splitter. Local oscillator and probe beam are therefore inherently phase stabilized without any further ado. It might be necessary or practical to guide the source beam into a frequency detuning unit (e.g. a double-pass acousto-optic modulator (AOM) configuration) before directing it to the homodyne interferometer. This is indispensable, if the probe beam has to be scanned over a

certain frequency range in order to sample the experiment over bandwidths much wider than the laser linewidth. The signal phase $\phi_s(t)$ (or frequency distribution $\delta\omega_s(t)$) is imprinted on the probe laser during interaction with the experiment. The subsequent 50/50 beam splitter mixes signal and LO beam in order to perform the homodyne detection. The detection of the balanced difference signal can be performed over a suitable low-pass filter and a subsequent power detector.

The relative phase stability between probe and LO could be compromised by independent perturbations on both arms of the interferometer though, and eventually the implementation of a subsequent phase lock (i.e. a relative path length stabilization of the interferometer arms) might be inevitable.

This scheme can be converted to a heterodyne detection setup by inserting another frequency detuning unit into the LO beam path as shown in fig. 4.9b). If again a double-pass AOM configuration is implemented for that purpose this typically leads to a frequency difference $\Delta\omega_{sl}$ between signal and LO in the hundred MHz range. The AOM might, however, induce time-dependent phase distortions. In this respect it is of high importance to choose an AOM setup providing as low phase noise as possible, but generally the implementation of a phase-lock will be necessary. The balanced difference signal centered at $\Delta\omega_{sl}$ can then be processed in two possible ways: Following the common working principle of analog spectrum analyzers the balanced signal can be mixed with a (tunable) local oscillator wave, low-pass filtered and finally be measured by a power detector. That way, in the detection electronics one would only add a frequency down-conversion step and finally receive the same signal as in homodyning. However, in this case the signal would — according to the noise analysis in sec. 4.2.3 — have only half the power, but the same noise compared to the homodyne case. A simpler and possibly better option for heterodyne detection would rely on directly filtering the difference signal at $\Delta\omega_{sl}$ by means of a narrow-band electronic band-pass filter in the MHz range, guiding it through a demodulator (e.g. an envelope detector) and detecting the final signal power. In virtue of the LO tunability the signal can in this configuration be precisely tuned over the band-pass filter in a controlled fashion.

In any case, both homodyne and heterodyne detection provide several decisive advantages over any filtering system based on direct detection. While the signal to noise ratio is massively improved by balanced detection the signal strength does not suffer from any significant attenuation processes, but is rather subject to a built-in low-noise amplification. Such an optical amplification is utterly impossible for other optical filter device. Moreover heterodyne detection is superior to other (spatial) frequency filters based on gratings or cavities, as there is (at least no fundamental) linewidth limit in heterodyning. The limit is more a matter of electronic filter design art with low-cost off-the-shelf components, than an actual search for highly specialized and expensively manufactured components as it is the case for extremely dispersive diffraction gratings or high quality cavity mirrors. For heterodyning at difference frequencies $\Delta\omega_{sl}$ in the hundred MHz range there exists a variety of reasonably priced narrow-band electronic bandpass filters (with passbands of $10 - 20$ MHz width e.g. from Mini-Circuits, Anatech Electronics Inc. etc.) which are perfectly suited for the sampling of a narrow-band frequency distributed signal. The filter performance of such a 20 MHz passband electronic filter is at an optical wavelength of 852 nm equivalent to a filter window of 10 fm, a value completely out of reach of any optical filter device.

4.2.6. Proposal for the nanofiber EIT experiment with low intensity probe signals

The decision for either homodyne or heterodyne detection is more subtle and tied to the specific context and aim of the experiment to be performed. In the atomic physics experiment of the Rauschenbeutel group aiming at the detection of a narrow-band EIT signal it might be

most suitable to implement a homodyne detection. The reason for that lies in the necessity for tuning the probe laser over a wide range around the EIT resonance of approximately 100 MHz and the simultaneous need to perform the measurement within a time of maximally 5 to 10 ms, as the lifetime of the atoms in the trap around the nanofiber decays exponentially with a half-life of 50 ms [8]. The pair of balanced photodiodes will, however, be subject to a limited bandwidth due to their finite rise and fall times. This corresponding maximum frequency f_{pd} sets the limit for the frequency resolution with which the signal can be detected. With a pair of fast balanced photodiodes possessing a bandwidth from DC to $\tilde{f}_{crit}$ and a source laser scanning over a frequency range Δf during a measurement time of Δt the maximal optical frequency resolution results as

$$f_{\text{res}} = \frac{\Delta f}{\Delta t} \frac{1}{2\tilde{f}_{\text{crit}}} \tag{4.52}$$

The factor two in eq. (4.52) accounts for the Nyquist-Shannon sampling theorem. For e.g. the fast Thorlabs PDB430A balanced amplified photodetector with $\tilde{f}_{crit} = 350$ MHz and an optical scan over $\Delta f = 100$ MHz per $\Delta t = 5$ ms the maximal optical frequency resolution turns out to be $f_{\text{res}} = 28.5$ Hz. Even though this is a reasonably good frequency resolution for the detection of the narrow-band EIT signal it might be necessary to achieve a resolution in or below the range of some Hz. But finding a balanced set of photodiodes gets increasingly difficult for significantly higher bandwidths than some 100 MHz. Thus, in order to achieve even higher frequency resolution it will be mandatory to lower the scan range.

Facing these resolution limitations which are a direct consequence of the critical frequency of the balanced photodiode the additional frequency offset in heterodyning (featuring an electronic bandwidth filtering at $\Delta\omega_{sl}$ and subsequent demodulation) is obviously contraindicated. If heterodyning is realized via an AOM as depicted in fig. 4.9b) the difference frequency $\Delta\omega_{sl}$ is most likely to be found in the hundred MHz range. This would mean that the heterodyne signal's amplitude modulation frequency would be in the same range as the optical frequency itself. In this case, of course, an envelope detection is virtually impossible.

Apart from that, it is of great importance to implement an anti-aliasing filter perfectly matched with the chosen pair of photodiodes. In digital signal processing such a filter compensates for those frequency components lying behind half the detector's limit frequency [156, 157]. Otherwise these components would lead to 'false' contributions at frequencies actually lying before half the limit frequency causing the so called aliasing effect. In signal processing this anti-aliasing filter is placed before the sampling process. In the optical domain it is very improbable that an analog working suitable filter is available. Therefore, the detected signal will have to be carefully post-processed with a suitable anti-aliasing filter in order to compensate for sampling artefacts.

4.2.7. Phase and amplitude sensitive detection of few to single photons

The basic principle behind heterodyne and homodyne detection described above referred to the classical concept of electromagnetic waves and assumed optical signals consisting of large ensembles of photons. Here, heterodyne/homodyne detection shall be examined at low signal light levels by means of a quantum mechanical description. In this context it needs to be clarified in which way the beat signal is to be expected to change. It is initially not obvious how the former concept of two single-frequency beams generating a temporal interference pattern on the detector translates to an interference of one coherent reference beam with a signal consisting of single photons, i.e. single wave packets representing a superposition of an infinite spectrum of frequencies with varying weights, respectively. Other than coherent states

$$|\alpha\rangle = e^{-|\alpha|^2/2} \sum_{n=0}^{\infty} \frac{\alpha^n}{\sqrt{n!}} |n\rangle \ , \tag{4.53}$$
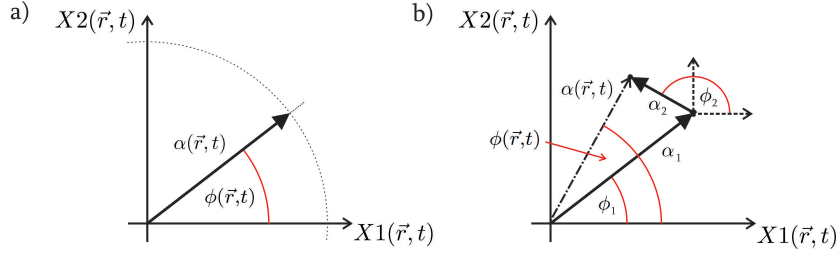
Figure 4.10.: Phasor diagrams for a) an electric field vector $\vec{E}(\vec{r}, t)$ and b) a superposition of two electric fields with amplitudes α_i and ϕ_i.

which consist of an indefinite number of photons [158, 159], Fock states

$$|n\rangle = \frac{(a^\dagger)^n}{\sqrt{n!}}|0\rangle \tag{4.54}$$

are eigenstates of the photon number operator $N = a^\dagger a$ and have an undefined phase due to the Heisenberg uncertainty relation between photon number and phase [160]

$$\Delta n \cdot \tan \Delta \phi \geq \frac{1}{2} \ . \tag{4.55}$$

Heterodyne detection is about measuring phases by means of an interferometric method. But at first sight it might be counterintuitive to perform an interferometric measurement with a state of undefined phase. Therefore, it is necessary to introduce a quantum mechanical description of heterodyne/homodyne detection in the following.

Measuring quadrature components of the light field

In a more general and abstract approach now an alternative description of the complex electric field vector

$$\vec{E}(\vec{r}, t) = \vec{E}_0(\vec{r}, t)\left(\alpha(\vec{r}, t)e^{i\omega t} + c.c.\right) \tag{4.56}$$

shall be developed. The field vector $\vec{E}(\vec{r}, t)$ is a solution of the wave equation

$$\nabla^2 \vec{E}(\vec{r}, t) - \frac{1}{c}\frac{\partial^2}{\partial t^2}\vec{E}(\vec{r}, t) = 0 \ . \tag{4.57}$$

The complex dimensionless amplitude

$$\alpha(\vec{r}, t) = \alpha_0(\vec{r}, t)e^{i\phi(\vec{r}, t)} \qquad \alpha_0 \in \mathbb{R} \tag{4.58}$$

has an alternative form in terms of the quadrature components $X1$ and $X2$ [146]

$$\vec{E}(\vec{r}, t) = \vec{E}_0\left(X1(\vec{r}, t)\cos \omega t + X2(\vec{r}, t)\sin \omega t\right) \tag{4.59}$$

with

$$X1(\vec{r}, t) = \alpha(\vec{r}, t) + \alpha^*(\vec{r}, t) = 2\,\mathcal{R}e\{\alpha(\vec{r}, t)\} = 2\alpha_0 \cos \phi(\vec{r}, t) \tag{4.60}$$

$$X2(\vec{r}, t) = i\big(\alpha(\vec{r}, t) - \alpha^*(\vec{r}, t)\big) = -2\,\mathcal{I}m\{\alpha(\vec{r}, t)\} = -2\alpha_0 \sin \phi(\vec{r}, t) \tag{4.61}$$

where $X1$ represents the real part and $X2$ the imaginary part of the complex amplitude of the electric field (4.58) [152, 146]. Therefore the angle ϕ can be expressed as

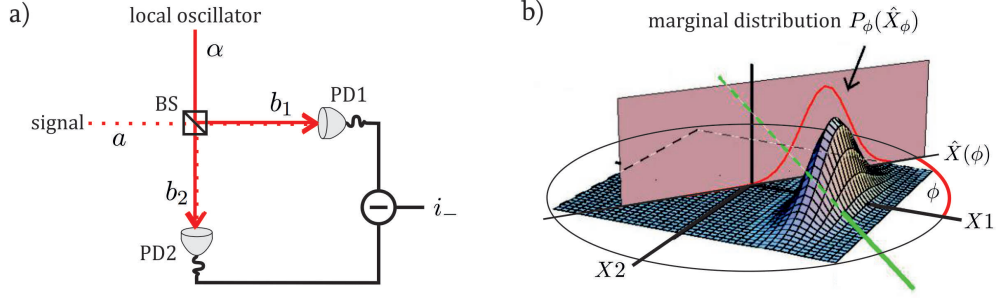$$\phi = -\arctan\left(\frac{X2}{X1}\right) \ . \tag{4.62}$$

Figure 4.11.: a) Relevant quantum fields in balanced heterodyne detection
b) Illustration, in how the quadrature components (measurable over heterodyne detection) emerge as two dimensional projections of the three dimensional Wigner function, which is not directly measurable (modified; original from [161]).

A suitable visualization of the quadratures is obtained using a phasor diagram displaying the vector $\vec{E}$ in the $(X1, X2)$ plane as depicted in fig. 4.10a). This phasor picture is especially suited for the treatment of interference phenomena (see fig. 4.10b)), of which heterodyne detection is a special case.

Quantum mechanical description of homodyne detection

For the sake of simplicity first the homodyne detection case is treated. The few photon signal field is now described by the operator a and the local oscillator is represented by the dimensionless complex amplitude $\alpha(t) = \alpha_0 e^{i\phi(t)}$ (cd. fig. 4.11). The photodetectors PD1 and PD2 are represented by the annihilation operators

$$b_1 = \frac{1}{\sqrt{2}}(a + \alpha) \tag{4.63}$$

$$b_2 = \frac{1}{\sqrt{2}}(a - \alpha) \, , \tag{4.64}$$

respectively. Here again, the change in signs is due to the phase shift of π introduced at the beam splitter [148]. The photocurrent at both detectors is then (in units of photons) given by

$$i_1 = b_1^\dagger b_1 = \frac{1}{2}\left(a^\dagger a + a^\dagger \alpha + a\alpha^* + |\alpha|^2\right) \tag{4.65}$$

$$i_2 = b_2^\dagger b_2 = \frac{1}{2}\left(a^\dagger a - a^\dagger \alpha - a\alpha^* + |\alpha|^2\right) \, . \tag{4.66}$$

The sum and difference of these currents i_1 and i_2 thus yields

$$i_+ = b_1^\dagger b_1 + b_2^\dagger b_2 = a^\dagger a + |\alpha|^2 \tag{4.67}$$

$$i_- = b_1^\dagger b_1 - b_2^\dagger b_2 = a^\dagger \alpha + a\alpha^* \, . \tag{4.68}$$

One may identify i_+ as the amplitude quadrature and i_- as the phase quadrature component. While the sum current directly gives the number of signal photons plus the intensity of the local oscillator

$$i_+ = a^\dagger a + |\alpha_0|^2 \tag{4.69}$$

the difference current shows a dependance on the local oscillator phase ϕ of the from

$$i_- = a^\dagger \alpha + a\alpha^* = \alpha_0\left(a^\dagger e^{i\phi} + ae^{-i\phi}\right) \tag{4.70}$$

$$= \alpha_0\left((a^\dagger + a)\cos\phi + i(a^\dagger - a)\sin\phi)\right) \tag{4.71}$$

Here, one can recognize the quadrature components [152] given by the opterators

$$X1 = \frac{1}{\sqrt{2}}\left(a^\dagger + a\right) \tag{4.72}$$

$$X2 = i\frac{1}{\sqrt{2}}\left(a^\dagger - a\right) \tag{4.73}$$

representing the real and imaginary field amplitudes, respectively. Thus we can write the difference current as

$$i_- = \sqrt{2}\alpha_0\left(X1\cos\phi + X2\sin\phi\right) \tag{4.74}$$

and define the generalized quadrature component as

$$X(\phi) = X1\cos\phi + X2\sin\phi \ . \tag{4.75}$$

Therefore, by controlled variation of the local oscillator phase ϕ one is able to measure an infinite set of quadrature components $X(\phi)$, each of which represents a projection of the Wigner function $P_\phi(X_\phi)$ onto the phase-space plane parallel to the plane spanned by the normal vector of ϕ as visualized in fig. 4.11b)). The Wigner function — being a quasi-propability distribution — fully characterizes the quantum state of the photon and can be reconstructed by a set of heterodyne measurements for various local oscillator phase settings [42, 162].

4.2.8. Heterodyne correlation spectroscopy

In this section correlation functions are introduced in order to investigate as to whether and how frequency information of the photon field can be extracted from few photon signal via its counting statistics. In a second step it is investigated how the experiment may benefit from the incorporation of heterodyne detection into such correlation measurements.

Coherence and correlation functions

Correlation functions contain information about the interrelationship of random variables at temporally or spatially separate points. In the special case of autocorrelation functions the correlation between one signal at some point in time t and the same signal at another point in time $t + \tau$ is evaluated. In quantum optics the correlation functions of n-th order at space-time points $\xi_j = (\vec{r_j}, t_j)$ $(j = 1, ..., 2n)$ is defined as [163, 164]

$$G^{(n)}(\xi_1 \ldots \xi_n, \xi_{n+1} \ldots \xi_{2n}) = \langle E^-(\xi_1) \ldots E^-(\xi_n) E^+(\xi_{n+1}) \ldots E^+(\xi_{2n}) \rangle \ , \tag{4.76}$$

where $\langle \ldots \rangle = tr\{\rho \ldots\}$ with the field density operator ρ and the positive frequency part (photon annihilator)

$$E^+(\xi) = \int_0^\infty au(\omega, \vec{r})e^{-i\omega t}\mathrm{d}\omega \tag{4.77}$$

and negative frequency part (photon creator)

$$E^-(\xi) = \int_{-\infty}^0 a^\dagger u^*(\omega, \vec{r})e^{-i\omega t}\mathrm{d}\omega \tag{4.78}$$

(mind the inverted sign convention; these expression correspond to the photon creators $a^\dagger, b^\dagger$ and annihilators a, b of sec. 4.2.7). Their sum gives the total complex electric field

$$E(\xi) = E^+(\xi) + E^-(\xi) \ . \tag{4.79}$$

An alternative representation of the positive and negative frequency components is given by [163, 164]

$$E^+(\xi) = \lim_{\eta \to +0} \frac{1}{2\pi i} \int_{-\infty}^{\infty} \frac{E(\vec{\xi}, t - \tau)}{\tau - i\eta} e^{-i\omega\tau} \mathrm{d}\tau \qquad (4.80)$$

$$E^-(\xi) = \lim_{\eta \to +0} \frac{1}{2\pi i} \int_{-\infty}^{\infty} \frac{E(\vec{\xi}, t - \tau)}{\tau + i\eta} e^{-i\omega\tau} \mathrm{d}\tau \ , \qquad (4.81)$$

respectively. This can intuitively be understood in that a phase variation of the photon field is equivalent to a time-displacement at the detector [165]. In terms of Glauber's correlation function formalism the counting rate of a photon detector is best described by the first-order correlation function at space-time point $\xi = \vec{r}, t$ and $\xi' = \vec{r}', t'$ as

$$G^{(1)}(\xi, \xi') = \langle E^-(\xi) E^+(\xi') \rangle \qquad (4.82)$$

The first-order correlation function $G^{(1)}(\xi, \xi)$ can therefore be identified with the intensity of the photon field $I(\xi) = E^-(\xi) E^+(\xi)$. The second-order correlation function

$$G^{(2)}(\xi, \xi') = \langle E^-(\xi) E^-(\xi') E^+(\xi') E^+(\xi) \rangle \qquad (4.83)$$
$$= \langle : I(\xi) I(\xi') : \rangle \qquad (4.84)$$

represents the correlation of two field intensities at different space-time points ξ and ξ'. Here, $: \ldots :$ denotes normal ordering.

In classical optics the coherence of a light field is referred to as its ability to reveal a signature of interference. For the purpose of a more general and accurate definition of this property it is useful to consider the n-th order normalized correlation functions [163, 66, 166]. By means of the first-order normalized correlation function

$$g^{(1)}(t, t + \tau) = \frac{G^{(1)}(t, t + \tau)}{(G^{(1)}(t, t) G^{(1)}(t + \tau, t + \tau))^{1/2}} \qquad (4.85)$$

it is possible to distinguish between incoherent light ($g^{(1)}(\xi, \xi') \geq 1$), partially coherent light ($g^{(1)}(\xi, \xi') \leq 1$) and fully coherent light ($g^{(1)}(\xi, \xi') = 1$). The second-order correlation function

$$g^{(2)}(t, t + \tau) = \frac{\langle : E^-(t) E^-(t + \tau) E^+(t + \tau) E^+(t) : \rangle}{\langle : E^-(t) E^+(t) : \rangle \ \langle : E^-(t + \tau) E^+(t + \tau) : \rangle} \qquad (4.86)$$

for a statistically stationary light field is only dependent on the time differences τ and can therefore be written as

$$g^{(2)}(\tau) = \lim_{t \to \infty} g^{(2)}(t, t + \tau) = \lim_{t \to \infty} \frac{\langle : E^-(t) E^-(t + \tau) E^+(t + \tau) E^+(t) : \rangle}{\langle : E^-(t) E^+(t) : \rangle^2} \ . \qquad (4.87)$$

As a measure of the intensity correlation over small time differences τ it characterizes the photon statistics. Generally, for light to possess second-order coherence the necessary condition is that $g^{(2)} = 1$ for all space-time points. The photon statistics is then said to be Poissonian. This is e.g. the case for ideal laser light. For statistically stationary light the crucial point is the correlation at $\tau = 0$ where for classical thermal light $g^{(2)}(0) \geq 1$, for non-classical light (e.g. Fock states) $g^{(2)}(0) \leq 1$ and for coherent light (e.g. laser light) $g^{(2)}(0) = 1$. It shall be resumed and emphasized here, that odd-ordered correlation functions $G^{(n+m)}(\xi_1 \ldots \xi_n, \xi_{n+1} \ldots \xi_{n+m})$ (with $n \neq m$) contain information about phase fluctuations of the electromagnetic field and its degree of monochromaticity, while even-ordered correlation functions $G^{(2n)}(\xi_1 \ldots \xi_{2n}, \xi_{2n+1} \ldots \xi_{4n})$ in contrast contain no phase information, but are measures of the fluctuations in the photon number, i.e. they allow for the determination to

the photon statistics [66, 167]. An illustrative example is the case of Fock states and coherent states, both of which possess first-order coherence ($g^{(1)} = 1$), but exhibit very different photon statistics and therefore differ in their second-order correlation characteristics, namely $g^{(2)}_{\text{Fock}} < 0$ and $g^{(2)}_{\text{coherent}} = 1$.

Concept of correlation spectroscopy

According to the Wiener-Khintchine theorem [126, 127] the frequency distribution of the optical field can be extracted from the counting characteristics described by the first-order auto-correlation function $G^{(1)}(\tau)$ via Fourier transform [167]

$$S(\omega) = \int_{-\infty}^{\infty} G^{(1)}(\tau) e^{-i\omega\tau} \, \mathrm{d}\tau \ . \tag{4.88}$$

The Fourier transform of the first-order correlation function thus results as the normalized intensity distribution of the signal field [168]

$$S(\omega) = \langle E^-(\omega) E^+(\omega) \rangle = I(\omega) \ . \tag{4.89}$$

Thus, in order to obtain the spectral power distribution $S(\omega)$ it is necessary to extract the $G^{(1)}(\tau)$ auto-correlation function from the photocurrents induced the detecting photodiode (with finite detection efficiency η). It turns out that the auto-correlation function of the photocurrent

$$C(\tau) = \overline{i(t)i(t+\tau)} \tag{4.90}$$

(where the overbar indicates time-averaging) reveals the auto-correlation characteristics

$$\overline{i(t)i(t+\tau)} = \eta G^{(1)}\delta(\tau) + \eta^2 G^{(2)}(\tau) = \eta\delta(\tau)\langle I \rangle + \eta^2 \langle : I(t)I(t+\tau) : \rangle \tag{4.91}$$

and a photocurrent squared mean of

$$\overline{i(t)}^2 = \eta^2 G^{(2)} = \eta^2 \langle I \rangle^2 \tag{4.92}$$

such that the photocurrent variance follows as

$$\begin{aligned}
\overline{i(t)i(t+\tau)} - \overline{i(t)}^2 &= \eta G^{(1)}\delta(\tau) + \eta^2 G^{(2)}(\tau) - \eta^2 G^{(2)} \tag{4.93} \\
&= \eta\delta(\tau)\langle I \rangle + \eta^2 \langle : I(t)I(t+\tau) : \rangle - \eta^2 \langle I \rangle^2 \tag{4.94}
\end{aligned}$$

as derived in [169]. The power spectrum of the light beam thus follows directly as Fourier transform of the photocurrent variance [166, 170]

$$S(\omega) = \frac{1}{\pi} \int_0^{\infty} \cos\omega\tau \ \lim_{t\to\infty} \left(\overline{i(t)i(t+\tau)} - \overline{i(t)}^2 \right) \, \mathrm{d}\tau \ . \tag{4.95}$$

Combination of correlation spectroscopy with heterodyne/homodyne detection

In combining the concept of correlation spectroscopy with the technique of heterodyne/homodyne detection it is possible to reveal the frequency information of a narrow-band spectral feature while providing a high signal to noise ratio including a built-in low-noise amplification. The principle to extract the spectral density directly from the photocurrent's statistics via a fast fourier transformation (FFT) is an interesting alternative to the method mentioned in sec. 4.2.5 and sec. 4.2.6, which basically projected the frequency distribution into an analogue narrow-band electronic band-pass filter. The employment of a direct FFT, however, comes along without any filter system.
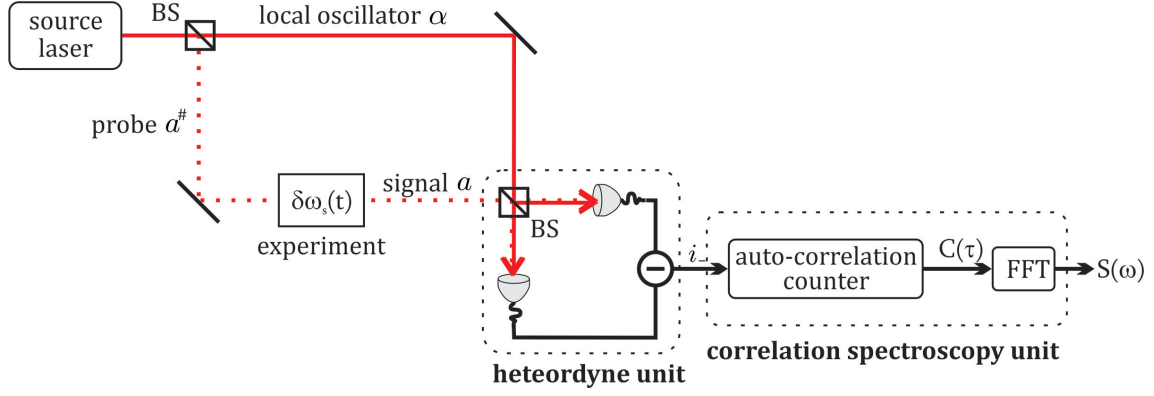
Figure 4.12.: Setup for combined balanced heterodyne correlation spectroscopy

This combined technique has recently been applied in experiments connected to the fine-resolved frequency analysis of very weak optical signals in quantum optics and atomic physics. A balanced heterodyne detection technique was successfully implemented for the frequency analysis of motional sidebands of single trapped ions, which arise due to the oscillation of the ion in the harmonic trap potential [171]. In that case an astonishing frequency resolution of 61 mHz could be achieved.

On the basis of this technique ultra-high frequency resolution is enabled for even few to single-photon signals. It is thus worthwhile considering the implementation of a homodyne/heterodyne correlation spectroscopy for the nanofiber experiment in the Rauschenbeutel group, especially if EIT is to be investigated on the single-photon level.

Part II.

Experiment and Measurements

5. Experimental Setup and Characterization of the OPLL

The first section of this chapter is intended to give a short introduction to the nanofiber based atom trap experiment performed in the Rauschenbeutel group. The parts of the experiment which have been treated in this thesis follow below and in the two subsequent chapters. The second part of this chapter represents a report documenting the reconstruction of the optical phase-locked loop. It is completed by both an in-loop and an out-of-loop measurement and characterization of the residual phase noise between control and probe laser.

5.1. The experimental setting of the nanofiber experiment

The future aim of the main experiment is to probe electromagnetically induced transparency (EIT) in cold Cs atoms trapped in the evanescent field around an ultrathin optical fiber. The trap is based on a theoretical proposal of Le Kien et al. of 2004 [172] on a two-color evanescent fiber trap. Following this proposal radial confinement of the Cs atoms is provided through a suitable superposition of a red and blue detuned dipole trap beam sent through the fiber partly propagating as evanescent field around the nanofiber (see fig. 5.1a)). Azimuthal confinement is induced by the usage of linear polarized red and blue detuned light modes as visualized in fig. 5.1c), which brakes the rotational symmetry. The trap configuration chosen for the Rauschenbeutel experiment is a refined version of that nanofiber trap, which includes an additional spatial confinement in the longitudinal direction [9]. By coupling in the red detuned light mode from both ends into the nanofiber a standing wave is generated as plotted in fig. 5.1b). This leads to an effective 3d confinement of Cs atoms lined up above and below the fiber as depicted in fig. 5.1d). Thus, this system possesses a novel twofold 1d optical lattice of Cs atoms. With the current trap configuration the Cs atoms are trapped in an approximate distance of 230 nm from the fiber surface, while the nanofiber diameter is around 500 nm over the tapered region of approximately 5 mm length [8].

For the purpose of loading the Cs atoms into the nanofiber trap they first have to be trapped and cooled in the vicinity of the nanofiber. This is accomplished with a magneto-optical trap (MOT) whose center point is in the vicinity of the nanofiber. The MOT loading procedure

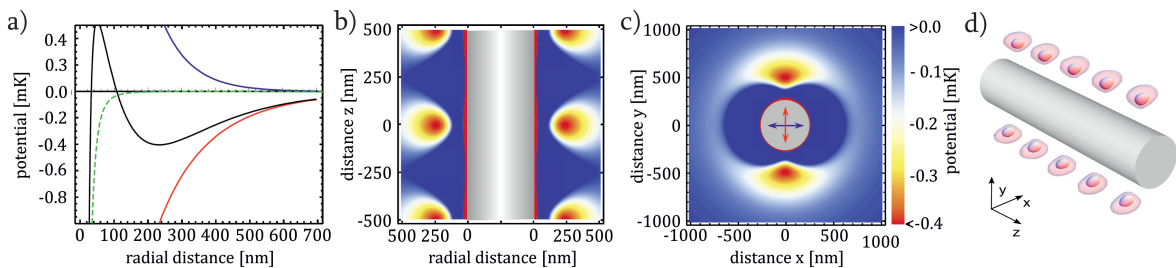**Figure 5.1.:** Depiction of 3d confinement of Cs atoms in an evanescent nanofiber trap accomplished via a) the suitable superposition of a red and blue detuned trap beam, b) the formation of a standing wave of the red detuned beam and c) using linear polarized red and blue detuned light modes. d) Visualization of the resulting twofold 1d optical lattice trapping potential wells for Cs atoms (all modified; originals from [9])
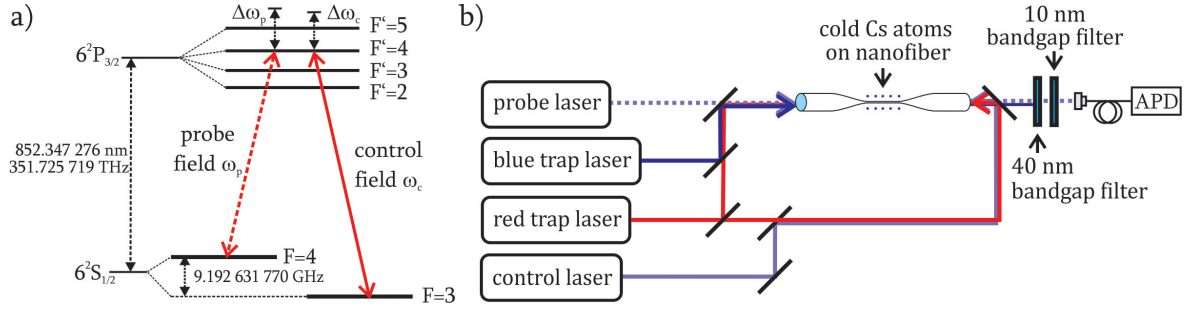
Figure 5.2.: a) Hyperfine level scheme of the Cs D2-line in cesium (line data adopted from [173]) b) Scheme of the experimental setup probing EIT in Cs atoms trapped around a nanofiber

takes ~ 2 s. Within the following 80 ms the atoms are cooled further and transferred into the nanofiber trap. It has turned out that letting the two-color nanofiber trap run continuously leads to best trapping efficiencies around the nanofiber [9]. In this experiment the blue and red detuned fiber trap beams are realized by a 1064 nm and a 780 nm laser beam being both far detuned with respect to the D1 (894 nm) and D2 (852 nm) lines in Cs. The cooling beams are both on the D2 line of Cs, namely on the $6^2\,S_{1/2}\ F = 4 \to 6^2\,P_{3/2}\ F' = 5$ transition and a repumper is implemented on the $F = 3 \to F' = 4$ line.

The levels, which will be used for the realization of EIT lie on the D2 line of Cs as well and are shown in fig. 5.2a). The weak probe laser couples between the $F = 4 \to F' = 4$ levels and the strong control laser dresses the $F = 3 \to F' = 4$ transition. The $6^2\,S_{1/2}\ F = 3 \to 6^2\,S_{1/2}\ F' = 4$ transition is dipole forbidden. For the detection of the few photon EIT probe signal an avalanche photodiode (APD) type C30902E from PerkinElmer will be used.

5.2. Aims and topics of this thesis

The main experiment can be divided into three parts: The first contains the laser beam preparation including frequency and phase stabilization setups. The second is the central part of the experiment consisting of the vacuum chamber containing the nanofiber, the Cs reservoir and the atom trapping and cooling arrangement. The third is the detection unit, where the separation of the weak EIT probe signal from all other co-propagating laser beams is accomplished and its power is measured.

In the context of this thesis parts of the first and third category of the main experiments were treated. Specifically, the first major part of the present work was devoted to the beam preparation of the EIT probe and control laser as well as their optical phase-locked loop (OPLL). The structural plan of the probe beam preparation setup was developed by the group's PhD students and the control beam preparation setup as well as the OPLL unit was designed and constructed within the framework of a Diplom thesis [15] in 2010. After the experiment moved from Mainz to Vienna in November/December 2010 these setups were partly rebuilt, completely readjusted and inspected for their performance in the context of this thesis. The other part of the present work deals with the investigation of two options for narrow-band filtering of the EIT probe signal. Both filtering with a diffraction grating and filtering based on heterodyne/homodyne detection techniques were theoretically elaborated. Finally, a homodyne test setup was realized where a saturation spectroscopy took the role of the nanofiber experiment.
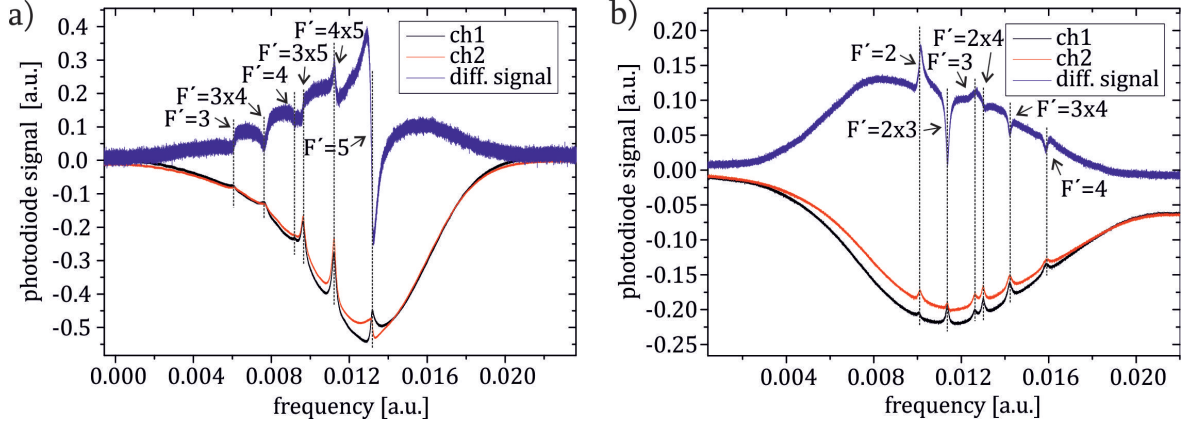
Figure 5.3.: Experimentally achieved polarization spectroscopy signals revealing the hyperfine transitions on the Cs D_2 line of a) the probe laser from $F = 4 \rightarrow F'$ and b) the control laser from $F = 3 \rightarrow F'$. (The expression $i \times j$ denotes the crossover resonance between level i and j.)

5.3. Probe and control laser preparation

Both lasers are extended cavity diode lasers and are equipped with both an injection current and temperature controller each. The probe laser is a Sacher LION-SYS-500 operating in Littman-Metcalf configuration. The control laser is a home made diode laser of the Littrow type presented in [99] with a Spectra Diode Labs SDL-5401 laser diode. For the experiment these lasers need to be stabilized to optical transitions between distinct hyperfine levels of the Cs D_2 line as described above. The frequency stabilization of the control laser is implemented via polarization spectroscopy on a room temperature Cs cell. For that purpose a compact polarization spectroscopy configuration is implemented based on the setup presented in [120]. In fig. 5.4 a scheme of the optical pathways of the laser preparation setup is depicted. The optical path of the probe laser is drawn in green, the one of the control laser in red, and paths where probe and control beam propagate in a mode-matched superposition are marked in blue. The probe laser is both phase and frequency stabilized with respect to the control laser via an optical phase-locked loop designed in [15]. For phase-lock independent experiments the probe laser, however, was provided with a separate polarization spectroscopy unit as well. Typical experimentally achieved polarization spectra of both the probe and the control laser lock transitions are displayed in fig. 5.3a) and b), respectively.

In fig. 5.4 the double-pass AOM configurations (see e.g. [174, 175]), which shift the optical frequencies of certain branches of the probe and the control beam are displayed. They provide an option for detuning the optical frequencies by $\pm(150 - 250)$ MHz with respect to the actual lasing wavelength. This range is determined by the AOM modulation efficiency

Table 5.1.: Settings of both the probe and control laser preparation setup (frequencies determined based on transition values given in [173]) (see text for details).

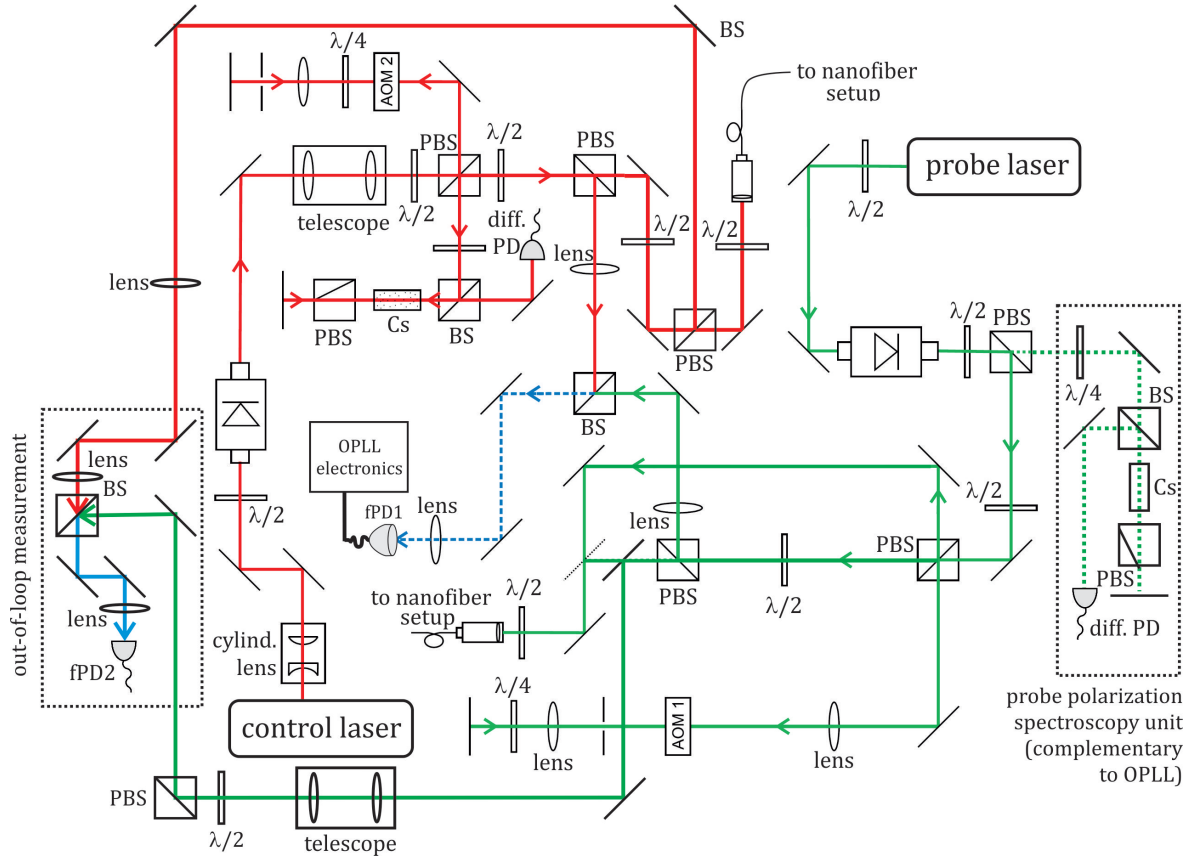| parameter	probe laser	control laser	beat signal freq.
lasing frequency (corresp. transition):	$F = 4 \rightarrow F' = 3$	$F = 3 \rightarrow F' = 4$	
Cs lock resonance:	$F = 4 \rightarrow F' = 3$	$F = 3 \rightarrow F' = 2 \times 4$	
AOM frequency:	100.621 MHz	88.114 MHz	
frequency shift of beam:	$+201.242$ MHz	$-176,228$ MHz	
light to nanofiber:	$F = 4 \rightarrow F' = 4$	$F = 3 \rightarrow F' = 4$	
beat signal on fPD1 & fPD2:	$F = 4 \rightarrow F' = 3$	$F = 3 \rightarrow F' = 4$	9.393874 GHz

Figure 5.4.: Detailed scheme of the optical beam path for the preparation of probe and control beam (modified; original from [15])

characteristics. In the case of the probe laser the AOM1 is set up in a branch parallel to the Cs polarization spectroscopy lock unit and it is implemented in the +1st diffraction order. This leads to a positive frequency shift of the post-AOM-beam with respect to the Cs lock frequency (and thus the probe lasing frequency) of two times the AOM1 frequency. For the control laser the AOM2 is passed in −1st order sequentially before the beam propagates through the Cs lock, such that the control lasing frequency is effectively locked to plus two times the AOM2 frequency with respect to the Cs lock transition. The different beam branches coupled out or detected at the various ends of the beam preparation setup in fig. 5.4 will correspond to different optical transition frequencies depending on their path through the setup experiencing eventual frequency shifts or optical beating with another laser beam. In table 5.1 the AOM frequency settings used for the probe and control laser preparation and corresponding optical transitions in the various output ports are listed. In order to yield the desired $F = 4 \to F' = 4$ transition frequency on the probe and the $F = 3 \to F' = 4$ transition frequency on the control output coupler to the nanofiber experiment the Cs polarization spectroscopies of the probe has to be locked to the $F = 4 \to F' = 3$ hyperfine transition and the control laser spectroscopy has to be locked to the $F = 3 \to F' = 2 \times 4$ crossover resonance. Of course, the probe frequency lock is finally taken over by the optical phase-locked loop, but still it will be necessary to preparatorily tune the probe laser to the vicinity of that $F = 4 \to F' = 3$ hyperfine feature by means of adjusting the ECDL cavity piezo while observing the probe polarization spectrum before actually starting the OPLL.
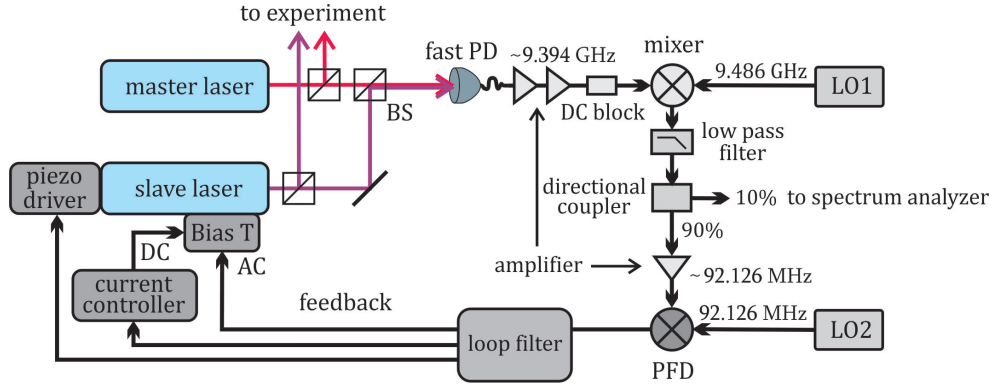
Figure 5.5.: A scheme of the optical phase-locked loop developed in [15] slightly modified in this work.

5.4. The implementation of the optical phase-locked loop

The superposed beat signal of probe and control laser on the fast photodiode (fPD1) will — in accordance with the previous discussion — consist of the probe on the $F = 4 \rightarrow F' = 3$ and the control on the $F = 3 \rightarrow F' = 4$. The set frequency of this beat note at $\Delta\omega^{set} = 9.393\,874$ GHz is very high and thus a very fast photodetector is needed. For this purpose an GaAs PIN detector from EOT (type ET-4000) with a very high cut off frequency of 12.5 GHz is implemented. For the purpose of maximal interference of both beams on the fast photodiode their powers were chosen to be 4.5 mW each (incidence power limit of the ET-4000: 10 mW). As previously described in sec. 3.3.2 and displayed in fig. 3.6 the OPLL converts this signal down by mixing it with a reference signal from a first local oscillator LO1. The resulting difference frequency between $\Delta\omega^{set}$ and $\Delta\omega_{LO1}$ is one input to the phase sensitive detector (PSD) and is to be compared with the other input from a second local oscillator signal LO2. In this OPLL, instead of a normal PSD a phase-frequency detector (PFD) was chosen, which is able to detect both the phase and frequency difference between its two inputs [15]. The operating bandwidth of the PFD determines the necessary detuning of $\Delta\omega_{LO1}$ from $\Delta\omega^{set}$. In the context of the Diplom thesis [15] the digital phase-frequency detector HMC439QS16G from Hittite Microwave Corporation with a frequency input range of 10–1300 MHz was deemed appropriate. Thus the combination of a Kuhne local oscillator MKU LO 95 PLL running at $\Delta\omega_{LO1} = 9.486$ GHz and a frequency tunable Agilent N9310A signal generator representing the LO2 at $\Delta\omega_{LO2} = 92.126$ MHz was chosen. Here, the Agilent signal generator provides a 10 MHz output, which is fed into the LO1 in order to stabilize it with respect to the LO2.

For the present thesis the optical phase-locked loop was rebuilt in accordance with the plans and descriptions found in [15]. After each step of the radio frequency electronics depicted in fig. 5.5 the actual values obtained on the spectrum analyzer were compared with the theoretically expected signal strengths and frequencies. In compliance with the limits for the input and output values of the microwave components and their prescriptive voltage supply given in the respective data sheets the beat signal strength in front of the phase sensitive detector was found to deviate from the values found in [15]: here, it was measured to be +15.6 dBm, which is around ten times higher than specified in [15]. The reason for this deviation could not be identified. In order not to exceed the permitted input power of the Hittite digital phase-frequency detector of +10 dBm the fourth amplifier (Mini-Circuits ZFL-500HLN+) used in [15] directly before the PFD was thus omitted and additionally the power supply of the preceding third amplifier (Mini-Circuits ZFL-500LN) was chosen to be 12 V instead of 15 V. That way the signal input to the PFD could be reduced to a non-hazardous value of +6 dBm. This corresponded to a signal strength of −19 dBm at the 10% output of

the directional coupler (Mini-Circuits ZFDC-10-1), where the power spectral density of the beat note phase noise can be observed while the OPLL is running.

Within [15] a special loop filter combination was developed driving three feedback paths. Slow phase fluctuations up to 160 Hz are selected by the loop filter to actuate the laser resonator piezo element. Fluctuations within the range from some 100 Hz to 100 kHz are filtered out and sent to the probe's laser current controller as a modulation input. A very fast path for phase fluctuations above 100 kHz up to 100 MHz uses the AC input of a Bias-T directly attached to the laser diode, while the injection current controller output is connected to the Bias-T DC input. The slow and medium path loop filters are basically PI controllers. The fast path loop filter presented in [15] was designed empirically based on computer simulations.

5.5. OPLL performance inspection by both an in-loop and out-of-loop measurement

It is common practice to accomplish the performance inspection of a stabilization system by an analysis of the error signal given out by the controller. In [15] the performance inspection of the designed OPLL was carried out by an observation of the beat note signal tapped at the directional coupler after the mixer and low pass filter (see fig. 5.5). It has to be taken into account that these measurements neither determine the absolute phase stability of the slave (i.e. the probe laser) nor do they prove the relative phase stability between master and slave laser in the strict sense. This is due to several circumstances: 1) The beat note phase noise characterization does not characterize the performance of the VCO (i.e. the probe laser) alone, but includes the contribution of the reference oscillator (i.e. the control laser) as well. Thus, phase noise of the control laser propagates through the phase-locked loop and is acquitted from the point of view of the PFD by actuating the probe laser. However, this effectively leads to the control laser noise being conveyed to the probe laser. Accordingly, even if the beat signal at the directional coupler indicates proper phase stability the probe laser's phase might actually fluctuate significantly. Consequently, at the most a stable and narrow beat signal at the position addressed above lets one conclude for a high *relative* phase stability between probe and control laser. 2) But not even relative phase stability is boundlessly ensured, as one has to consider the PLL behind the optical detection to work essentially toward a vanishing error signal. It is important to note that eventual noise added to the beat signal during the detection process on the fast photodiode or during the subsequent microwave signal processing will be spuriously antagonized by the PLL in the form of feedback to the probe laser. This means that all OPLL artifact noise will directly be conveyed to the probe laser's phase performance; indeed the better the PLL, loop filter and actuating units work, the worse that preceding noise will be conveyed to the probe laser.

A solution to the first circumstance is difficult, as for the inspection of phase noise at optical frequencies one would always be restricted to a heterodyne detection technique involving another laser. In many, experiments, however an absolute phase stability is not necessary anyway, but only a relative phase coherence between the probe and control laser is desired. Considering the second point, however, it should have become clear that an objective phase-lock performance inspection has to be accomplished from 'outside' the optical phase-locked loop, not by means of the error signal from 'within' the OPLL. For that reason in the present thesis a second fast photodiode (fPD2) was set up for an 'out-of-loop' phase noise inspection of the beat signal as depicted in fig. 5.4. Fig. 5.5 shows the in-loop and out-of-loop outputs, at which the OPLL characterization measurements were recorded in this work.

The 'out-of-loop' measurement of the beat signal's phase noise power spectral density should be as independent from the actual OPLL as possible and contain as little additional noise sources as needed in order to obtain a meaningful conclusion about the OPLL performance.
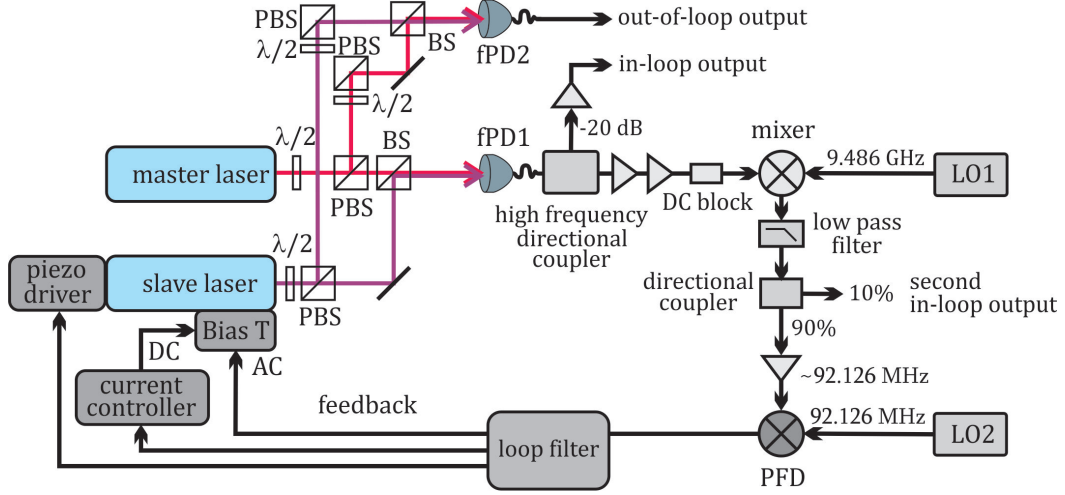
Figure 5.6.: A scheme of the optical phase-locked loop developed in [15] showing the modification for the performed in-loop and out-of-loop beat signal measurement.

This supposes the out-of-loop measurement to contain no more than a fast photodetector of low noise at best. Here, an Hamamatsu ultrafast MSM photodetector type G4176-03 was chosen as out-of-loop photodiode, followed by a Mini-Circuit Bias-Tee type ZX85-12G+. On the other hand, it is desirable to obtain two directly comparable measurements of the beat signal from inside and outside of the loop. This means, the in-loop signal has to be tapped not until after amplification and mixing with the LO1, but directly after the signal detection, because each additional electronic processing step may tamper with the original beat signal to be compared. Also the spectrum analyzer characteristics may vary for different signal strengths and frequency domains. For this purpose the OPLL setup in fig. 5.5 was slightly modified by inserting a second directional coupler (Agilent 773D) directly behind the fPD1. This directional coupler is specifically designed for high signal frequencies from 2 to 18 GHz and offers a -20 dB attenuated coupling output, which can be used for signal inspection. The basically unchanged photodiode signal is parallely forwarded from the main line output over to the original OPLL electronics. That way only a minor intervention of the original OPLL design is ensured. It is, however, necessary to amplify the very small signal from the -20 dB attenuated coupling output in order to obtain a signal of strength comparable to that of the out-of-loop measurement. For this purpose a Mini-Circuit ZX60-14012L+ amplifier suited for up to 14 GHz and offering a 12 dB amplification was implemented at the directional coupler output before directing the signal to the spectrum analyzer. The out-of-loop detection was realized as depicted in fig. 5.4 on the fPD2.

5.6. Characterization of the phase lock performance

In the following the outcome of the measurements performed at the OPLL are presented. To begin with, some information concerning the data evaluation from the spectrum analyzer is given followed by the presentation of the in and out-of-loop measured noise power spectral densities of the beat signal.

5.6.1. Data analysis of the in-loop and out-of-loop beat signal data

In order to normalize the noise power density measured with a specific resolution bandwidth RBW to the conventional 1 Hz bandwidth it is necessary to subtract $10\log(RBW)$ from the measured data [132, 176] (here log denotes the logarithm to the base 10). Furthermore, if

a noise correction is performed, the noise data has to be subtracted taking into account the logarithmic data representation. Assuming, the original measurement data points x are given in dBm (decibel with respect to 1 mW) the noise and bandwidth corrected data follow as

$$
\begin{aligned}
x_{\text{corrected}}[\text{dBm/Hz}] &= 10\Big(\log\big(10^{(x[\text{dBm}]/10)} - 10^{(x_{\text{noise}}[\text{dBm}]/10)}\big) - \log\big(RBW\big)\Big) \\
&= 10\log\left(\frac{10^{(x[\text{dBm}]/10)} - 10^{(x_{\text{noise}}[\text{dBm}]/10)}}{RWB}\right). \quad (5.1)
\end{aligned}
$$

In order to convert these data to the more demonstrative and convenient representation of dBc (decibel with respect to the carrier peak power x_{carrier}) the $x_{\text{corrected}}$ have to be processed according to

$$
x_{\text{corrected}}[\text{dBc/Hz}] = 10\log\left(\frac{10^{(x_{\text{corrected}}[\text{dBm/Hz}]/10)}}{10^{(x_{\text{carrier}}[\text{dBm/Hz}]/10)}}\right). \quad (5.2)
$$

Moreover, the power spectral density is conventionally given as a function of the offset frequency f from the carrier peak, rather than in dependance on the actual optical or electrical signal frequency. For that reason all spectra were subject to a frequency offset correction. The center frequency of the beat signal was observed to fluctuate by approximately ± 20 Hz per ~ 30 s around a central position of 9393.872892 MHz. This drift required an appropriate frequency correction for each curve measured individually.

For the detection of both the in-loop and out-of-loop signal an Anritsu MS2718B digital spectrum analyzer with a fine resolution bandwidth of only 1 Hz was employed. This analyzer type gives out 551 data points for each power spectrum measurement, whereas each data point represents averaged values from several internal measurements. During the data analysis an important fact about the data acquisition of the Anritsu MS2718B was found: Measurements with a frequency span smaller than 551 Hz with the minimal resolution bandwidth of 1 Hz lead to unusable data, as the analyzer gives out multiple power values per frequency component. These power values can not be averaged by post-processing as the manufacturer confirmed. Thus, the scan with the finest RBW of 1 Hz was conducted at a span of 1 kHz.

5.6.2. Double-sideband power spectral densities of the beat signal

Fig. 5.7a)-f) shows the double-sideband power spectral density $\mathcal{L}^{\text{DSB}}(f)$ (cf. eq. (3.31)) of the in-loop (green line) and out-of-loop (blue line) beat signal for a selection of different frequency spans. All spectra were subject to a resolution bandwidth correction. For a better classification of the measured data the curves are accompanied by the background noise curves (red line). The spectra are normalized to dBc with respect to the carrier peak power of $x_{\text{carrier}} \simeq -68.5$ dBm of the in and out-of-loop beat signal, which was determined at a span of 1 kHz using the minimal resolution bandwidth of 1 Hz.

In fig. 5.7a) the power of the main carrier peak is distributed between $f = -35$ Hz to $f = 35$ Hz. First spurious noise peaks can be identified to originate from the mains frequency at 50 Hz and its harmonics with peak powers below -65 dBc. As already asserted in [15] the noise peaks distributed around the 2 kHz region which can be seen in fig. 5.7b) can be attributed to unidentified electronic noise sources in the lab similarly to the relatively pronounced noise peak at $\simeq 28.5$ kHz observed in fig. 5.7c). In fig. 5.7d) a very weak crosstalk contribution between the medium and the fast control paths can be seen in the region around 300 kHz. The large bumps at around 2.4 MHz mark the border of the overall loop bandwidth of the OPLL. Fig. 5.7e) reveals that the beat signal phase noise distribution touches the noise floor at approximately 8 GHz. It turned out, that this noise floor is dominantly determined by the spectrum analyzer characteristics, i.e. it persists even for the 'free' spectrum analyzer without cable connection to the experiment.
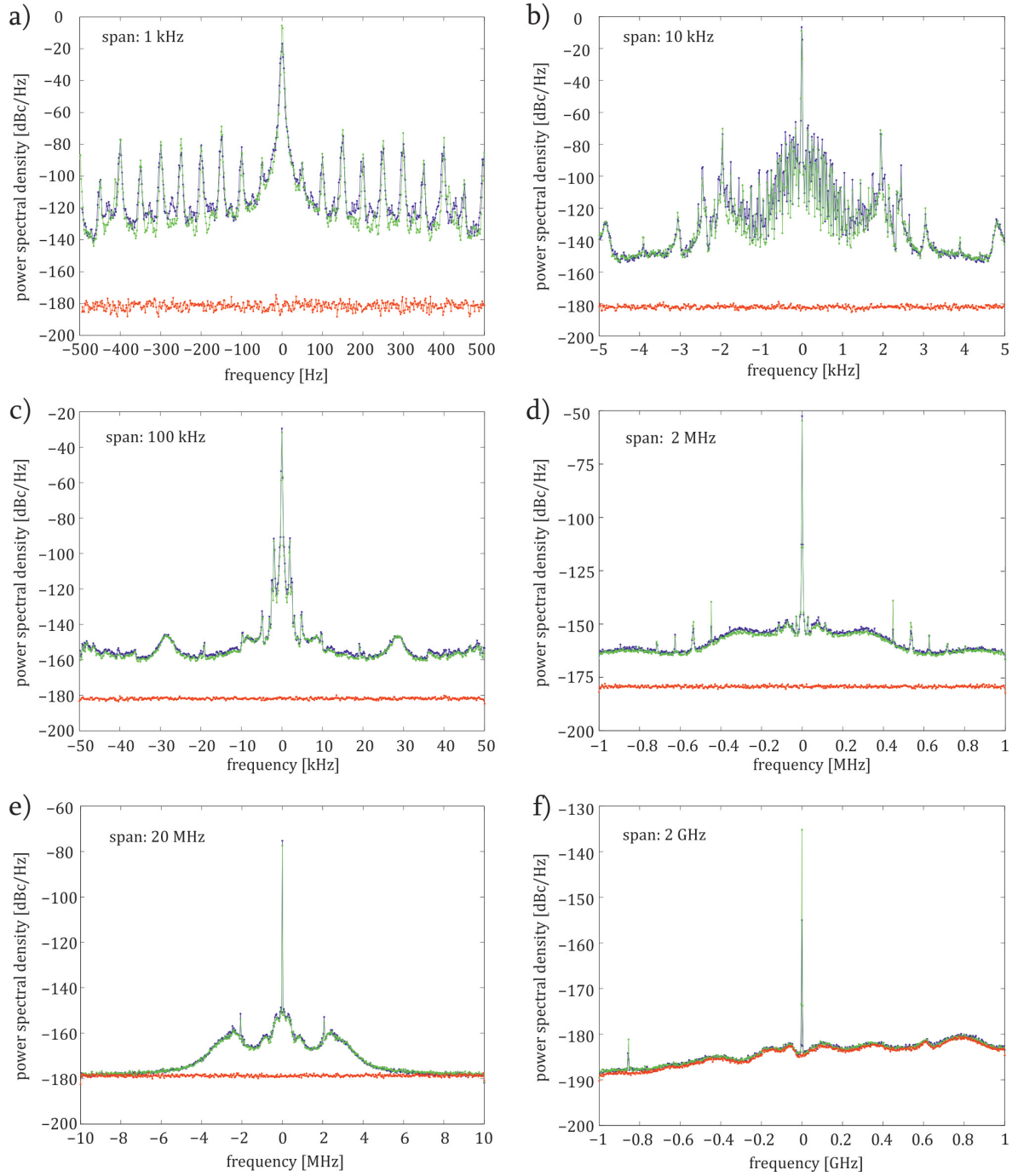
Figure 5.7.: Double-sideband noise power spectral densities $\mathcal{L}^{\mathrm{DSB}}(f)$ measured at varying spans and resolution bandwidths (blue: out of loop measurements, green: in loop measurements, red: noise background). On all spectra a bandwidth correction was performed.

For measurements with a very small frequency span it was noticed that the beat signal peak moves around the central frequency value of 9393.872892 MHz with a variation amplitude of approximately $20 - 30$ Hz within half a minute. On the other hand, for measurements of small span and fine resolution bandwidth the measurements took several seconds. These circumstances made the determination of the 3 dB width (FWHM) of the carrier peak very difficult. In [15] a measurement with a resolution bandwidth of 10 Hz gave rise to a beat signal linewidth (FWHM) of below 10 Hz. Here, with a resolution bandwidth of 1 Hz the carrier could be estimated to have a width of around 5 Hz. As a possible reason for this

Figure 5.8.: Single-sideband noise power spectrum for offset frequencies from the carrier ranging from $f = 35$ Hz to 1 GHz (the individual DSB curves were subject to noise correction (see text))

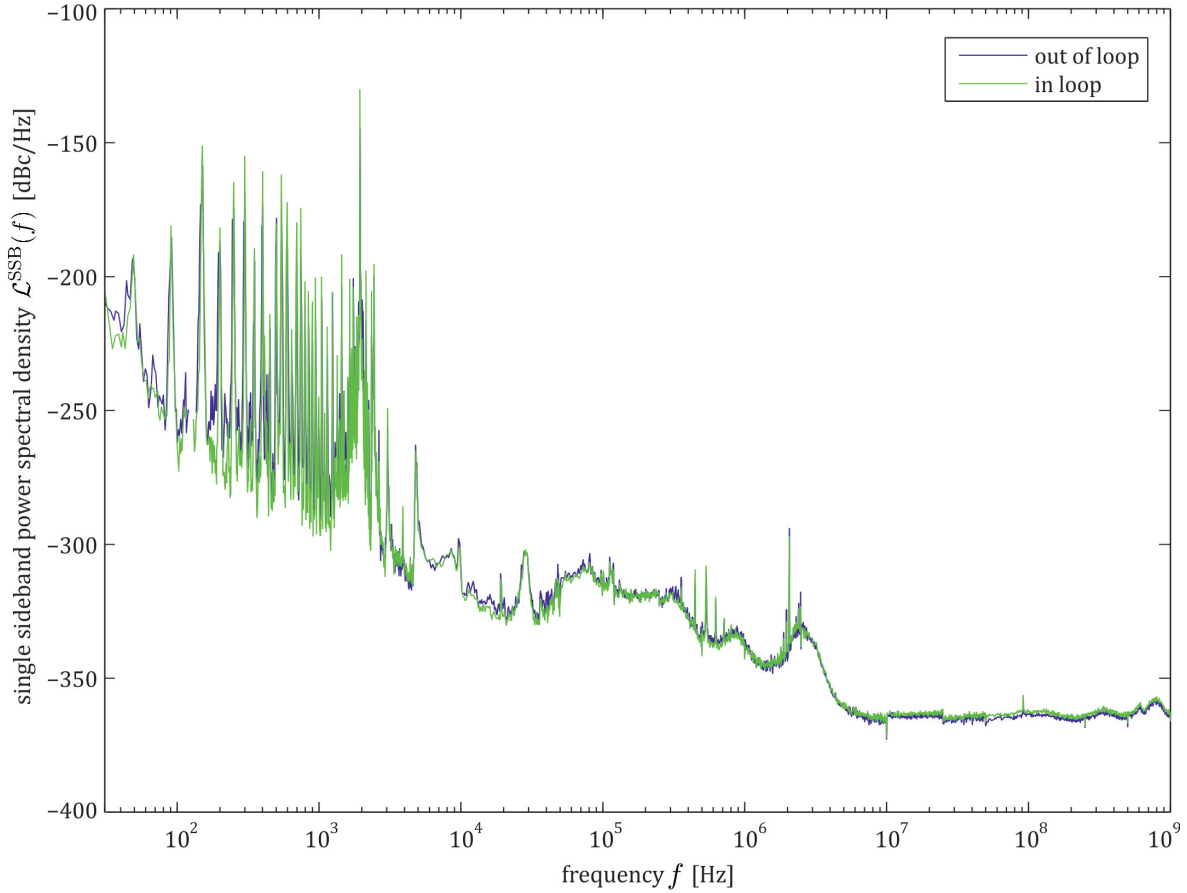residual oscillation of the beat signal the frequency error of the Agilent N9310A signal generator (used as LO2 and providing the 10 MHz reference onto which the LO1 is stabilized) can be considered. After consultation with Agilent the reference frequency error is given approximately by $\pm(2 \cdot 10^{-6})$, i.e. ± 20 Hz. The uncertainty of the RF frequency output is given as ± 20 MHz $\cdot f_{LO2}/(10$ MHz$)$, i.e. 180 Hz in this case. With respect to the phase-frequency detector these two errors are anti-correlated and can thus be expected to cancel partially. The overall frequency error of the beat signal can hence be assumed to be approximately 160 Hz. As a consequence, this frequency error will lead to a washed out carrier peak in the DSB power spectral density and can be considered as the reason for the observed residual frequency oscillation of the carrier peak in time. It is questionable, if the resulting relative frequency error between the control and the probe laser is acceptable for the performance of EIT in Cs at the nanofiber.

5.6.3. Single-sideband power spectral density of the beat signal

In fig. 5.8 the corresponding single-side band phase noise spectrum $\mathcal{L}^{\mathrm{SSB}}(f)$ (cf. eq. (3.31)) of the in-loop and out-of-loop beat signals are displayed within the offset frequency range from 10 Hz up to 1 GHz from the carrier. These spectra represent a composition of 14 individual measurements of the double-side band spectra received for different frequency spans and correspondingly adapted resolution bandwidths around the carrier peak, respectively. All single measurement curves were subject to noise and resolution bandwidth correction according to eq. (5.1). Even though a noise correction was performed on the data the resulting

phase noise spectrum between $f = 5$ MHz and $f = 1$ GHz has to be treated with caution: in this frequency regime the logarithmic representation brings features to light which are more a signature of the noise correction procedure (suffering from the stochastic nature of the noise curve) than of the actual phase noise spectral density of the beat signal. Finally, the data were rescaled to dBc/Hz and combined such that for each offset frequency sequence the measurement with the finest resolution bandwidth available was adopted. This technique comes along with a certain degree of information loss over the total spectral range: The further away a considered phase noise component is from the carrier peak the lower was the resolution bandwidth with which it was measured. Thus, narrow and high noise peaks will appear the more washed out the further away they occur from the carrier. However, the total phase noise power in the spectrum will be accurately reproduced in the representation presented in fig. 5.8, as the spectrum analyzer performs a measurement of the integrated power per RBW over the specified span rather than a discrete sampling of the power distribution.

For clarity it shall be noted that the small structure seen in the range from 10^7 Hz to 10^9 Hz is negligible and that it is more due to the noise correction procedure than due to actual phase noise contributions, as in this range the beat signal and background noise are of the same order of magnitude (see fig. 5.7e)).

Based on the corresponding phase noise power spectral density $S^{\text{SSB}}(f)$ (in units of Hz) the value for η, i.e. the fraction of the carrier peak power compared to the power of the total spectrum power and the residual phase noise σ^2 can be extracted (cf. eq. (3.32)). The carrier power was determined as the integral power over the main peak in fig.5.7a) $S^{\text{DSB}}(f)$ between $f = -35$ Hz and $f = 35$ Hz while the power of the total phase noise spectrum was integrated over $\mathcal{L}^{\text{SSB}}(f)$ from $f = 0$ Hz and $f = 1$ GHz yielding

$$\eta_{\text{in}} = 97.34\% \qquad \text{and} \qquad \eta_{\text{out}} = 95.33\% \tag{5.3}$$

corresponding to a mean square phase noise of

$$\sigma_{\text{in}}^2 = 0.0270 \text{ rad}^2 \qquad \text{and} \qquad \sigma_{\text{out}}^2 = 0.0478 \text{ rad}^2 \tag{5.4}$$

for the in-loop and out-of-loop spectra, respectively.

The results obtained in this work can be assumed to be more accurate than those yielded earlier in [15], as the latter were conducted at coarser resolution bandwidths and the SSB spectrum was composed of only four individual measurements of the DSB beat signal. Apart from a consequently somewhat different measurement and evaluation procedure the results obtained in this work are in good agreement with the values obtained in [15]. For comparison, in [15] the residual phase error of the OPLL between 100 Hz and 7.5 MHz was found to be $\sigma^2 = 0.038$ rad^2 and the power fraction in the carrier was determined to be $\eta \approx 96\%$. The contribution of the 50 Hz noise peak was omitted in that evaluation [15] for an unclear reason. The measurements conducted in the present work, however, indicate that these mains frequency related noise peaks are not detection related, as for the out-of-loop measurement the power supply of the photodetector and Bias-Tee combination was a battery, but still a pronounced 50 Hz peak was visible just like for the in-loop measurement. The values of the fractions $\eta_{\text{in,out}}$ and the mean square phase noises $\sigma_{\text{in,out}}^2$ obtained from the present evaluation procedure contain all observed noise peaks.

As suspected, the in-loop measurement reveals slightly better performance of the OPLL than the more objective out-of-loop measurement, which is basically independent from the controllers' inherent noise. Notwithstanding, both measurements indicate a very decent phase-lock performance of the OPLL and the residual phase noise reaches values, which are significantly lower than those achieved in [177] and comparable to those in [131, 178, 179]. Thus, the probe and control laser are now again suitably prepared for coherent interactions, e.g. with atomic ensembles.

6. Proposal for a Narrow-band Diffraction Grating Filter

In the Rauschenbeutel nanofiber experiment the few photon probe signal is immersed in a fluorescence background of the nanofiber, caused by one of the Cs trap laser beams. As the fluorescence light is broadband compared to the EIT probe signal it can be assumed that narrow-band filtering of the signal will increase the signal to noise ratio.

At the beginning of this chapter a short resume of the latest fiber fluorescence characterization is given. Subsequently, a proposal for an experimental realization of a narrow-band filter system using a highly dispersive diffraction grating is presented, which was developed based on the theoretical investigations in the preceding theory chapter. The aim was to realize a rather simple setup which would bring about a filter window of maximally ± 0.1 nm around the probe center wavelength at 852.347 nm while reducing the actual probe signal as little as possible. Such a filter would lead to an improvement of the signal to noise ratio of at least one order. Originally it was planned to realize the diffraction grating filter proposed here, but due to massive delivery problems with the grating company this experiment could not be conducted. Thus, this chapter presents the elaborated setup plans including a list of the already ordered main components in order to enable a later realization of this setup.

6.1. Characterization of the fiber fluorescence

The spurious fluorescence light is induced in the fiber by the blue detuned trap beam at 780 nm with a power of 25 mW, which is co-propagating with the probe beam in the fiber. Recently, the spectral distribution of the fluorescence light was determined by the PhD students of the Rauschenbeutel nanofiber experiment. For that characterization two optical interference bandpass filters were inserted in the fluorescence beam exiting the nanofiber — as depicted in fig. 6.1 — before it was directed to an Avantes Avaspec ULS2048x16 $(600 - 1100$ nm) spectrometer (equipped with an AVA OSF 600-3 filter and an AVA slit 50). The first filter had a 40 nm transmission window around 850 nm to cut off the blue detuned trap beam at 780 nm and the second bandpass filter possessed a 10 nm transmission window around 850 nm. Both of these interference filters have a signal transmission of $\simeq 70\%$ and therefore reduce the overall probe signal by a factor of 2. Apart from that associated signal loss, the results of the spectrometric measurement in fig. 6.2 show that a significant fraction of fluorescence light nevertheless co-propagates with the signal.

The envelope of the spectral power distribution of the fiber fluorescence signal shown in
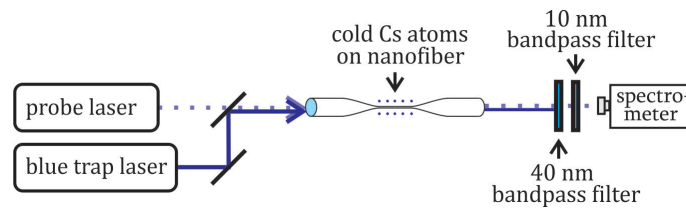

Figure 6.1.: Simple scheme of the experimental setup for the analysis of the spectral power distribution of the fiber fluorescence co-propagating with the few photon probe signal.
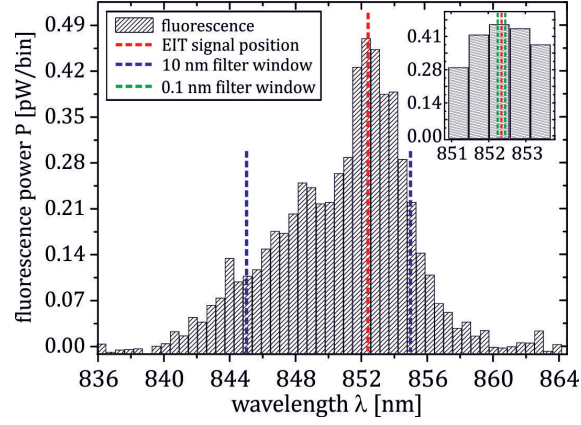
Figure 6.2.: Spectrum of the fluorescence light induced by the blue trap laser at 780 nm with a power of 25 mW measured after passing two interference filters with a transmission window of (850 ± 20) nm and (850 ± 5) nm (dashed blue line), respectively. The position of the probe beam (not measured here) is marked as dashed red line. The inset shows a magnified view of a narrow-band region around the probe laser line showing the desired filter window of 0.1 nm.

fig. 6.2 has a FWHM of approximately 10 nm centered around 852 nm due to the interference filters used for the spectral measurement. The data reveal that in this setting the probe and fluorescence signals are within a range of ± 5 nm around the probe's central frequency at 852.3 nm of the same order of magnitude, i.e. around 5 pW. However, the EIT probe signal is assumed to have a linewidth in the order of Hz or kHz and is therefore several orders of magnitude narrower than the broadband distributed fluorescence light. Thus, if the filter window could be narrowed by a factor of 10 or 100 a significantly improved signal to noise ratio would be achievable. But by means of interference filters this is not easily achievable. Interference filters with bandpass width in the nm range are very hard to get for the desired wavelengths or very expensive, if custom-made. Hence, other options for filtering the probe signal have to be considered.

As the EIT probe signal is expected to be linearly polarized it suggests itself to consider a polarization dependent separation of the signal from the fluorescence. Further analysis of the fiber fluorescence showed, however, that the fluorescence light is only weakly polarized. The data in fig. 6.3a) reveal this slight polarization dependence, which was probed by directing the fluorescence through a rotatable polarizer and measuring the transmitted power. The data
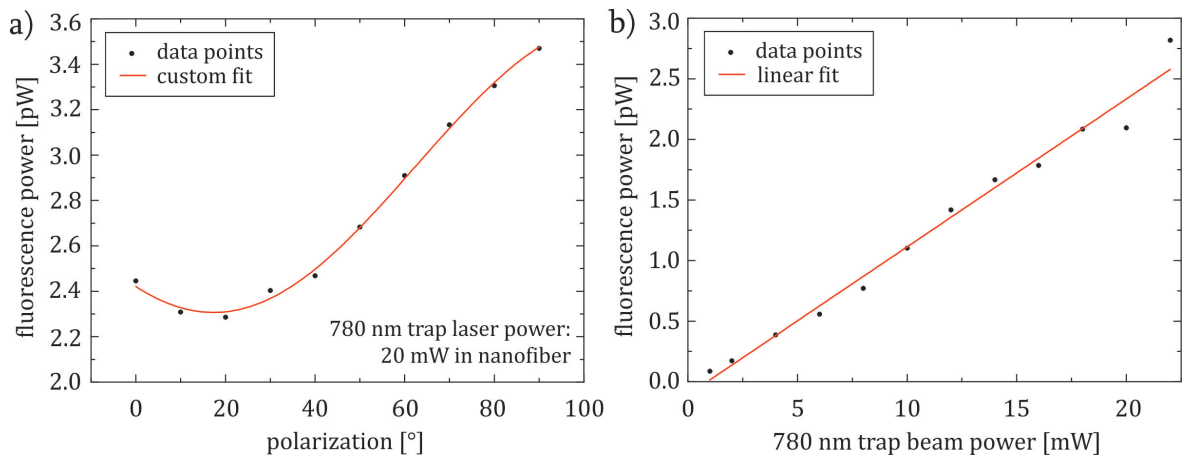

Figure 6.3.: The fluorescence signal is a) only slightly polarized and b) depends linearly on the blue detuned trap laser intensity.

can be fitted with a general superposition of two orthogonal linear polarization components $P_x(\theta) \propto E_{ox}^2 \cos^2 \theta$ and $P_y(\theta) \propto E_{oy}^2 \sin^2 \theta$ with the component's electric field amplitudes E_{ox} and E_{oy}. This gives the fluorescence power P_{fl} as a function of the polarization projection angles θ as

$$P_{\mathrm{fl}}(\theta) = (P_{oy} - P_{ox})\big(\sin(\theta - \theta_0)\big)^2 + P_{ox} \; . \tag{6.1}$$

A fit of the data by means of this fit function yields the powers of the corresponding polarization components $P_{ox} = (2.31 \pm 0.01)$ pW and $P_{oy} = (1.02 \pm 0.04)$ pW with the corresponding basis angle $\theta_0 = 17.3° \pm 0.8°$. The corresponding maximal and minimal values of the fluorescence power $P_{\mathrm{fl}}(\theta)$ found in the respective polarization planes θ are $\max\{P_{\mathrm{fl}}\} = P_{\mathrm{fl}}(107.3°) = (3.54 \pm 0.06)$ pW and $\min\{P_{\mathrm{fl}}\} = P_{\mathrm{fl}}(17.3°) = (2.31 \pm 0.01)$ pW. Thus, the best extinction ratio achievable with a polarization filter is

$$\frac{\max\{P_{\mathrm{fl}}\} - \min\{P_{\mathrm{fl}}\}}{\max\{P_{\mathrm{fl}}\} + \min\{P_{\mathrm{fl}}\}} \simeq 0.21 \; . \tag{6.2}$$

Therefore, the fluorescence cannot be sufficiently separated from the EIT probe signal using simple polarization filters.

Moreover, further investigations showed that the fluorescence power P_{fl} has a linear dependence on the power of the blue detuned trap laser at 780 nm $P_{780\mathrm{nm}}$ as can be extracted from fig. 6.3b). A linear regression reveals the relation

$$P_{\mathrm{fl}}(P_{780\mathrm{nm}}) = (122.0 \pm 5.1)P_{780 \; \mathrm{nm}} \cdot 10^{-12} - (107 \pm 67) \; \mathrm{fW} \; . \tag{6.3}$$

Hence, a slight alteration of the dipole trap laser powers will not lead to a significant improvement of the signal to noise ratio as well. Therefore, the implementation of a more advanced narrow-band filter system is indispensable.

6.2. Realizations of a simple narrow-band optical filter system

For the purpose of narrow-band filtering of optical signals there are several physical systems that may come to mind. A frequently implemented option is based on the narrow transmission peaks of optical Fabry-Pérot resonators [133, 134]. But it lies in the nature of the Airy transmission function of cavities that the more narrow-band the transmission peaks are the smaller the free spectral range (i.e. the frequency distance of those transmission peaks from each other) will become, if the cavity finesse cannot be increased by the same factor (e.g. due to fabrication limits or unreasonable costs). A suitable sequential combination of several optical resonators with different transmission linewidths and free spectral ranges can compensate for that drawback. In this case however, several control loops (e.g. a Pound-Drever-Hall lock) will be necessary for stabilizing the frequency positions of the cavities' resonances to the signal frequency [180]. Moreover, in order to achieve very narrow linewidths and to prevent the loss of a significant fraction of the signal power the cavity mirrors will need to feature very high reflectances. All together this will result in a rather pricey overall setup.

On the search for simpler, more cost-efficient and eventually less lossy filter options a diffraction grating could be considered. In that case, the wavelength dependence of the diffraction angle is for example exploited in grating mono and polychromators. For filter windows of sub-nm widths however the setup has to be highly specialized for the particular wavelength in order to achieve the high angular dispersion needed. In the following a proposal for such a highly dispersive diffraction grating setup is presented.
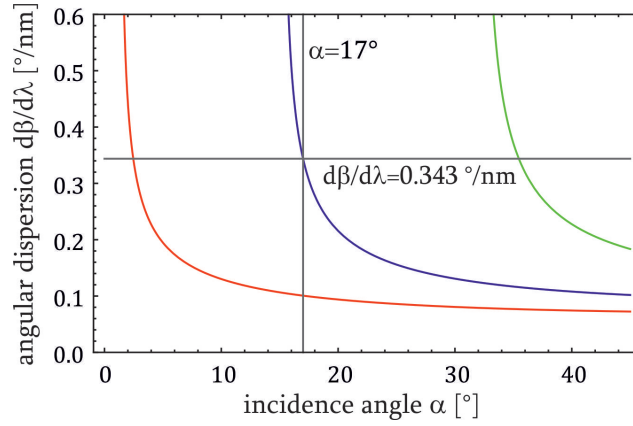
Figure 6.4.: Angular dispersion of the first diffraction order of a light ray of $\lambda = 852.3$ nm in dependance on the incidence angle α for gratings with different groove densities: with $G = 1200/\text{mm}$ (red curve), $G = 1480/\text{mm}$ (blue curve) and $G = 1800/\text{mm}$ (green curve) (for details see text).

6.2.1. Frequency filtering with a diffraction grating

For the application presented in sec. 5.1 a filter with a transmission window width in the sub-nm range is necessary. Filtering as narrow-band as this by means of a grating is very challenging. In sec. 4.1.2 of the theory chapter general expressions of the lower bounds for the incidence angle in eq. (4.11) and the upper bounds of the groove density in eq. (4.13) were derived. In order to obtain high angular dispersion it is of critical importance to choose a suitable combination of groove density and incidence angle lying as close as possible to the line of divergence defined as

$$\beta_m(G, \alpha) = \arcsin\left(m\lambda G - \sin\alpha\right) = \pm\frac{\pi}{2} \tag{6.4}$$

(cf. sec. 4.1.2). In satisfying this condition the grating operating point will be situated on the fast varying slope of the angular dispersion enabling maximal angular resolution. However, the operating point still needs to be chosen in the regime, where a stable mode of operation can be ensured.

In the experimental context a quantity of direct interest was found to be the variation of the angular dispersion $\mathrm{d}\beta/\mathrm{d}\lambda$ with respect to the incidence angle α as it essentially determines the stability of the setup. Inevitable mechanical perturbations (e.g. vibrations on the optical table) will lead to small variations of the incidence angle. Large values of the local gradient

$$\frac{\partial}{\partial\alpha}\left(\frac{\mathrm{d}\beta_m}{\mathrm{d}\lambda}\right)(\alpha, G) = -\frac{mG\cos\alpha\,(m\lambda G - \sin\alpha)}{(1 - (m\lambda G - \sin\alpha)^2)^{3/2}}\ , \tag{6.5}$$

i.e. the steepness of the flanks near the boundary line of eq. (6.4), will correspond to large deviations of the operation points. Gratings with higher values of G will possess higher angular dispersion than gratings with smaller G for equally stable configurations, i.e. where the values of $\frac{\partial}{\partial\alpha}(\frac{\mathrm{d}\beta_m}{\mathrm{d}\lambda})$ are the same.

As an illustration of this relationship in fig. 6.4 the angular dispersion around 852.3 nm is displayed in dependance on the incidence angle α for three different grating constants. These curves are basically cuts through the 3d angular dispersion plotted in the theory chapter in fig. 4.2. If for example for a grating with $G = 1480/\text{mm}$ (blue curve) an incidence angle of $\alpha = 17°$ can be supposed to possess a stable operation, then for a $G = 1200/\text{mm}$ grating (red curve) the slope $\frac{\partial}{\partial\alpha}(\frac{\mathrm{d}\beta_m}{\mathrm{d}\lambda})$ is significantly steeper at the point of similar angular dispersion, which comes along with a more instable performance. For a $G = 1800/\text{mm}$ grating (green
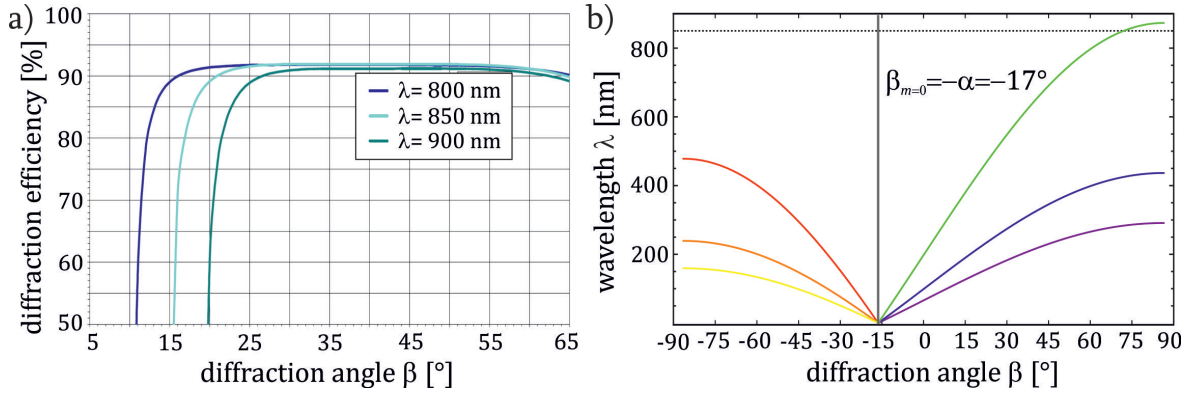
Figure 6.5.: a) Grating efficiency curves from a rigorous simulation by Horiba for the diffraction efficiency into the first order of rays at $\lambda = 800$ nm, $\lambda = 850$ nm and $\lambda = 900$ nm for the Horiba grating type 52428090 with 1480 grooves/mm (modified; original provided by Horiba)
b) Wavelengths of the positive and negative first three diffraction orders (grey: $m = 0$, red: $m = -1$, orange: $m = -2$, yellow: $m = -3$, red: $m = +1$, blue: $m = +2$, purple: $m = +3$), which occur at the possible diffraction angles β originating from a multichromatic incident beam at $\alpha = 17°$ diffracted at a grating with $G = 1480$/mm. The dashed grey line marks the wavelength of $\lambda = 852.347$ nm.

curve) on the other hand, the slope is less steep, and thus it would be possible to choose an incidence angle which is even closer to the respective minimum incidence angle. In this respect, combinations of groove density and incidence angle with higher G are to be preferred, as long as the condition of eq. (4.13) is satisfied.

6.2.2. Setup proposal and expected performance of a diffraction grating

Now it shall be investigated which combinations of groove density and incidence angle will be necessary and experimentally feasible in order to realize a narrow-band filter as needed for the nanofiber experiment. In order to get a theoretical estimate over the expected performance optimum of a real grating one has to account for the actual acceptance range of incidence angles of those gratings satisfying the condition of optimal groove density and incidence angle combinations mentioned above. As described in sec. 4.1.5 the blaze angle and the corresponding diffraction efficiency of a grating are normally optimized for one specific incidence angle and diffraction order. It turned out to be quite difficult to find gratings satisfying the need for suitably high groove densities between 1400 and 2200 grooves/mm (cf. fig. 4.2b)), while supporting the extreme incidence and diffraction angles needed for high angular dispersion. A thorough search through the product catalogues of various grating manufacturers reveals that the vast majority of gratings is optimized for the respective Littrow angle and the gratings suffer from quickly dropping efficiency even for slight deviations from the Littrow configuration.
The gold coated pulse compression gratings from Horiba are exceptional in this respect. These gratings support an extraordinarily wide incidence angle domain covering a range of several 10°. The grating type 52428090 with 1480 grooves/mm e.g. facilitates an incidence angle covering the very large range from $\simeq 15°$ to $\simeq 75°$ featuring an efficiency between 80% and 90% (see fig. 6.5a) for reference). However, the diffraction efficiency may drop for lower α as can be seen in fig. 6.5a). As the curve in fig. 6.5a) only shows results of a theoretical simulation by the grating manufacturer it still has to be verified experimentally as to how the grating efficiencies behave for the interesting incidence angle domain between 15° and 20°. The large dimensions of this grating ($40 \times 60 \times 10$ mm^3, ruled area: 36×56 mm^2) furthermore satisfy the precondition for a high number of illuminated grooves causing a desirably narrow
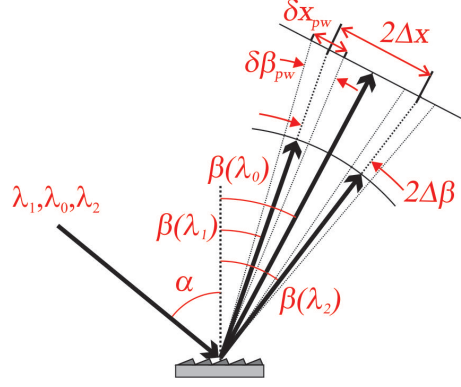
Figure 6.6.: Illustration of the spatial splitting of two different spectral components λ_1 and λ_2 subject to spectral filtering. Their angular and spatial pulse width $\delta\beta_{\mathrm{pw}}$ and δx_{pw} as well as their relative angular and spatial splitting $\Delta\beta$ and Δx are displayed, respectively.

angular linewidth of the spectral lines (see eq. (4.16) and eq. (4.33)).

One important point for filtering application with a grating is the overlapping of diffraction orders visualized in fig. 4.1c) of the theory chapter. The performed simulation in fig. 6.5b) to the contrary shows that for the proposed grating with $G = 1480/\mathrm{mm}$ and the incidence angle $\alpha = 17°$ in the expected diffraction angle region exclusively the desired first diffraction order can exist. Only for $\lambda < 450$ nm other diffraction orders can form. In that wavelength domain, however, no contribution is to be expected in the Rauschenbeutel nanofiber experiment.

For a grating with $G = 1480/\mathrm{mm}$, the theoretical lower bound incidence angle introduced in sec. 4.1.2 lies at $\alpha_{\min} = 15.158°$. If, for the sake of stability, an incidence angle of $\alpha = 17°$ is chosen one would yield an angular dispersion of approx. $\mathrm{d}\beta/\mathrm{d}\lambda \simeq 0.3438°/\mathrm{nm}$. With respect to a circular projection plane radially spanned around the diffraction grating with a radius of one meter (for illustration see fig. 6.6) the angular splitting of each pair of wavelength components at $\lambda_{1,2} = (852.347 \pm 0.05)$ nm and $\lambda_0 = 852.347$ nm would be expected as

$$\Delta\beta = \beta_{m=1}(\lambda_1) - \beta_{m=1}(\lambda_0) \simeq \beta_{m=1}(\lambda_0) - \beta_{m=1}(\lambda_2) \simeq 0.017° \tag{6.6}$$

corresponding to a spatial splitting of $\Delta x \simeq 0.30$ mm in a 1 m distance behind the diffraction grating. This value lies in the range, which seems to be experimentally feasible to access with a suitable aperture.

The finesse (cf. eq. (4.34)) achievable with the proposed Horiba grating type 52428090 under complete, homogeneous illumination is the number of grooves

$$\mathcal{F} = N = G \cdot w = 1480/\mathrm{mm} \cdot 56 \text{ mm} = 82880 \ . \tag{6.7}$$

In this case the angular pulse width of the monochromatic components λ_1, λ_0 and λ_2 in the first diffraction order are theoretically expected to be

$$\delta\beta_{\mathrm{pw}} = \frac{2\lambda}{Nd\cos\beta} \simeq 0.0018° \ . \tag{6.8}$$

At one meter distance from the diffraction grating this is equivalent to a spatial pulse width of $\delta x_{\mathrm{pw}} \simeq 32.1$ μm. The minimally resolvable angular splitting between two diffracted wavelengths λ_1 and λ_2 was given by the Rayleigh criterion in eq. (4.20) as one half of the angular pulse width $\delta\beta_{\mathrm{pw}}$. Thus, for two wavelengths at (852.347 ± 0.05) nm the resolution limit would be reached, when their relative angular splitting was $\Delta\beta_{\mathrm{Rayleigh}} \lesssim 0.0009°$ corresponding to a spatial splitting one meter behind the grating of $\Delta x_{\mathrm{Rayleigh}} \simeq 16.0$ μm. So, here the ratio

between the angular splitting $\Delta\beta$ of two wavelengths at λ_1 and λ_2 and the mean angular pulse width $\delta\beta_{\mathrm{pw}}$ of a monochromatic diffraction component at $\lambda \simeq 852$ nm is achieved to be

$$\frac{\Delta\beta}{\delta\beta_{\mathrm{pw}}} \simeq 9.3 \ . \tag{6.9}$$

This ratio allows for a clean filtering of the desired frequency component. Indeed, the result in eq. (6.9) exceeds the Rayleigh criterion by a factor of $\gtrsim 18$. But furthermore, leaking from neighboring spurious components into the filter window is prevented due to the high value of $\Delta\beta/\delta\beta_{\mathrm{pw}}$. Thus, the spatial filter aperture could even be narrowed further without loss of signal intensity.

6.2.3. Proposal for the optical setup around the diffraction grating

In order to find the best possible implementation of the previous theoretical considerations, it is important to focus on the critical parameters. These are first of all the effective number of illuminated grating grooves as the critical parameter determining both the finesse and resolving power of a diffraction grating. Thus, the beam forming optics before the grating needs to allow for an optimal illumination of the full ruled grating width. Furthermore, it is desirable to enhance the splitting of the freely propagating diffraction orders behind the grating and to design a setup that enables filtering on a compact area both by means of suitable optics. In the following a detailed proposal for a diffraction grating based narrow-band optical filter is presented.

The optical setup in fig. 6.7 shows a beam preparation optimized for an incidence angle of $\alpha = 17°$ and the resulting first order diffracted ray appearing at $\beta_{m=1} \simeq 75.72°$ for a beam of $\lambda = 852.347$ nm. In this case the difference angle is $\beta_{m=1} - \alpha \simeq 58.74°$. The first two lenses at position (1) and (2) are supposed to prepare the signal beam exiting the nanofiber with a beam waist of approx. 2 mm. They take care of the proper beam waist expansion and recollimation on the incident beam path for an optimal illumination of the full grating length. The optics proposed in tab. 6.1 represents a reasonable, cost-effective choice, as one of the main criteria was providing a setup of low price. However, a lens at position (2) with an even bigger diameter (e.g. of $\varnothing = 70$ mm) or even better a bigger, aspheric lens (providing abberation correction) would improve the grating illumination and thus the resulting angular resolution. For the latter the possible improvement is estimated to be approximately $10-20\%$ for a price increase of the lens by a factor of > 10.

After diffraction at the grating the desired first diffraction order has to be imaged onto the spatially filtering aperture, while other wavelength components outside of the desired filter window of (852.347 ± 0.05) nm are to be omitted. This can e.g. be accomplished by inserting a lens with a long focal length into the first order diffracted beam. This lens at position (4) needs to have a large diameter in order to focus the diffracted beam without optical distortions. The spatially filtering aperture can now be positioned at (5), which is the focal point of the lens at position (4). Here, an approximative calculation was performed on the basis of ray transfer matrix analysis [134, 133].[1] Fig. 6.8 shows a visualization of the first diffraction order marginal rays of three wavelength components $\lambda_1 = (852.347 - 0.05)$ nm (blue line), $\lambda_0 = 852.347$ nm (green line) and $\lambda_2 = (852.347 + 0.05)$ nm (red line) diffracted at the proposed grating. Each closely spaced pair of rays of the same color symbolizes the pulse width of that frequency components' marginal ray. It should be noted that the deviating

---

[1]It should be noted that Gaußian beam optics is not applicable here, as the diffraction orders are non-Gaußian modes due to a partial cut-off of the incident Gaußian beam mode at both the lens at position (2) and at the grating. This truncation at the grating is necessary for achieving a more homogeneous illumination of the full grating length in order to yield a higher effective number of illuminated grooves. A fully correct calculation would only be obtained by means of Fourier optics.
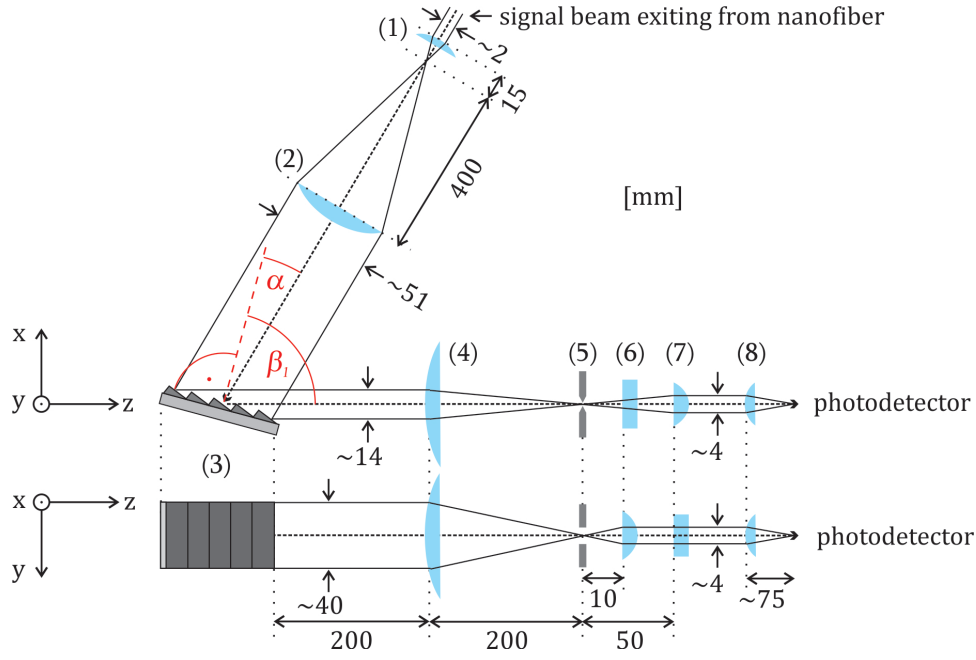
Figure 6.7.: Proposal for the beam forming optics around the diffraction grating (drawing not to scale). Details of the optical components are listed in tab. 6.1.

propagation lengths of the upper with respect to the lower marginal rays originating from both opposite ends of the grating in fig. 6.8 introduce a certain, small degree of asymmetry. The position of the grating (3), the lens (4), the spatially filtering slit (5) and the x-axis collimating cylindrical lens (6) are indicated in fig. 6.8.

According to this calculation at the focal point of lens (4), two wavelength components $\lambda_1 = (852.347 - 0.05)$ nm and $\lambda_2 = (852.347 + 0.05)$ nm will appear in a $\simeq \pm 3.44$ mm transversal distance to the desired $\lambda_0 = 852.347$ nm component. For all three wavelengths components λ_1, λ_0 and λ_2 the spatial pulse width at position (5) is $\delta x_{pw} \simeq 0.18$ mm. Thus, the proposed optical setup behind the grating possesses an enhanced ratio of

$$\frac{\Delta x}{\delta x_{\text{pw}}} \simeq 19 \ . \tag{6.10}$$

This is around a factor of 2 better than the result in eq. (6.9) without post-grating optics. In addition with this setup the absolute splitting $\Delta\beta$ is increased by a factor of 10, while the

Table 6.1.: Beam forming optical setup around the grating. All optical elements are from Thorlabs Inc. and were chosen to have an N-BK7 coating (pc=plano convex; pcc=plano convex cylindrical).

| Position	Object/Type/Properties	Purpose
(1) lens	LA1540-B pc: ø= 12.7 mm(= 1/2″), $f = 15$ mm	focussing
(2) lens	LA1725-B pc: ø= 50.8 mm (= 2″), $f = 400$ mm	recollimation
(3) grating	Horiba gold coated pulse compression grating, type 52428090, $G = 1480/$mm	diffraction
(4) lens	LA1353-B pc: ø= 75 mm, $f = 200$ mm	focussing
(5) slit	Newport compact slit type M-SV-0.5, micrometer precise adjustable width: $0 - 5$ mm	spatial filtering
(6) lens	LJ1878L1-B pcc: $f = 10$ mm, $H = 10$ mm, $L = 12$ mm	recollimation y
(7) lens	LJ1821L1-B pcc: $f = 50$ mm, $H = 20$ mm, $L = 22$ mm	recollimation x
(8) lens	LA1257-B pc: ø= 25 mm, $f = 75$ mm	focussing
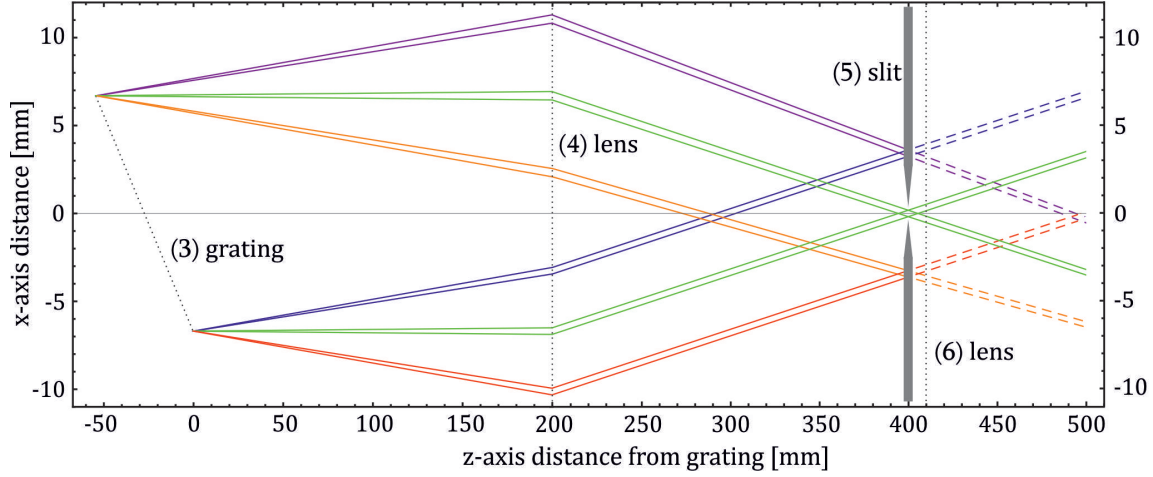
Figure 6.8.: Visualization of the enveloping rays of the first diffraction order of three wavelength components $\lambda_1 = (852.347 - 0.05)$ nm (blue line), $\lambda_0 = 852.347$ nm (green line) and $\lambda_2 = (852.347 + 0.05)$ nm (red line) diffracted at the grating as proposed.

needed propagation distance behind the grating is reduced by more than a factor of 2. This results in an experimentally more feasible and compact filter setup.

The spatially filtering aperture needs to fulfill certain requirements as fine-tunability on the μm scale. For this purpose a Newport type M-SV-0.5 compact slit with an adjustable slit width between $0 - 5$ mm was deemed appropriate. This slit has a fixed length of 12.7 mm and possesses two highly parallel blades, which can be driven symmetrically with a μm precise opto-mechanic positioner (type BM11.5 from Newport). The slit is supposed to be mounted on an equally μm precise translation stage from Thorlabs, type PT1/M for an accurate lateral positioning of the slit on the x-axis. Fig. 6.7 visualizes how the slit blades have to be precisely positioned at the focal point of the lens at (4) with a slit width of approximately 0.2 mm. The optimal slit width has to be determined experimentally. Clearly, spherical abberation effects of lens (4) are particularly unfavorable, while chromatic distortions are negligible for the considered wavelength range. In this respect, an aspheric lens at position (4) would possess cleaner filtering of the desired frequency component, though, at a significantly increased price.

Behind the aperture it is important to account for the elliptic transversal shape of the signal beam. The subsequent lenses at positions (6) and (7) are cylindrical in order to systematically reshape the elliptic diffracted beam for a selective recollimation of the signal beam on both the x- and y-axis. Finally, the lens at position (8) is spheric again and is used for refocussing the signal beam onto the avalanche photodiode (APD). For a fiber coupled APD the signal beam will have to be shaped more thoroughly. The parameters for this incoupling optics have to be chosen carefully with respect to the actual beam shape after the filtering process and thus no meaningful theoretical prediction can be given at this point.

It will be the main experimental challenge to find a stable setting with the lowest possible value of the incidence angle α. Clearly, in dependence on the actually implemented α setting $\beta_{m=1}$ will deviate and the positioning of the beam forming optics on the x-axis behind the grating will need to be adapted or probably even specific optical elements will need to be exchanged from the scenario calculated here. In this respect the dimensions given in fig. 6.7 must be regarded as guidelines. Ultimately, the setup — especially the part following after the diffraction process — has to be adapted in a more empirical fashion.

According to the calculations presented here, it is possible to realize an advanced filter window of (852.347 ± 0.050) nm with the proposed diffraction grating based setup and an incidence angle of $\alpha = 17°$. In this case the spectral filtering is improved by a factor of ~ 100 over

the spectral transmission widths $\delta\lambda \simeq 10$ nm achievable with interference filters. The signal loss due to the limited diffraction efficiency of the grating is expected to be $(75 \pm 10)\%$ according to the theoretical simulation by Horiba (cf. fig. 6.5a)). The resulting transmission window is therefore expected to significantly improve the signal to noise ratio of the EIT probe signal. By means of the fluorescence data displayed in fig. 6.2 the fluorescence power within a rectangular filter window of (852.347 ± 0.05) nm can be estimated to be $P_{\mathrm{fl}} \simeq 0.16$ pW (where the power suppression by a factor of 2 from the interference filters used for the measurement in fig. 6.2 is excluded). Thus, this diffraction grating filter is able to improve the signal to noise ratio by a factor of more than 100.

7. Experimental Investigation of a Homodyne Saturation Spectroscopy

Interferometers are highly sensitive devices. They are susceptible to virtually any kind of perturbation causing an alteration of the optical path length difference between the interfering beams. Path length difference variations on the order of a tenth of the optical wavelength leave conspicuous marks in the resulting interference pattern behind the interferometer. This high precision and sensitivity make interferometers prime candidates for detecting tiny phase retardation processes for such extreme cases as the measurement of quantum noise [162] or even the elusive footprint of gravitational waves [181].

In the theory chapter in sec. 4.2 the numerous advantages and features of heterodyne detection were examined. In the context of this thesis a first experimental attempt was made in order to exploit this superior interferometric detection method for a narrow-band filtering application as needed in the Rauschenbeutel nanofiber experiment. The realized test setup aiming at the examination of genuine homodyne detection features is described in the following.

7.1. Concept of the realized homodyne spectroscopy setup

For a first demonstration of the homodyne detection principle a straightforward experiment was realized. The role of the "atomic sample" imprinting a frequency distribution on the probing beam was taken over by a Cs cell saturation spectroscopy. The principle idea was to synthesize a conventional saturation spectroscopy signal by periodically scanning the frequency of an ECDL, in this case over the Cs D2 line transitions from $F = 3$ to $F' = 2$ up to $F = 3$ to $F' = 4$ (cf. fig. 5.2b)). This spectral information encoded on the weak spectroscopy probe beam as an amplitude modulation was to be measured via a homodyne detection setup. The test experiment presented here shall demonstrate the power of homodyne detection of such a time-resolved intensity profile.

The analogy with the setting in the Rauschenbeutel group's prospective EIT experiment lies in that in the latter the probe laser will be scanned over the EIT resonance as well by means of a double-pass AOM. While the fiber fluorescence noise is assumed to be distributed over a wide band, the EIT resonance is expected to have a width in the sub-kHz domain. In this test setup for comparison, the hyperfine lines will appear as saturation spectroscopic features of some MHz width. While this appears to be more than a factor of 10^3 wider than the anticipated EIT feature the scalability of the optical frequency resolution of this setup is defined by the ECDL/AOM scan amplitude only and not by the homodyne detection unit itself. The homodyne signal amplification is of universal nature and independent from the laser's frequency scan range or velocity.

Here, the resulting signal contains the frequency dependent saturated absorption profile $I(\nu)$ in a time-resolved fashion, i.e. $I(\nu(t))$. Thus, in order to resolve the hyperfine structure on the saturation spectrum the laser frequency scan rate f_{scan} and the limit frequency of the photodiode f_{crit} have to be well matched. If the frequency scan rate of the spectroscopy laser is e.g. chosen to be $\simeq 21$ Hz the hyperfine features of the Cs spectroscopy can only be resolved, if the limit frequency of the photodetector is in excess of a critical frequency f_{crit}
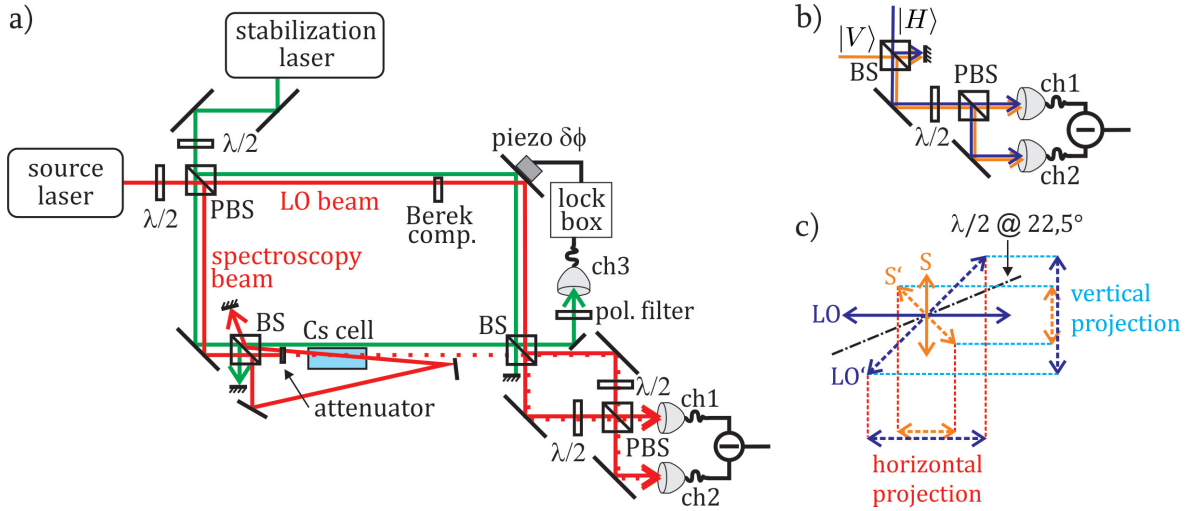
Figure 7.1.: a) Schematic, simplified representation of the implemented homodyne spectroscopy setup. b) Balancing for one of the BS outputs by means of c) a polarization projection measurement at a PBS (see text for details).

(in analogy to the considerations around eq. (4.52)). Here, the spectroscopy laser scans over the Cs spectrum with a scan interval of $\Delta f \simeq 1.5$ GHz within a scan time of $\Delta t \simeq 1/(2 \cdot 21)$ s. In order to resolve the hyperfine structure on the saturation spectrum a frequency resolution of $f_{\mathrm{res}} \lesssim 1$ MHz is needed. Thus, the critical frequency (=bandwidth) of the photodiodes needs to be

$$f_{\mathrm{crit}} \geq \frac{\Delta f}{\Delta t} \frac{1}{f_{\mathrm{res}}} \simeq 63 \text{ kHz} . \tag{7.1}$$

For this experimental demonstration a Thorlabs balanced photodetector PDB 210A with a bandwidth of $f_{\mathrm{crit}} \leq 1$ MHz was employed.

The conceptional setup of the conducted homodyne spectroscopy is displayed in fig. 7.1a). The source laser (drawn in red) feeds both beams needed for the homodyne detection principle: the source beam splits up into the spectroscopy beam and the local oscillator beam (LO) at the first polarizing beam splitter (PBS). Here, for the spectroscopy a branch of the ECDL was used, which was denoted as the 'control laser' in the previous sections. The $\lambda/2$ plate in front of this PBS enables a power adjustment between LO and spectroscopy beam. On a successive beam splitter (BS) the spectroscopy beam is split up into the pump and the probe beam of the saturation spectroscopy. The probe beam is attenuated by an appropriately chosen neutral density filter. On a second beam splitter the signal beam is superposed with the LO beam. At this stage behind this BS, however, interference between signal and LO beam does not occur, as the spectroscopy and LO beam are of orthogonal polarization by virtue of the first PBS.

Interference of spectroscopy and LO beam could be induced by inserting a $\lambda/2$ plate (at an angle of 45° to the horizontal) e.g. into the LO beam before this BS. But first, balanced homodyne detection needs a perfectly equalized power ratio between the two outputs of the combining BS to be detected by each of the two photodiodes of the balanced detector. Second, conventional 50/50 BS possess a mismatch of some percent ($\simeq 10\%$) between transmitted and reflected power (even laser line beam splitters have at least a mismatch of some percent $\simeq 3\%$) [182, 183]. Hence introducing the interference at this stage would be no suitable choice, if the canceling effect on classical noise of the balanced configuration shall be exploited.

7.2. Realization of the balanced detection

Instead an "equivalent circuit diagram" for the theoretically ideal 50/50 BS was elaborated in this thesis. The principle behind the optical balancing developed here shall be displayed in fig. 7.1b) and c). For the sake of simplicity first only one of the two BS outputs shall be considered as depicted in fig. 7.1b). Assuming all PBS's to transmit $|H\rangle$ and to reflect $|V\rangle$ polarization components in this case the signal beam will be of $|V\rangle$ and the LO beam of $|H\rangle$ polarization before and after their combination on the first BS in fig. 7.1b). These orthogonal polarization planes will be flipped according to the angle of the $\lambda/2$ plate axis. If the $\lambda/2$ plate is set to an angle of $\simeq 22.5°$ with respect to either the horizontal or vertical base both the signal and the LO polarization planes are turned by $\simeq 45°$. The subsequent PBS will then project these diagonal polarizations onto the two bases of the PBS: $|H\rangle$ and $|V\rangle$ (see visualization in fig. 7.1c)). Only by this projection the interference of signal and LO beam is first introduced in the setup. By detuning the $\lambda/2$ plate slightly from the angle of $22.5°$ the two outputs of the PBS feeding the two photodiodes of the balanced detector can be equalized in power, respectively. For the other output of the combining BS (which is blocked in fig. 7.1b)) the same principle applies: an equilibration of both photodiodes is possible over adjusting the $\lambda/2$ plate of this other arm. That way an optimal equalization of the powers incident on both photodiodes can be achieved. Even though the optical paths behind the combining BS might remind of a second Mach-Zehnder type interferometer, they are not: the polarization planes of the two beam fractions collected by either of the photodiodes are orthogonal again, i.e. the two beams at each of the two PBS outputs do not interfere, but only their powers are combined.

To the author's best knowledge, this optical balancing method has not been documented before. There exist other related methods exploiting two PBS (see e.g. [171]). That method, which uses only one PBS output suffers from signal losses due to imperfect transmission and reflection at the PBS of the respective polarization component and for practical reasons requires additional wave retarders in the individual arms of the interferometer. The latter is principally undesirable in terms of the additional phase noise introduced by such elements acting on just one of the interferometer branches. The method employed here on the contrary comes along without additional wave plates in the individual interferometer arms and detects the total signal power limited only by negligible absorption by the BS/PBS. Furthermore, here the one PBS is employed symmetrically such that an eventual transmittance and reflectance mismatch is automatically balanced.

The homodyne experiment is most importantly dependent on the fulfillment of two requirements: First, the spatial mode match, as well as the phase front curvatures and polarization planes of signal and local oscillator beam shall be as identical as possible in order to obtain a decent homodyne signal. For that reason signal and local oscillator beam were chosen to originate from the same source laser. The source beam is collimated with a telescope before entering the interferometer (not displayed in fig. 7.1a)). In addition on their way through the experiment, any beam shape deforming elements acting only on one of the beams need to be avoided. In this respect, the experiment revealed that it is e.g. of crucial importance to insert a Cs cell with high quality optical windows. The second important requirement for homodyning is the conformance of a constant phase relationship between signal and local oscillator beam at their mixing point. Here again, the fact that one source laser feeds both the signal and LO beam serves as a first important step toward relative phase stability. Inevitable mechanical and aerodynamical distortions of the interferometer, however, lead to a persistent fluctuation of the relative phase between signal and LO beam. These have to be compensated for by means of a control loop in order to realize a homodyne detection.
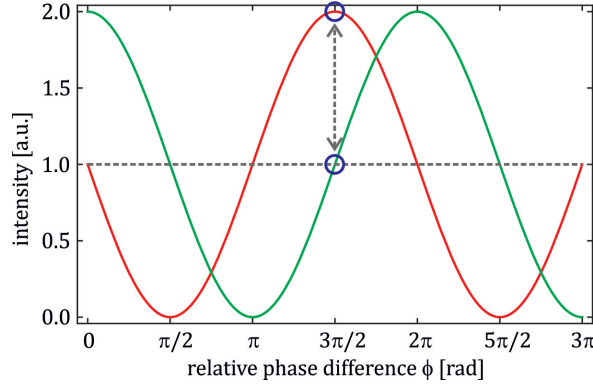
Figure 7.2.: The interferometer path length difference is stabilized such that the stabilization beam intensity is fixed at the intersection point between the stabilization beam fringes (green line) with its average intensity level (grey dotted curve). The spectroscopy beam receives an additional phase difference contribution of $\phi = \pi/2$ on the LO beam. Thus, the interference pattern of the spectroscopy and LO beam (red line) is stabilized to an extremal point.

7.3. Interferometer stabilization for an amplitude quadrature measurement

For the active stabilization of the optical path length difference between the two arms of the interferometer an error signal has to be generated and fed into lock electronics in order to produce an actuating value. This value needs to reset the relative phase difference between the two interferometer arms by actuating a phase shifting mirror mounted on a piezo actuator. In a Mach-Zehnder type interferometer the error signal is most suitably represented by the final interference fringe pattern in dependance on the relative phase between both optical branches. This fringe pattern is schematically displayed as the red curve in fig. 7.2. The steep slopes of the interference pattern at the relative phase difference points with odd multiples of $\pi/2$ are ideal for locking.

For the detection of the absorption spectrum an amplitude quadrature sensitive measurement has to be performed.[1] Thus a difficulty arises due to the fact that for the determination of the amplitude quadrature component of the signal the relative phase difference between signal and LO beam has to be even multiples of $\pi/2$. These points on the contrary are unsuitable lock point as they provide symmetric error signals with respect to the deviation direction. For that reason a more elaborate locking technique is necessary. A possible solution could be a Pound-Drever-Hall like locking procedure introducing a small modulation on the interference signal so that the derivative of the error function can be obtained. The derivative contains information about the sign of the slope on both sides of the error signals extremum and thus breaks its ambiguity. The need for an additional signal modulation and subsequent additional mixing electronics makes this technique rather demanding.

A way simpler option would exploit the perfect periodicity of the interference pattern. This stabilization option is depicted in fig. 7.1. For this technique an additional beam — the stabilization beam — is to be coupled into the interferometer at the second input port of the first PBS. Here, as stabilization beam a branch of the ECDL is employed, which was called the 'probe laser' in the previous chapters. This beam is employed for locking the interferometer on a steep fringe slope, while the signal fringe experiences a phase shift of odd multiples of $\pi/2$ relative to the stabilization beam. Thus, one of the beams has to pass through a wave retarder

---

[1]Principally, a phase quadrature sensitive measurement could be performed as well. However, this would measure the dispersive features of the respective hyperfine transitions. Those could be approximatively transformed into the absorption spectrum by means of the Kramers-Kronig relations [184].
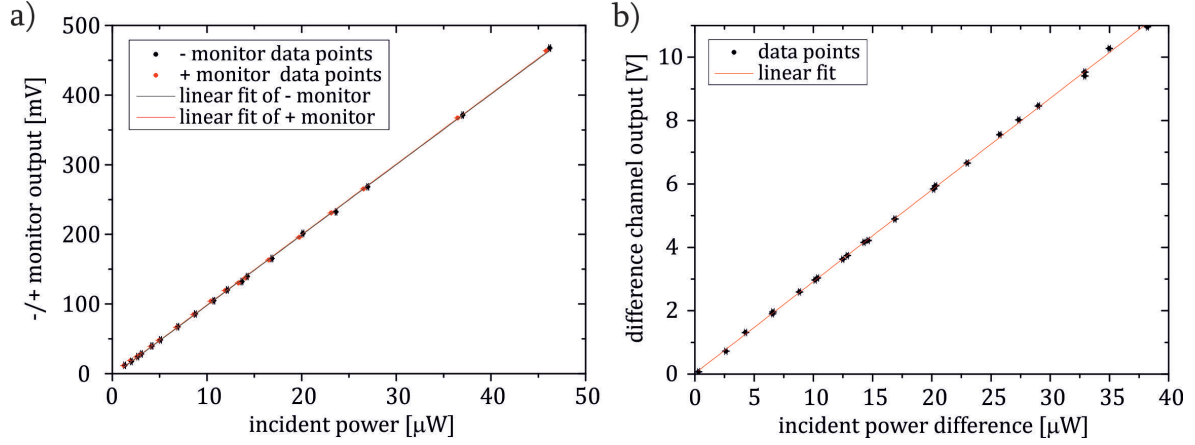
Figure 7.3.: Photodiode characteristics showing a) the - and + monitor signal outputs of the Thorlabs PDB 210A in dependance on the their respective incident powers and b) balanced difference signal output in dependance on the input power difference between the - and + photodiode.

on its propagation through the interferometer while the other does not. In this experiment the stabilization beam was chosen to propagate approximately 5 mm above the spectroscopy beam hitting all elements just like the latter, but bypassing the Cs cell on the signal arm and moving past a Berek compensator, which is placed in the LO arm of the spectroscopy beam. A Berek compensator consists of an uniaxial crystal cut with the extraordinary axis perpendicular to the plate. It can be seen as a continually tunable wave retarder plate. By means of appropriately tilting this birefringent optical device the LO beam can be retarded by $\pi/2$ with respect to the stabilization beam. Thus, when the stabilization beam is locked on the steep slope of the interference pattern the spectroscopy beam is automatically locked at its extremal points as needed for homodyne amplitude quadrature measurements.

For the detection of the stabilization beam's interference pattern the stabilization and the spectroscopy/LO beams have to be separated after the combining BS. Interference of the two orthogonal stabilization beams is introduced by letting them propagate through a polarization filter at 45° to the horizontal. The error signal is then fed into a standard laser lock box (home-made PI controller, following the "Lock Box No. 5" design from the University of Bonn) and the actuating output is taken as input of the piezo driver (Pickelmann SVR 500/1) operating the phase shifting piezo actuator (Pickelmann PSt 1000/16/15). For this system to lock it is of crucial importance that the combination of piezo actuator and piezo driver is able to actuate the piezo over a path length long enough to stay in lock over a reasonable time on the one hand and for large relative path length deviations on the order of several wavelengths on the other hand (e.g. due to acoustically excited oscillations of a mirror mount). This presumes basically a good match between the lock box actuating value voltage domain and the necessary piezo driver input voltage domain. On the other hand, the quality of the lock is determined by the frequency range of the lock system. A first limitation here is the resonance frequency of the piezo itself, which lies at 40 kHz. The mounted mirror reduces this limit to approximately 20 kHz due to the increased oscillating weight. The final limit is, however, set by the capacitively induced cutoff frequency of the combination of piezo actuator and piezo driver. In this case the piezo with a 150 nF capacity can be driven by the SVR 500/1 driver with some hundred Hz at best according to the piezo driver data sheet.

7.4. Characterization of the used balanced photodetector

For the noise canceling effect in balanced homodyning it is of crucial importance to have a detection system as symmetric as possible. Thus, this experiment aims at the characterization of the pair of balanced photodiodes used in all of the following experiments. It is a Thorlabs balanced amplified photodetector type PDB 210A. This detector provides three channels. The first two — called the '−monitor' and '+monitor' — deliver the preamplified single photodiode signals. The difference signal of the two (unamplified) photodiode outputs is passed through an ultra-low noise, high-speed transimpedance amplifier and can be tapped at the third output.

For the characterization of the photodiode's equalization the signal arm of the interferometer was blocked over the whole time and the LO beam was stepwise attenuated with various neutral density filters. The signal strength at the − and +monitor channels was measured in dependance on the actual optical power falling on each of the photodiodes. The results displayed in fig. 7.3a) show a very decent correspondence of the two photodiode's characteristics. Linear fits to the measured data give an input power to output voltage relation for the −monitor photodiode of

$$U_- = (10.11 \pm 0.03) \text{ mV}/\mu\text{W} \cdot P_- - (2.2 \pm 2.6) \text{ mV} \qquad (7.2)$$

and for the +monitor photodiode of

$$U_+ = (10.01 \pm 0.03) \text{ mV}/\mu\text{W} \cdot P_+ - (2.3 \pm 2.7) \text{ mV} . \qquad (7.3)$$

The negative offsets originate from both the photodiodes' and the oscilloscope's bias voltage. In a second attempt the balanced output of the Thorlabs PDB 210A was characterized. For this experiment one photodiode was completely blocked and the other photodiode was exposed to varying LO powers as before. The measured difference signals are displayed in fig. 7.3b). A linear fit reveals the relation

$$U_{\text{diff}} = (289.3 \pm 1.2) \text{ mV}/\mu\text{W} \cdot P_{\text{diff}} + (24 \pm 24) \text{ mV} \qquad (7.4)$$

between the difference channel voltage U_{diff} and the difference between the optical powers incident on both photodiodes $P_{\text{diff}} = P_+ - P_-$. Finally, a fixed amplification factor of $g \simeq 28.6$ between the single photodiode channels and the difference channel can be stated according to eq. (7.2), eq. (7.3) and eq. (7.4).

7.5. Characterization of the interferometer alignment

In the following the alignment of the interferometer and stabilization system is characterized. Generally, the fringe visibility

$$V = \frac{\max\{P(\Delta\phi)\} - \min\{P(\Delta\phi)\}}{\max\{P(\Delta\phi)\} + \min\{P(\Delta\phi)\}} \qquad (7.5)$$

of the interference pattern $P(\Delta\phi)$ of two coherently interfering waves with the maximum value $\max\{P(\Delta\phi)\}$ and the minimum value $\min\{P(\Delta\phi)\}$ is a measure for their mode overlap. For two interfering coherent beams of power P_1 and P_2 the visibility follows as

$$V = \frac{2\sqrt{P_1 P_2}}{P_1 + P_2} . \qquad (7.6)$$

Subsequently, for two beams of unequal power or reduced coherence the theoretically overall achievable visibility is suppressed.
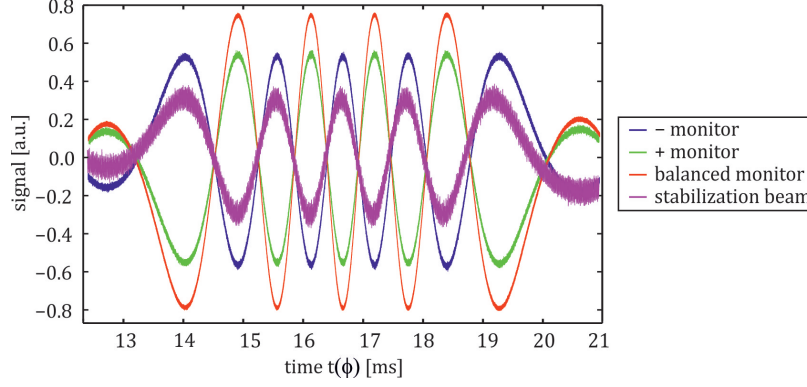
Figure 7.4.: Experimentally observed interference fringes for a controlled phase shift scan of a piezo mounted mirror. The y-axis was individually rescaled for each curve. The streching interference fringes over time is due to the nonlinear stressstrain curve of the piezo material, which occur around the maxima and minima of the piezo voltage. Displayed is the setting for the relative phase noise sensitive measurement described in sec. 7.6: the relative phase difference between −monitor and stabilization beam fringes is 0 and the fringes on the +monitor are phase shifted by π relative to the former.

In order to attain optimal overlap between the signal and LO beam the interferometer was adjusted toward optimal interference fringe contrast of signal and LO beam. This is most suitably performed while the LO phase-shifting piezo mirror was in the scan mode (see e.g. fig. 7.4). With a signal power of $P_s = 0.54 \ \mu\text{W}$ and a LO power of $P_l = 32.04 \ \mu\text{W}$ the theoretically achievable visibility is 0.26. In the experiment a visibility of 0.2 could be reached between signal and LO. This lower value can be assigned to a residual imperfection of the mode overlap and a reduction of coherence due to fluctuations in the relative phase relation between signal and LO beam. For the stabilization beam interference (with $P_1 \simeq P_2$) a visibility of 0.6 was obtained, which was mainly limited by restricted adjusting possibilities: for the alignment of the stabilization beam only two incoupling mirrors directly before entering the interferometer were available. After iterative optimization of the source laser beam and the stabilization beam to the interferometer, finally the interferometer had to be optimized for the signal and the LO beam in order to obtain high signal detection efficiency.

7.6. Inspection of the interferometer relative phase stabilization

Now the performance of the implemented stabilization system is to be investigated. Here, all measurements aiming at the acquisition of phase noise were recorded as time-dependent DC signals on an Agilent InfiniiVision type MSO6104A digital oscilloscope as for this, but especially for the subsequent interferometer stabilization measurements low frequencies from DC up to the kHz range were of particular interest. Moreover all subsequent measurements should be performed at all four photodiode outputs simultaneously. For both reasons, a storage oscilloscope was more appropriate for data acquisition than the spectrum analyzers, which were readily available. The time-dependent photodiode signals were postprocessed to obtain the desired phase noise power spectral densities via an FFT routine, which was implemented in MATLAB. Generally, due to the finite measuring time a periodic signal may be sampled over a noninteger number of cycles giving rise to a discontinuity in the time-resolved signal. These discontinuities lead to the appearance of spurious contributions to the FFT spectrum at frequencies higher than the respective Nyquist frequency. The resulting partial spectral redistribution of the signal power is called spectral leakage and causes the FFT spectrum to appear smeared out [185]. In order to compensate for such artifacts a
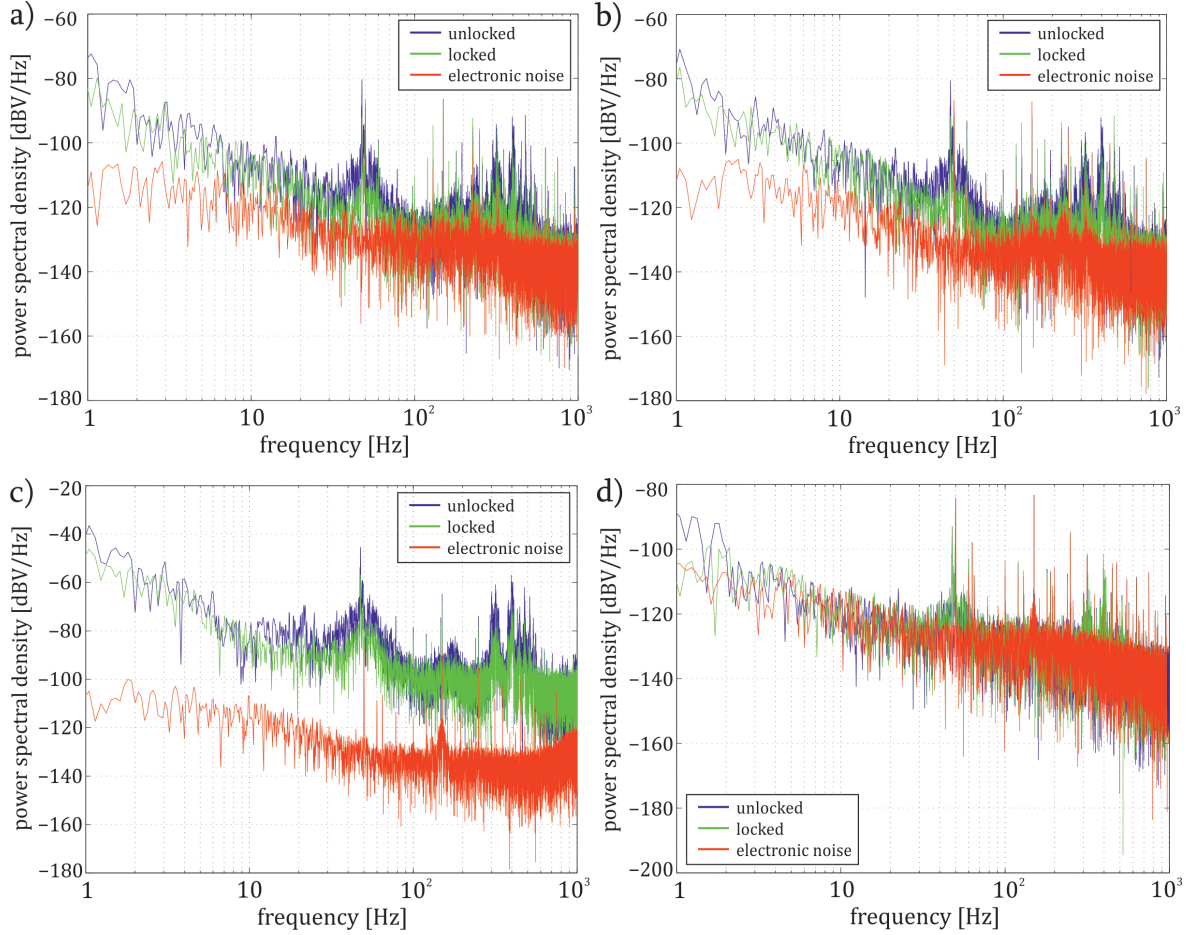
Figure 7.5.: Phase noise spectra of all photodiode channels for each the unlocked (blue) and the locked (green) interferometer. For comparison the red curve shows the electronic noise on each output while all photodiodes were blocked. The spectra display a) the −monitor noise, b) the +monitor noise, c) the balanced monitor noise and the d) stabilization photodiode noise. (For this phase noise measurement the −monitor fringe pattern and stabilization beam interference pattern are locked in phase, the +monitor fringes are π out of phase with respect to the former.)

Hanning type windowed FFT routine [186, 187] was implemented.

In order to determine the phase noise of the interferometer for this measurement the Berek compensator was readjusted such that the induced phase shift of the fringe pattern with respect to the stabilization beam fringes on the −monitor was 0 and on the +monitor π (see fig. 7.4). That way, all photodiodes measure the noise of the phase quadrature component. The signals of the unlocked interferometer were measured while the phase shifting mirror piezo voltage was set and fixed at a value were the relative phase $\phi_{sl}(t = 0) \simeq 0$ at the start time of the measurement. Over the measurement interval of 10 s the phase ϕ_{sl} was observed to slightly drift around $\phi_{sl}(t = 0) \simeq 0$ as expected.

Fig. 7.5 shows the resulting phase noise power spectral densities of all four photodiode channels, both for the relative phase stabilized (green curves) and the unlocked (blue curves) interferometer. The power spectral densities are displayed in dBV (i.e. decibel with respect to 1 V). The data were obtained over the FFT routine performed on the corresponding time-dependent photodiode signals for a record time of 10 s with an oscilloscope sampling rate of $f = 50 \cdot 10^3$ Hz. To better assess the measured data shown in fig. 7.5 the electronic noise on all channels for the optically blocked photodiodes (red curves) are displayed for reference.

The phase noise data in fig. 7.5 reveal that a significant phase noise suppression effect of the active interferometer stabilization is restricted to the low frequency region from DC up to some 10^2 Hz as expected. This suppression is on the order of $\simeq 5$ dB to $\simeq 10$ dB on all monitor channels of the balanced photodiode. The impact of the stabilization is most prominently observed on the balanced photodiode output in fig. 7.5c). It is observed that the 50 Hz mains frequency noise peak found on the noise curve has the same strength and frequency position in the locked and unlocked phase noise curves in both fig. 7.5a) and b). On the locked and unlocked phase noise curves on all photodiode channels, however, an additional significantly wider and stronger noise peak is found at $\simeq 47.59$ Hz. This is probably due to leaking of the mains frequency over the lock box power supply into the control circuit and some unknown mechanism leading to a slight frequency shift and broadening of that feature. Another possibility is that this near mains frequency noise originates from the piezo driver. This noise peak is suppressed by $\simeq 13$ dB in the locked interferometer case with respect to the unlocked case, but still lies about 40 dB above the electronic noise floor of $\simeq 130$ dBV. In the frequency range between 150 and 600 Hz undifferentiated noise peaks occur most probably due to mechanical vibrations on the table. As can be seen in fig. 7.5a), b) and c) in this frequency region only a slight noise improvement of some dB is achieved in the stabilized interferometer case.

The rather restrained noise suppression of the implemented stabilization system is certainly due to the stabilization photodiode (Osram SFH2400 standard photodiode), which has a low saturation intensity, while possessing a relatively high electronic noise floor. Its noise characteristic is displayed in fig. 7.5d). It can be seen, that the phase noise of the stabilized interferometer is already suppressed by the control loop to the level of the electronic noise on the stabilization photodiode. However, on all channels of the balanced pair of photodiodes in fig. 7.5a), b) and c) the electronic noise floor is distinct from the phase noise distributions and about $5-10$ dB lower on the $-$ and $+$monitor and $10-30$ dB lower on the balanced output than the respective phase noise distributions in the displayed spectral region. As the optical power of the stabilization beam could not be increased further due to the photodiodes saturation limit. In an enhanced setup this photodiode needs to be exchanged with a photodiode of either a significantly higher saturation level or significantly lower noise.

7.7. Investigations on the spectral fidelity and optical signal amplification

In this experiment the optical amplification of the saturation spectroscopy signal for homodyning at varying LO beam powers was investigated. Furthermore, the applicability of this method for spectroscopic investigations was examined. Here, a saturation spectroscopy of the Cs $6^2\ S_{1/2}\ F = 3 \rightarrow 6^2\ P_{3/2}\ F' = 2, 3, 4$ transitions was observed. For the demonstration of the potential of optical homodyne amplification the saturation spectroscopy signal beam was chosen of such low power ($P_s = 0.54\ \mu$W) that the directly detected signal (i.e. without homodyning with the LO beam) was in the order of the electronic noise in the difference signal output of the balanced photodiodes, when observed on the oscilloscope. As fig. 7.6 shows by subsequently increasing the power of the LO beam the saturation spectroscopy signal could be amplified to a meaningful level without any significant noise contributions. The power of the LO beam was varied by means of neutral density filters. This made it necessary to relock the interferometer stabilization and readjust the Berek compensator for every LO power setting. It is mainly for this reason that the individual curves in fig. 7.6 were subject to an arbitrary time offset, which had to be corrected in order to obtain comparability. Thus, only the relative distances between the hyperfine lines should be considered to be meaningful.
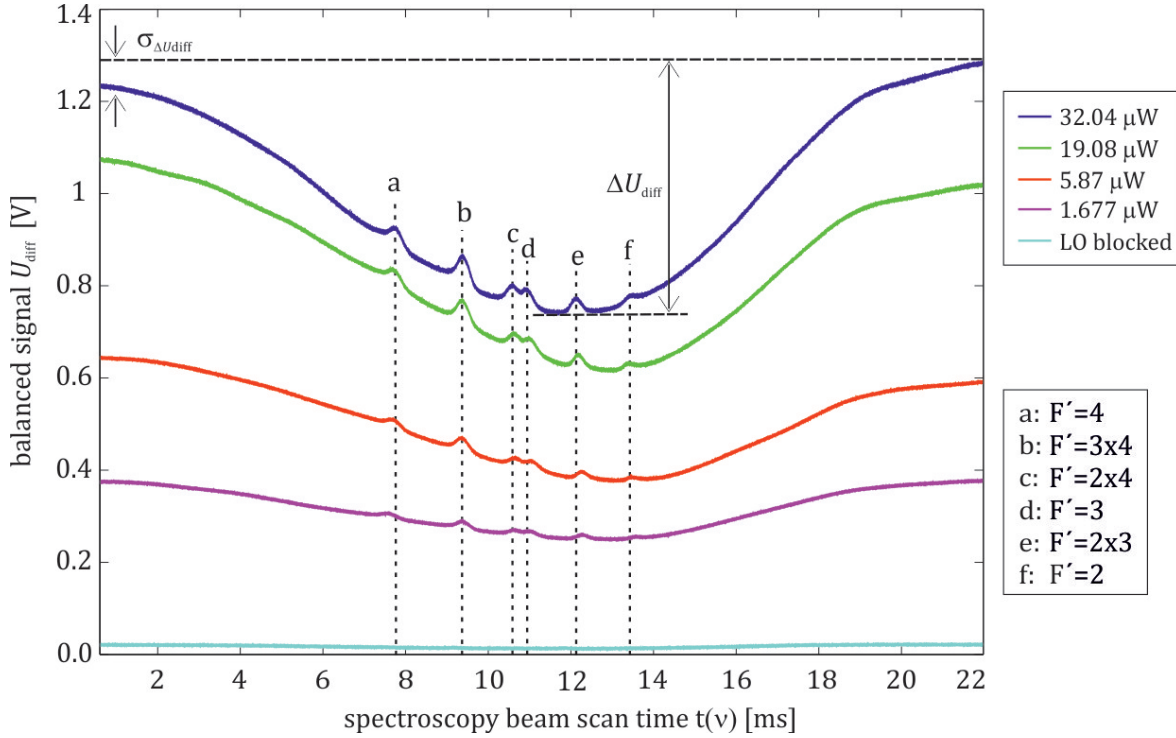
Figure 7.6.: Saturation spectra of the Cs $6^2 \, S_{1/2} \, F = 3 \to 6^2 \, P_{3/2} \, F' = 2, 3, 4$ transitions measured at the balanced photodiode output as a function of the spectroscopy beam frequency scan time $t(\omega)$ for varying LO powers P_l between 0 and $32.04 \, \mu$W. A linear dependence between the scan time $t = t(\nu)$ and the laser frequency ν can be assumed for the displayed range in approximation.

7.7.1. Spectral fidelity

If homodyne detection is to be employed as a spectroscopic measurement tool it is important to investigate its fidelity. Distortions of the spectrum could degrade the explanatory power of homodyning for spectroscopic applications. At a closer look in fig. 7.6 a certain variation of the relative distance between the hyperfine peaks can be observed. In fig. 7.7a) the relative distances between the hyperfine peaks Δt are plotted as a function of the LO power P_l. Fits to a constant value of the relative scan time distances $\Delta t(\Delta \nu)$ of each neighboring pair of resonances show that the relative peak position variations lie within the determined error range. The resulting values for the average relative hyperfine peak distances Δt are displayed in tab. 7.1 together with their total error, whose main contribution arises from the noise on the saturation signal. For comparison tab. 7.1 also lists the theoretically expected optical frequency differences, which were calculated based on the transition values given in [173]. By

Table 7.1.: Fitted values for the average relative hyperfine peak distances Δt and the theoretical optical frequency differences $\Delta \nu$ between the corresponding hyperfine features.

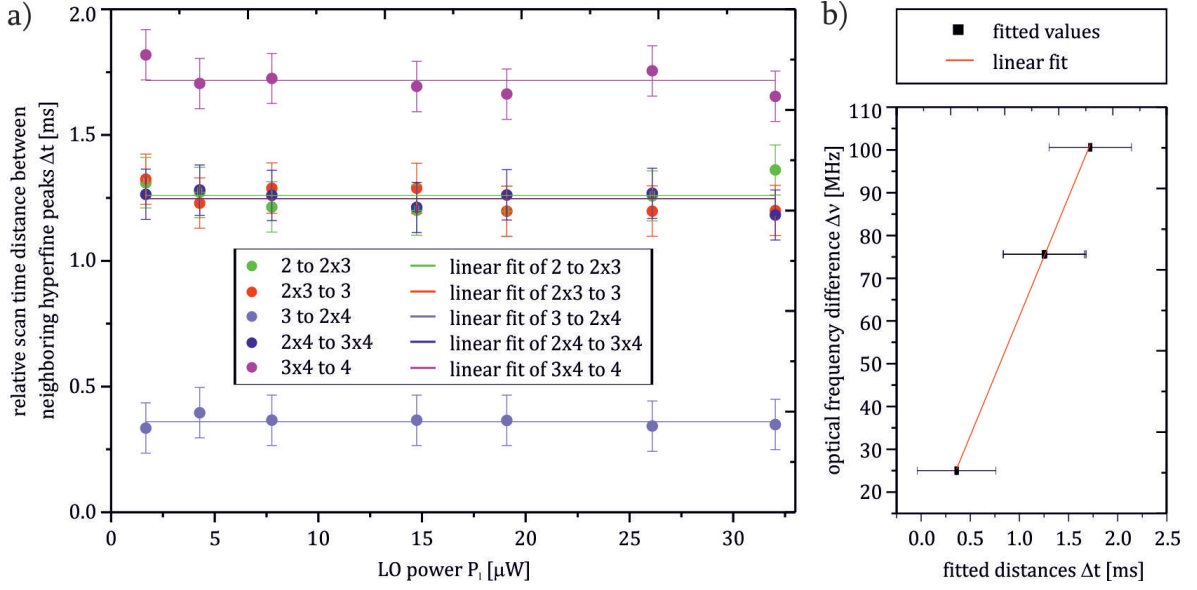| corresponding resonances $6^2 \, S_{1/2} \, F = 3 \to 6^2 \, P_{3/2} \, F' = ...$	fitted values $\Delta t(\Delta \nu)$ [ms]	frequency difference $\Delta \nu$ [MHz]
$2 \leftrightarrow 2 \times 3$	1.26 ± 0.12	75.606
$2 \times 3 \leftrightarrow 3$	1.25 ± 0.12	75.606
$3 \leftrightarrow 2 \times 4$	0.36 ± 0.11	25.015
$2 \times 4 \leftrightarrow 3 \times 4$	1.25 ± 0.11	75.606
$3 \times 4 \leftrightarrow 4$	1.72 ± 0.12	100.621

Figure 7.7.: a) Relative spectroscopy beam scan time distances of the hyperfine peaks Δt on the observed saturation spectra as a function of the LO power P_l. The drawn lines refer to linear fits with a vanishing slope, respectively.
b) Plot for the determination of the functional dependence of the optical difference frequency $\Delta\nu$ on the hyperfine peak scan time distances Δt. The fit shows a linear regression.

means of a linear fit (see fig. 7.7b)) the correspondence between the spectroscopy laser scan time difference Δt and its corresponding optical frequency difference $\Delta\nu$ is determined to be

$$\Delta\nu(t) = (55.83 \pm 0.63) \text{ MHz/ms} \cdot \Delta t + (5.28 \pm 6.5) \text{ MHz} . \tag{7.7}$$

The standard deviation of the relative peak distances extracted from the linear fits in fig. 7.7a) are around $\sigma_t = 0.02$ ms each (mainly due to the reading accuracy) and thus give rise to a relative frequency precision of $\sigma_\nu \simeq 6.5$ MHz of the spectroscopic method conducted here.

7.7.2. Low-noise optical signal amplification

In fig. 7.8 the height ΔU_{diff} of the full Doppler-broadened spectroscopy dip (see fig. 7.6) was measured for varying LO powers between 0 and 32.04 μW. The latter value marks the saturation limit of the balanced photodiode. On the oscilloscope a significant time-dependent y-axis distortion of the spectra was observed, which can be described as time-dependent compression of the spectrum height fluctuating on a scale of a few seconds. These fluctuations were identified to be due to deviations of the relative phase between the two interferometer branches (i.e. between signal and LO beam) from the desired value of multiples of π (odd multiples on one photodiode and even multiples on the other, respectively). The reasonably dimensioned reading accuracy errors $\sigma_{\Delta U\text{diff}}$ displayed as error bars of the determined heights ΔU_{diff} in fig. 7.8 account for these relatively large fluctuations.
Theoretically it is expected that the balanced photodiode current i_{diff} scales proportional to the square root of the local oscillator power P_l (cf. eq. (4.45)). Here, a realistic model accounting for imperfect balancing was employed for fitting the data. It includes a possible small mismatch between the signal and LO contributions on the –monitor P_s^- and P_l^- and the +monitor P_s^+ and P_l^+ represented by the small power differences $\delta P_s = P_s^+ - P_s^-$ and $\delta P_l = P_l^+ - P_l^-$ on the – and +monitor photodiodes (with $P_s^- + P_s^- = P_s$ and $P_l^- + P_l^- = P_l$, respectively). The general balanced photodiode current then follows as

$$\Delta i_{\text{diff}} \propto P_s^+ + P_l^+ + 2\sqrt{P_s^+ P_l^+}\cos(\phi_{sl}) - \left(P_s^- + P_l^- + 2\sqrt{P_s^- P_l^-}\cos(\phi_{sl} + \pi)\right) . \tag{7.8}$$
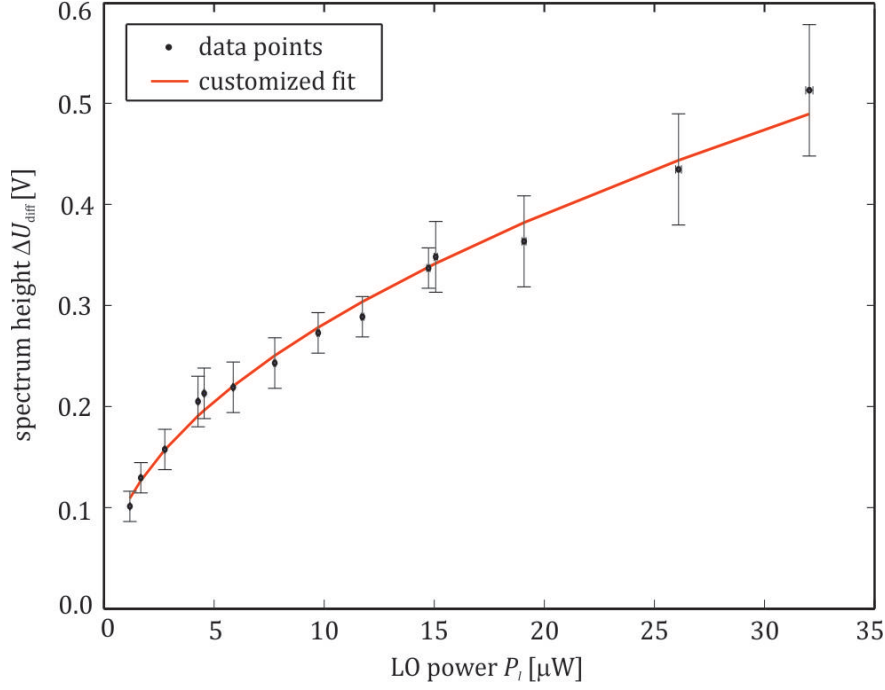
Figure 7.8.: Full height of the Doppler-broadened spectroscopy dip as a function of the LO beam power.

In the case of the amplitude quadrature sensitive measurement conducted here the relative phase between signal and LO beam is $\phi_{sl} = n\pi$ with $n \in \mathbb{Z}$. Without loss of generality here the relative phase can be set to $\phi_{sl} = 0$, such that the balanced photodiode current is

$$\Delta i_{\mathrm{diff}} \quad \propto \quad \delta P_s + \delta P_l + 2\left(\sqrt{P_s^+ P_l^+} + \sqrt{(P_s^+ - \delta P_s)(P_l^+ - \delta P_l)} \right) . \tag{7.9}$$

In a reasonable first order approximation the term $\delta P_s \delta P_l$ is negligible, as the power differences δP_s and δP_l are both very small. Subsequently, eq. (7.9) can be rewritten as

$$\Delta i_{\mathrm{diff}} \quad \propto \quad \delta P_s + \delta P_l \; + 2\sqrt{P_s^+ P_l^+} \left(1 + \sqrt{1 - \frac{\delta P_s}{P_s^+} - \frac{\delta P_l}{P_l^+}} \right) . \tag{7.10}$$

Both δP_s and δP_l can be assumed to scale linearly with the total power of the corresponding beam, thus

$$\delta P_s \simeq c_s P_s^+ \qquad \text{and} \qquad \delta P_l \simeq c_l P_l^+ \tag{7.11}$$

with the constant scaling factors c_s and c_l. With the photodiode conversion factor $\xi = (289.3 \pm 1.2)\,\mathrm{mV/\mu W}$ and the photodiode offset $\zeta = (24 \pm 24)\,\mathrm{mV}$ from eq. (7.4) the balanced photodiode voltage results as

$$U_{\mathrm{diff}}(P_s, P_l) = \left(c_s P_s^+ + c_l P_l^+ \; + 2\sqrt{P_s^+ P_l^+} \left(1 + \sqrt{1 - c_s - c_l} \right) \right) \cdot \xi + \zeta . \tag{7.12}$$

But here, instead of the absolute value of P_s^+ the saturation spectrum power heights $\Delta P_s^+ = P_s^+ - P_{s\,\mathrm{min}}$ corresponding to the balanced photodiode voltage difference $\Delta U_{\mathrm{diff}} = U_{\mathrm{max}} - U_{\mathrm{min}}$ (see fig. 7.6) are to be fitted, where the P_s^+ and U_{max} refer to the highest point of the saturation spectrum and $P_{s\,\mathrm{min}}$ and U_{min} to the lowest point of the Doppler broadened saturation dip. Now the fit function for the saturation spectrum heights ΔU_{diff} as a function of the LO power reads

$$\Delta U_{\mathrm{diff}}(P_l) = \xi \cdot \left(c_s \Delta P_s^+ + 2\left(\sqrt{P_s^+ P_l^+} - \sqrt{(P_s^+ - \Delta P_s^+)P_l^+} \right) \left(1 + \sqrt{1 - c_s - c_l} \right) \right) . \tag{7.13}$$

Based on this customized function the obtained fit displayed in fig. 7.8 (red curve) shows a perfect agreement of the measured data with the theoretically assumed behavior within the error bars. By means of fitting the data the determination of δP_s and δP_l was found not to be decisive, as for various parameters start values between 10^{-3} and 1 for both c_s and c_l the fit was found to be equally good in terms of the method of least squares [156]. As fitted parameters with estimated errors follow the small imbalance factors $c_s = 0.4 \pm 0.5$ and $c_l = 0.5 \pm 0.5$ and the saturation spectrum power height $\Delta P_s^+ = (15 \pm 5)$ nW.

In summary, this experiment demonstrated the power of optical homodyne amplification for the detection of atomic transition features at sub-μW signal light levels and proves the theoretically expected scaling behavior with the LO beam power. As this optical amplification is of low noise it enables very high power resolution of low light signals. In this rather simple setup, the hyperfine structure features of less than 8 nW height could be clearly resolved. The saturation limit of the balanced photodiode is the only bound in this respect. Hence, homodyne detection can be regarded as a promising technique for low-noise optical signal amplification enabling narrow-band, post-detection electronic filtering, which can fruitfully be exploited for the nanofiber experiment.

8. Outlook

In order to trigger further development of the presented setups some opportunities for subsequent improvements of the work presented here shall be discussed in this chapter.

8.1. Possible improvements of the probe/control laser preparation and OPLL setup

A recommendable improvement of the optical setup of the in-loop beat signal detection concerns the fast ET-4000 GaAs PIN detector from EOT. This model has a focussing plastic lens built into the entrance aperture in the chassis. Due to the fact that this lens has no suitable anti-reflection coating, a small but significant part of the probe beam manages to propagate backwards through the setup and into the polarization spectroscopy of the control laser. Here, it leads to additional hyperfine features associated with the probe saturation spectroscopy features $F = 4 \rightarrow F' = 3, 3 \times 4, 4, 3 \times 5, 4 \times 5, 5$, which may disturb the frequency lock of the control laser. The need for a perfect overlap of the probe and control laser on the fast photodiode does not allow for a slight misalignment and thus this backwards propagating probe beam cannot be masked out by means of apertures. The stability of the control laser's frequency lock could thus be improved by carefully quarrying out the plastic lens or providing the fast photodiode with a new, self-made housing and an additional anti-reflection coated focussing lens. This would incidentally facilitate the not so easy adjustment of the fast photodiode and may hence improve the detected beat signal strength.

8.2. Other possible improvements

Recently it has been considered to modify the experimental setup of the nanofiber experiment and change the EIT resonance to transitions on the Cs D_1 line at around $\lambda = 894.593$ nm. At the moment it is unknown as to how the fiber fluorescence characteristics are modified around that region. Nonetheless, in the following theoretically determined values for the necessary angles and estimations of the possible performance of the proposed diffraction grating with $G = 1480$/mm working on the D_1 line are given.

Filter grating setting for the D_1 line at $\lambda_0 = 894.593$ nm:

- theoretical lower bound incidence angle: $\alpha_{\min} = 18.905°$

- proposed incidence angle: $\alpha = 21°$

- first order diffraction angle for λ_0: $\beta_{m=1} \simeq 74.93°$

- difference angle: $\beta_{m=1} - \alpha \simeq 53.95°$

- angular dispersion at $\beta_{m=1}(\lambda_0)$: $\mathrm{d}\beta/\mathrm{d}\lambda \simeq 0.3262°$/nm

- angular splitting between $\lambda_{1,2} = (852.347 \pm 0.05)$ nm and $\lambda_0 = 852.347$ nm:
  $\Delta\beta = \beta_{m=1}(\lambda_1) - \beta_{m=1}(\lambda_0) \simeq \beta_{m=1}(\lambda_0) - \beta_{m=1}(\lambda_2) \simeq 0.016°$

- angular pulse width of component λ_0: $\delta\beta_{\text{pw}} \simeq 0.0020°$

- ratio between the angular splitting $\Delta\beta$ and the mean angular pulse width $\delta\beta_{\text{pw}}$ of diffraction component at λ_0:
  $\Delta\beta/\delta\beta_{\text{pw}} \simeq 8.0$

These values are very similar to those obtained for $\lambda_0 = 852.347$ nm. Therefore, it is reasonable to expect that the proposed grating filter setup can be adapted to a setting probing the D_1 line with reasonable effort as well.

Bibliography

[1] J. I. Cirac, P. Zoller, H. J. Kimble, and H. Mabuchi: *Quantum state transfer and entanglement distribution among distant nodes in a quantum network.* Phys. Rev. Lett., 78(16):3221–3224, 1997.

[2] L. M. Duan, M.D. Lukin, J. I. Cirac, and P. Zoller: *Long-distance quantum communication with atomic ensembles and linear optics.* Nature, 414:413–418, 2001.

[3] Pieter Kok, W. J. Munro, Kae Nemoto, T. C. Ralph, Jonathan P. Dowling, and G. J. Milburn: *Linear optical quantum computing with photonic qubits.* Rev. Mod. Phys., 79(1):135–174, 2007.

[4] H. J. Kimble: *The quantum internet.* Nature, 453:1023–1030, 2008.

[5] E. Lundström, G. Brodin, J. Lundin, M. Marklund, R. Bingham, J. Collier, J. T. Mendonça, and P. Norreys: *Using high-power lasers for detection of elastic photon-photon scattering.* Physical Review Letters, 96(8):083602, 2006.

[6] S. E. Harris and L. V. Hau: *Nonlinear optics at low light levels.* Phys. Rev. Lett., 82:4611–4614, 1999.

[7] M. Fleischhauer, A. Imamoğlu, and J.P. Marangos: *Electromagnetically induced transparency: Optics in coherent media.* Rev. Mod. Phys., 77(633):633–673, 2005.

[8] E. Vetsch, D. Reitz, G. Sagué, R. Schmidt, S. T. Dawkins, and A. Rauschenbeutel: *Optical interface created by laser-cooled atoms trapped in the evanescent field surrounding an optical nanofiber.* Phys. Rev. Lett., 104(20):203603, 2010.

[9] Eugen Vetsch: *Optical Interface Based on a Nanofiber Atom-Trap.* PhD thesis, Johannes Gutenberg-Universität Mainz, Group of Prof. A. Rauschenbeutel, Dec 2010.

[10] Bernd Kaltenhuser, Harald Kbler, Andreas Chromik, Jrgen Stuhler, Tilman Pfau, and Atac Imamoglu: *Narrow bandwidth electromagnetically induced transparency in optically trapped atoms.* Journal of Physics B: Atomic, Molecular and Optical Physics, 40(10):1907, 2007.

[11] N. Papasimakis and N. Zheludev: *Metamaterial-induced transparency: Sharp fano resonances and slow light.* Opt. Photon. News, 20(10):22–27, 2009.

[12] A. H. Safavi-Naeini, T. P. Mayer Alegre, J. Chan, M. Eichenfield, M. Winger, Q. Lin, J. T. Hill, D. E. Chang, and O. Painter: *Electromagnetically induced transparency and slow light with optomechanics.* Nature, 472:69–73, 2011.

[13] M. P. Hedges, J. J. Longdell, Y. Li, and M. J. Sellars: *Efficient quantum memory for light.* Nature, 465:1052–1056, 2010.

[14] E. Togan, Y. Chu, A. S. Trifonov, L. Jiang, J. Maze, L. Childress, M. V. G. Dutt, A. S. Srensen, P. R. Hemmer, A. S. Zibrov, and M. D. Lukin: *Quantum entanglement between an optical photon and a solid-state spin qubit.* Nature, 466:730–734, 2010.

[15] Melanie Müller: *Realization and characterization of a phase locked laser system for coherent spectroscopy of fiber-coupled cesium atoms.* Diplomarbeit, Johannes Gutenberg Universität Mainz, July 2010. Group of Prof. A. Rauschenbeutel.

[16] Daniel M. Greenberger, Michael A. Horne, and Anton Zeilinger: *Multiparticle interferometry and the superposition principle.* Physics Today, 46(8):22–29, 1993.

[17] Erwin Schrödinger: *Die gegenwärtige Situation in der Quantenmechanik.* Naturwissenschaften, 23(48):807–812, 1935.

[18] A. Einstein, B. Podolsky, and N. Rosen: *Can quantum-mechanical description of physical reality be considered complete?* Phys. Rev., 47(10):777–780, 1935.

[19] John Stuard Bell: *Speakable and Unspeakable in Quantum Mechanics – Collected Papers on Quantum Philosophy.* Cambridge University Press, Cambridge (UK), 2004.

[20] Thomas Jennewein, Ulrich Achleitner, Gregor Weihs, Harald Weinfurter, and Anton Zeilinger: *A fast and compact quantum random number generator.* Rev. Sci. Instrum., 71(4):1675–1680, 2000.

[21] S. Pironio, A. Acín, S. Massar, A. Boyer de la Giroday, D. N. Matsukevich, P. Maunz, S. Olmschenk, D. Hayes, L. Luo, T. A. Manning, and C. Monroe: *Random numbers certified by bells theorem.* Nature, 464:1021–1024, 2010.

[22] John Archibald Wheeler and Wojciech Hubert Zurek (editors): *Quantum Theory and Measurement.* Princeton University Press, Princeton, 1984.

[23] Asher Peres: *Quantum Theory: Concepts and Methods.* Kluwer Academic, New York, Boston, Dordrect, London, Moscow, 1. edition, 2002.

[24] A. L. Schawlow and C. H. Townes: *Infrared and optical masers.* Phys. Rev., 112(6):1940–1949, 1958.

[25] T.H. Maiman: *Stimulated optical radiation in ruby.* Nature, 187:493–494, 1960.

[26] C.H. Bennett and G. Brassard: *Quantum cryptography: Public key distribution and coin tossing.* In *Proceedings of IEEE International Conference on Computers Systems and Signal Processing*, pages 175–179. IEEE Press, 1984.

[27] Artur K. Ekert: *Quantum cryptography based on bell's theorem.* Phys. Rev. Lett., 67(6):661–663, 1991.

[28] Earl T. Campbell: *Distributed quantum-information processing with minimal local resources.* Phys. Rev. A, 76(4):040302, 2007.

[29] Liang Jiang, Jacob M. Taylor, Anders S. Sørensen, and Mikhail D. Lukin: *Distributed quantum computation based on small quantum registers.* Phys. Rev. A, 76(6):062323, 2007.

[30] Charles H. Bennett, Gilles Brassard, Claude Crépeau, Richard Jozsa, Asher Peres und William K. Wootters: *Teleporting an unknown quantum state via dual classical and Einstein-Podolsky-Rosen channels.* Phys. Rev. Lett., 70(13):1895–1899, 1993.

[31] M. Żukowski, A. Zeilinger, M. A. Horne, and A. K. Ekert: *"event-ready-detectors" bell experiment via entanglement swapping.* Phys. Rev. Lett., 71(26):4287–4290, 1993.

[32] Charles H. Bennett, Gilles Brassard, Sandu Popescu, Benjamin Schumacher, John A. Smolin, and William K. Wootters: *Purification of noisy entanglement and faithful teleportation via noisy channels.* Phys. Rev. Lett., 76(5):722–725, 1996.

[33] Robert Raussendorf and Hans J. Briegel: *A one-way quantum computer.* Phys. Rev. Lett., 86:5188–5191, 2001.

[34] Michael A. and Nielsen: *Cluster-state quantum computation.* Reports on Mathematical Physics, 57(1):147–161, 2006.

[35] E. Knill, R. Laflamme, and G. J. Milburn: *A scheme for efficient quantum computation with linear optics.* Nature, 409:46–52, 2001.

[36] P. Walther, K. J. Resch, T. Rudolph, E. Schenck, H. Weinfurter, V. Vedral, M. Aspelmeyer, and A. Zeilinger: *Experimental one-way quantum computing.* Nature, 434:169–176, 2005.

[37] C. Y. Lu, X. Q. Zhou, O. Gühne, W. B. Gao, J. Zhang, Z. S. Yuan, A. Goebel, T. Yang, and J. W. Pan: *Experimental entanglement of six photons in graph states.* Nature Physics, 3:91–95, 2007.

[38] M. Fleischhauer and M. D. Lukin: *Quantum memory for photons: Dark-state polaritons.* Phys. Rev. A, 65(2):022314, 2002.

[39] H. J. Briegel, W. Dür, J. I. Cirac, and P. Zoller: *Quantum repeaters: The role of imperfect local operations in quantum communication.* Phys. Rev. Lett., 81(26):5932–5935, 1998.

[40] A. Kuzmich, W. P. Bowen, A. D. Boozer, A. Boca, L. M. Chou, C. W.and Duan, and H. J. Kimble: *Generation of nonclassical photon pairs for scalable quantum communication with atomic ensembles.* Nature, 423:731–734, 2003.

[41] Shuai Chen, Yu Ao Chen, Thorsten Strassel, Zhen Sheng Yuan, Bo Zhao, Jörg Schmiedmayer, and Jian Wei Pan: *Deterministic and storable single-photon source based on a quantum memory.* Phys. Rev. Lett., 97(17):173004, 2006.

[42] Alexander I. Lvovsky, Barry C. Sanders, and Wolfgang Tittel: *Optical quantum memory.* Nature Photonics, 3:706–714, 2009.

[43] M. D. Lukin: *Colloquium: Trapping and manipulating photon states in atomic ensembles.* Rev. Mod. Phys., 75(2):457–472, 2003.

[44] S. E. Harris, J. E. Field, and A. Imamoğlu: *Nonlinear optical processes using electromagnetically induced transparency.* Phys. Rev. Lett., 64(10):1107–1110, 1990.

[45] Tony Y. Abi-Salloum: *Electromagnetically induced transparency and autler-townes splitting: Two similar but distinct phenomena in two categories of three-level atomic systems.* Phys. Rev. A, 81:053836, 2010.

[46] Petr M. Anisimov, Jonathan P. Dowling, and Barry C. Sanders: *Objectively discerning autler-townes splitting from electromagnetically induced transparency.* Phys. Rev. Lett., 107:163604, 2011.

[47] S. H. Autler and C. H. Townes: *Stark effect in rapidly varying fields.* Phys. Rev., 100(2):703–722, 1955.

[48] Lene V. Hau, S. E. Harris, Zachary Dutton, and Cyrus H. Behroozi: *Light speed reduction to 17 metres per second in an ultracold atomic gas.* Nature, 397:594–598, 1999.

[49] M. Fleischhauer and M. D. Lukin: *Dark-state polaritons in electromagnetically induced transparency.* Phys. Rev. Lett., 84(22):5094–5097, 2000.

[50] Alexey V. Gorshkov, Axel André, Michael Fleischhauer, Anders S. Sørensen, and Mikhail D. Lukin: *Universal approach to optimal photon storage in atomic media.* Phys. Rev. Lett., 98(12):123601, 2007.

[51] Yu Ao Chen, Shuai Chen, Zhen Sheng Yuan, Bo Zhao, Chih Sung Chuu, Jörg Schmiedmayer, and Jian Wei Pan: *Memory-built-in quantum teleportation with photonic and atomic qubits.* Nature Physics, 4:103–107, 2008.

[52] K. J. Boller, A. Imamoğlu, and S. E. Harris: *Observation of electromagnetically induced transparency.* Phys. Rev. Lett., 66(20):2593–2596, 1991.

[53] Chien Liu, Zachary Dutton, Cyrus H. Behroozi, and Lene Vestergaard Hau: *Observation of coherent optical information storage in an atomic medium using halted light pulses.* Nature, 409:490–493, 2001.

[54] D. F. Phillips, A. Fleischhauer, A. Mair, R. L. Walsworth, and M. D. Lukin: *Storage of light in atomic vapor.* Phys. Rev. Lett., 86(5):783–786, 2001.

[55] Holger P. Specht, Christian Nlleke, Andreas Reiserer, Manuel Uphoff, Eden Figueroa, Stephan Ritter, and Gerhard Rempe: *A single-atom quantum memory.* Nature, 473:190–193, 2011.

[56] C. G. B. Garrett and D. E. McCumber: *Propagation of a gaussian light pulse through an anomalous dispersion medium.* Phys. Rev. A, 1(2):305–313, 1970.

[57] Michael D. Stenner, Daniel J. Gauthier, and Mark A. Neifeld: *The speed of information in a 'fast-light' optical medium.* Nature, 425:695–698, 2003.

[58] George M. Gehring, Aaron Schweinsberg, Christopher Barsi, Natalie Kostinski, and Robert W. Boyd: *Observation of backward pulse propagation through a medium with a negative group velocity.* Science, 312(5775):895–897, 2006.

[59] Robert W. Boyd: *Slow and fast light: fundamentals and applications.* Journal of Modern Optics, 56(18):1908–1915, 2009.

[60] Léon Brillouin: *Wave Propagation and Group Velocity.* Academic Press, 3. edition, 1964.

[61] S. Chu and S. Wong: *Linear pulse propagation in an absorbing medium.* Phys. Rev. Lett., 48(11):738–741, 1982.

[62] Raymond Y. Chiao and Aephraim M. Steinberg: *Tunneling times and superluminality.* Progress in Optics (ed. Wolf, E.), 37:345–405, 1997.

[63] Miguel González-Herráez, Kwang Yong Song, and Luc Thévenaz: *Optically controlled slow and fast light in optical fibers using stimulated brillouin scattering.* Applied Physics Letters, 87(8):081113, 2005.

[64] G.A. Reider: *Photonik - Eine Einfhrung in die Grundlagen.* Springer-Verlag, Berlin, Heidelberg, New York, 2. Auflage, 2004.

[65] I. I. Rabi: *Space quantization in a gyrating magnetic field.* Phys. Rev., 51(8):652–654, 1937.

[66] Christopher C. Gerry and Peter L. Knight: *Introductory Quantum Optics.* Cambridge University Press, 1st edition, 2006.

[67] M. Brune, F. Schmidt-Kaler, A. Maali, J. Dreyer, E. Hagley, J. M. Raimond, and S. Haroche: *Quantum rabi oscillation: A direct test of field quantization in a cavity.* Phys. Rev. Lett., 76:1800–1803, 1996.

[68] G. Alzetta, A. Gozzini, L. Moi, and G. Orriols: *An experimental method for the observation of r.f. transitions and laser beat resonances in oriented na vapour.* Il Nuovo Cimento B (1971-1996), 36:5–20, 1976.

[69] A. Aspect, E. Arimondo, R. Kaiser, N. Vansteenkiste, and C. Cohen-Tannoudji: *Laser cooling below the one-photon recoil energy by velocity-selective coherent population trapping.* Phys. Rev. Lett., 61:826–829, 1988.

[70] K. Bergmann, H. Theuer, and B. W. Shore: *Coherent population transfer among quantum states of atoms and molecules.* Rev. Mod. Phys., 70(3):1003–1025, 1998.

[71] U. Gaubatz, P. Rudecki, S. Schiemann, and K. Bergmann: *Population transfer between molecular vibrational levels by stimulated raman scattering with partially overlapping laser fields: A new concept and experimental results.* The Journal of Chemical Physics, 92(9):5363–5376, 1990.

[72] Nikolay V Vitanov, Thomas Halfmann, Bruce W Shore, and Klaas Bergmann: *Laser-induced population transfer by adiabatic passage techniques.* Annual Review of Physical Chemistry, 52(1):763–809, 2001.

[73] O. A. Kocharovskaya and I. I. Khanin: *Coherent amplification of an ultrashort pulse in a three-level medium without population inversion.* Pis ma Zhurnal Eksperimental noi i Teoreticheskoi Fiziki, 48:581–584, 1988.

[74] S. E. Harris: *Lasers without inversion: Interference of lifetime-broadened resonances.* Phys. Rev. Lett., 62:1033–1036, 1989.

[75] J. Mompart and R Corbalán: *Lasing without inversion.* Journal of Optics B: Quantum and Semiclassical Optics, 2(3):R7, 2000.

[76] Alexey V. Gorshkov: *Novel Systems and Methods for Quantum Communication, Quantum Computation, and Quantum Simulation.* PhD thesis, Harvard University, Cambridge, Massachusetts, Nov 2009.

[77] Claude Cohen-Tannoudji, Jaques Dupont-Roc, and Gilbert Grynberg: *Atom-Photon interactions - Basic processes and applications.* Wiley-VCH, 1998.

[78] Stephen P. Smith, Sameer R. Bhalotra, Anne L. Brody, Benjamin L. Brown, Edward K. Boyda, and Mara Prentiss: *Inexpensive optical tweezers for undergraduate laboratories.* American Journal of Physics, 67(1):26–35, 1999.

[79] M.D. Wang, H. Yin, R. Landick, J. Gelles, and S.M. Block: *Stretching dna with optical tweezers.* Biophysical Journal, 72(3):1335 – 1346, 1997, ISSN 0006-3495.

[80] David G. Grier: *A revolution in optical manipulation.* Nature, 424:810–816, 2003.

[81] Jeffrey R. Moffitt, Yann R. Chemla, Steven B. Smith, and Carlos Bustamante: *Recent advances in optical tweezers.* Annual Review of Biochemistry, 77(1):205–228, 2008.

[82] Keir C. Neuman and Attila Nagy: *Single-molecule force spectroscopy: optical tweezers, magnetic tweezers and atomic force microscopy.* Nature Methods, 5:491–505, 2008.

[83] A. Ashkin: *Trapping of atoms by resonance radiation pressure.* Phys. Rev. Lett., 40:729–732, 1978.

[84] Steven Chu, Arthur Ashkin, and A. Cable: *Experimental observation of optically trapped atoms.* Physical Review Letters, 57(3):314, 1986.

[85] Rudolf Grimm, Matthias Weidemller, and Yurii B. Ovchinnikov: *Optical dipole traps for neutral atoms.* Advances In Atomic, Molecular, and Optical Physics, 42:95–170, 2000.

[86] Florian Warken: *Ultradünne Glasfasern als Werkzeug zur Kopplung von Licht und Materie.* Dissertation, Rheinischen Friedrich-Wilhelms-Universität Bonn, 2007.

[87] Guillem Sagué Cassany: *Cold atom physics using ultra-thin optical fibres.* PhD thesis, Rheinischen Friedrich-Wilhelms-Universität Bonn, 2008.

[88] Ulrich Tietze und Christoph Schenk: *Halbleiterschaltungstechnik.* Springer-Verlag, Berlin, Heidelberg, New York, 10. Auflage, 1993.

[89] Karl Heinz Rohe: *Elektronik für Physiker.* Teubner, Stuttgart, 3. Auflage, 1978.

[90] Karl Johan Åström and Richard M. Murray: *Feedback Systems: An Introduction for Scientists and Engineers.* Princeton University Press, Princeton, 2nd edition, 2009.

[91] John Bechhoefer: *Feedback for physicists: A tutorial essay on control.* Rev. Mod. Phys., 77(3):783–836, 2005.

[92] Simon Hooker and Colin Webb: *Laser Physics.* Oxford Master Seriess in Atomic, Optical and Laser Physics. Oxford University Press, 1st edition, 2010.

[93] *Temperature-dependent refractive index of silicon and germanium*, volume 6273, Orlando, FL (USA), 2006. SPIE.

[94] Cunyun Ye: *Tunable external cavity diode lasers.* World Scientific, Singapore, 1st edition, 2004.

[95] Maurice G. A. Bernard and Georges Duraffourg: *Laser conditions in semiconductors.* physica status solidi (b), 1(7):699–703, 1961, ISSN 1521-3951.

[96] Carl E. Wieman and Leo Hollberg: *Using diode lasers for atomic physics.* Rev. Sci. Instrum., 62(1), 1991.

[97] Newport Corporation, Irvine, California: *Laser Diode Technology Tutorial*, July 2011. http://www.newport.com/Tutorial-Laser-Diode-Technology/852182/1033/content.aspx.

[98] Sacher Lasertechnik Group: *Anti-reflection coated diode lasers.* Product Catalogue, 2011.

[99] L. Ricci, M. Weidemller, T. Esslinger, A. Hemmerich, C. Zimmermann, V. Vuletic, W. Knig, and T. W. Hnsch: *A compact grating-stabilized diode laser system for atomic physics.* Optics Communications, 117(5-6):541–549, 1995, ISSN 0030-4018.

[100] C. J. Hawthorn, K. P. Weber, and R. E. Scholten: *Littrow configuration tunable external cavity diode laser with fixed direction output beam.* Rev. Sci. Instrum., 72:4477, 2001.

[101] Michael G. Littman and Harold J. Metcalf: *Spectrally narrow pulsed dye laser without beam expander.* Appl. Opt., 17(14):2224–2227, 1978.

[102] Jr. Trutna, W.R. and L.F. Stokes: *Continuously tuned external cavity semiconductor laser.* Journal of Lightwave Technology, 11(8):1279–1286, 1993.

[103] L. Levin: *Mode-hop-free electro-optically tuned diode laser.* Opt. Lett., 27(4):237–239, 2002.

[104] M. Bagley, R. Wyatt, D.J. Elton, H.J. Wickes, P.C. Spurdens, C.P. Seltzer, D.M. Cooper, and W.J. Devlin: *242 nm continuous tuning from a grin-sc-mqw-bh ingaasp laser in an extended cavity.* Electronics Letters, 26(4):267–269, 1990.

[105] K. B. MacAdam, A. Steinbach, and C. Wieman: *A narrow-band tunable diode laser system with grating feedback, and a saturated absorption spectrometer for cs and rb.* Am. J. Phys., 60(12):1098–1111, 1992, ISSN 00029505.

[106] M. Fleming and A. Mooradian: *Spectral characteristics of external-cavity controlled semiconductor lasers.* Quantum Electronics, IEEE Journal of, 17(1):44–59, 1981.

[107] R. V. Pound: *Electronic frequency stabilization of microwave oscillators.* Rev. Sci. Instrum., 17(11):490–505, 1946.

[108] R. W. P. Drever, J. L. Hall, F. V. Kowalski, J. Hough, G. M. Ford, A. J. Munley, and H. Ward: *Laser phase and frequency stabilization using an optical resonator.* Appl. Phys. B, 31(2):97–105, 1983.

[109] John L. Hall, Matthew S. Taubman, and Jun Ye: *Laser stabilization.* In M. Bass, J. M. Enoch, E. W. Van Stryland, and W. L. Wolfe (editors): *Optics Handbook*, pages 27.1–27.24. Optical Society of America, 2000.

[110] Eric D. Black: *An introduction to pound-drever-hall laser frequency stabilisation.* Am. J. Phys., 69(1):79–87, 2001.

[111] T. W. Hänsch and B. Couillaud: *Laser frequency stabilization by polarization spectroscopy of a reflecting reference cavity.* 35(3):441–444, 1980.

[112] G. Ritt, G. Cennini, C. Geckeler, and M. Weitz: *Laser frequency offset locking using a side of filter technique.* Appl. Phys. B, 79:363–365, 2004.

[113] T. W. Hänsch, M. D. Levenson, and A. L. Schawlow: *Complete hyperfine structure of a molecular iodine line.* Phys. Rev. Lett., 26(16):946–949, 1971.

[114] Gary C. Bjorklund: *Frequency-modulation spectroscopy: a new method for measuring weak absorptions and dispersions.* Opt. Lett., 5(1):15–17, 1980.

[115] G. C. Bjorklund, M. D. Levenson, W. Lenth, and C. Ortiz: *Frequency modulation (fm) spectroscopy.* Appl. Phys. B, 32:145–152, 1983.

[116] C. Wieman and T. W. Hänsch: *Doppler-free laser polarization spectroscopy.* Phys. Rev. Lett., 36(20):1170–1173, 1976.

[117] Yaakov Shevy and Hua Deng: *Frequency-stable and ultranarrow-linewidth semiconductor laser locked directly to an atomic-cesium transition.* Opt. Lett., 23(6):472–474, 1998.

[118] C.P. Pearman, C.S. Adams, S.G. Cox, P.F. Griffin, D.A. Smith, and I.G. Hughes: *Polarization spectroscopy of a closed atomic transition: applications to laser frequency locking.* J. Phys. B: At. Mol. Opt. Phys., 35:5141–5151, 2002.

[119] A. Ratnapala, C. J. Vale, A. G. White, M. D. Harvey, N. R. Heckenberg, and H. Rubinsztein-Dunlop: *Laser frequency locking by direct measurement of detuning.* Opt. Lett., 29(23):2704–2706, 2004.

[120] Wolfgang Alt: *Optical control of single neutral atoms.* Phd thesis, Rheinische Friedrich-Wilhelms-Universität Bonn, 2004.

[121] F.M. Gardner: *Phaselock Techniques.* Wiley, 3rd edition, 2005.

[122] Andrew Leven: *Telecommunication circuits and technology.* Butterworth-Heinemann, 1st edition, 2000.

[123] L.H. Enloe and J.L. Rodda: *Laser phase-locked loop.* Proceedings of the IEEE, 53(2):165–166, 1965, ISSN 0018-9219.

[124] R. Wynands and A. Nagel: *Precision spectroscopy with coherent dark states.* Appl. Phys. B, 68:1–25, 1999.

[125] Miao Zhu and John L. Hall: *Stabilization of optical phase/frequency of a laser system: application to a commercial dye laser with an external stabilizer.* J. Opt. Soc. Am. B, 10(5):802–816, 1993.

[126] Norbert Wiener: *Generalized harmonic analysis.* Acta Mathematica, 55, 1930.

[127] A. Khintchine: *Korrelationstheorie der stationären stochastischen Prozesse.* Mathematische Annalen, 109:604, 1934.

[128] Donald R. Stephens: *Phase-Locked Loops for Wireless Communications - Digital, Analog and Optical Implementations.* Kluwer Academic, New York, 2nd edition, 2002.

[129] A. Hajimiri and T.H. Lee: *A general theory of phase noise in electrical oscillators.* Solid-State Circuits, IEEE Journal of, 33(2):179–194, 1998.

[130] Mike Curtin and Paul OBrien: *Phase-locked loops for high-frequency receivers and transmitters: i-iii.* Analog Dialogue, 33:9, 1999.

[131] M. Prevedelli, T. Freegarde, and T. W. Hänsch: *Phase locking of grating-tuned diode lasers.* Appl. Phys. B, 60:S241–S248, 1995.

[132] Jürgen Appel, Andrew MacRae, and A.I. Lvovsky: *A versatile digital ghz phase lock for external cavity diode lasers.* Measurement Science and Technology, 20(5):055302, 2009.

[133] B.E.A. Saleh und M.C. Teich: *Grundlagen der Photonik.* Wiley-VCH, Weinheim, 2. Auflage, 2008.

[134] Eugene Hecht: *Optics.* Addison Wesley, San Francisco, CA (USA), 2002.

[135] Erwin G. Loewen and Evgeny Popov: *Diffraction Gratings and Applications.* Marcel Dekker, Inc., New York, 1st edition, 1997.

[136] Wolfgang Demtröder: *Experimentalphysik 2, Elektrizität und Optik.* Springer, Berlin, 5. Auflage, 2009.

[137] Christopher Palmer and Erwin Loewen: *Diffraction Grating Handbook.* Newport Corporation, Rochester, New York, 6th edition, 2005.

[138] Tapan K. Sarkar, Robert Mailloux, Arthur A. Oliner, M. Salazar-Palma, and Dipak L. Sengupta: *History of wireless.* John Wiley and Sons, Hoboken, NJ (USA), 2006.

[139] J. Salz: *Modulation and detection for coherent lightwave communications.* Communications Magazine, IEEE, 24(6):38–49, 1986, ISSN 0163-6804.

[140] J.R. Barry and E.A. Lee: *Performance of coherent optical receivers.* Proceedings of the IEEE, 78(8):1369–1394, 1990.

[141] Harry J.R. Dutton: *Understanding Optical Communication.* IBM Corporation, 1st edition, 1998.

[142] Govind P. Agrawal: *Lightwave Technology – Telecommunication Systems.* Wiley.

[143] John M. Senior and M. Yousif Jamro: *Optical Fiber telecommunications – Principles and Pracitce.* Pearson Education Ltd., 3rd edition, 2009.

[144] M. R. Vanner, I. Pikovski, M. S. Kim, C. Brukner, K. Hammerer, G. J. Milburn, and M. Aspelmeyer: *Pulsed quantum optomechanics.* arXiv:1011.0879v1, 2010.

[145] M. A. Johnson and C. H. Townes: *Quantum effects and optimization of heterodyne detection.* Optics Communications, 179(1-6):183–187, 2000.

[146] Hans A. Bachor and Timothy C. Ralph: *A Guide to Experiments in Quantum Optics.* Wiley-VCH, Weinheim, 2. edition, 2004.

[147] Horace P. Yuen and Vincent W.S. Chan: *Noise in homodyne and heterodyne detection.* Opt. Lett., 8(3):177–179, 1983.

[148] A. Zeilinger: *General properties of lossless beam splitters in interferometry.* American Journal of Physics, 49(9):882–883, 1981.

[149] Rüdiger Paschotta: *Encyclopedia of Laser Physics and Technology.* Wiley-VCH, Berlin, 2008.

[150] Charles H. Henry and Rudolf F. Kazarinov: *Quantum noise in photonics.* Rev. Mod. Phys., 68(3):801–853, 1996.

[151] Carlton M. Caves: *Quantum limits on noise in linear amplifiers.* Phys. Rev. D, 26(8):1817–1839, 1982.

[152] U. Leonhardt and H. Paul: *Measuring the quantum state of light.* 19:89–130, 1995.

[153] Carlton M. Caves: *Quantum-mechanical noise in an interferometer.* Phys. Rev. D, 23(8):1693–1708, 1981.

[154] Robert Kingston: *Detection of optical and infrared radiation.* Springer, 2nd edition, 1979.

[155] Leonid G. Kazovsky: *Optical heterodyning versus optical homodyning: A comparison.* Journal of Optical Communications, 6(1):18–24, 1985.

[156] William H. Press, Saul A. Teukolsky, William T. Vetterling, and Brian P. Flannery: *Numerical recipes - The art of scientific computing.* Cambridge University Press, Cambridge (UK), 3rd edition, 2007.

[157] Thomas Frey und Martin Bossert: *Signal- und Systemtheorie.* Vieweg+Teubner, Wiesbaden, 2. Auflage, 2008.

[158] Roy J. Glauber: *Coherent and incoherent states of the radiation field.* Phys. Rev., 131(6):2766–2788, 1963.

[159] L. Mandel and E. Wolf: *Coherence properties of optical fields.* Rev. Mod. Phys., 37(2):231–287, 1965.

[160] T. Opatrný, M. Dakna, and D. G. Welsch: *Number-phase uncertainty relations: Verification by balanced homodyne measurement.* Phys. Rev. A, 57(3):2129–2133, 1998.

[161] Gerd Breitenbach: *A gallery of quantum states.* online, Oct 2011. `http://gerdbreitenbach.de/gallery/`.

[162] D. T. Smithey, M. Beck, M. G. Raymer, and A. Faridani: *Measurement of the wigner distribution and the density matrix of a light mode using optical homodyne tomography: Application to squeezed states and the vacuum.* Phys. Rev. Lett., 70(9):1244–1247, 1993.

[163] Roy J. Glauber: *The quantum theory of optical coherence.* Phys. Rev., 130(6):2529–2539, 1963.

[164] Roy J. Glauber: *Quantum theory of optical coherence.* WILEY-VCH, Weinheim, 1st edition, 2007.

[165] Malvin C. Teich: *Quantum theory of heterodyne detection.* In E. M. Pell (editor): *Proc. Third Photocond. Conf.*, pages 1–5, New York, 1971. Pergamon Press.

[166] Howard Carmichael: *An Open Systems Approach to Quantum Optics, Lectures Presented at the Universit Libre de Bruxelles October 28 to November 4, 1991.* Lecture Notes in Physics monographs. Springer, Berlin, Heidelberg, 1st edition, 1993.

[167] D.F. Walls and Gerald J. Milburn: *Quantum Optics.* Springer, 2nd edition, 2008.

[168] Wolfgang Demtröder: *Laser Spectroscopy*, volume 1 & 2. Springer, Heidelberg, 4th edition, 2008.

[169] D.N. Klyshko and Anatolii V. Masalov: *Photon noise: observation, squeezing, interpretation.* Physics-Uspekhi, (11):1203, 1995.

[170] H. J. Carmichael: *Spectrum of squeezing and photocurrent shot noise: a normally ordered treatment.* J. Opt. Soc. Am. B, 4(10):1588–1603, 1987.

[171] Ch. Raab, J. Eschner, J. Bolle, H. Oberst, F. Schmidt-Kaler, and R. Blatt: *Motional sidebands and direct measurement of the cooling rate in the resonance fluorescence of a single trapped ion.* Phys. Rev. Lett., 85(3):538–541, 2000.

[172] Fam Le Kien, V. I. Balykin, and K. Hakuta: *Atom trap and waveguide using a two-color evanescent light field around a subwavelength-diameter optical fiber.* Phys. Rev. A, 70(6):063403, 2004.

[173] Daniel A. Steck: *Cesium d line data.* available online, Dec 2010. `http://steck.us/alkalidata/`, revision 2.1.4.

[174] E. A. Donley, T. P. Heavner, F. Levi, M. O. Tataw, and S. R. Jefferts: *Double-pass acousto-optic modulator system.* 76(6):063112, 2005.

[175] Chih Hao Chang, R. K. Heilmann, M. L. Schattenburg, and P. Glenn: *Design of a double-pass shear mode acousto-optic modulator.* 79(3):033104, 2008.

[176] Agilent Technologies, Inc.: *Spectrum Analyzer Measurements and Noise (Application Note 1303)*, Sep 2009. `http://cp.literature.agilent.com/litweb/pdf/5966-4008E.pdf`.

[177] L. Cacciapuoti, M. de Angelis, M. Fattori, G. Lamporesi, T. Petelski, M. Prevedelli, J. Stuhler, and G. M. Tino: *Analog + digital phase and frequency detector for phase locking of diode lasers.* Rev. Sci. Instrum., 76(5):053111–7, 2005.

[178] Alberto M. Marino and Jr. C. R. Stroud: *Phase-locked laser system for use in atomic coherence experiments.* Rev. Sci. Instrum., 79(1):013104, 2008.

[179] D. Höckel, M. Scholz und O. Benson: *A robust phase-locked diode laser system for EIT experiments incesium.* Appl. Phys. B, 94:429–435, 2009.

[180] M. Scholz, L. Koch, R. Ullmann, and O. Benson: *Single-mode operation of a high-brightness narrow-band single-photon source.* 94(20):201105, 2009, ISSN 00036951.

[181] David G. Blair (editor): *The detection of gravitational waves.* Cambridge University Press, 2005.

[182] *Tholabs inc. online product catalogue*, November 2011. `http://www.thorlabs.com/`.

[183] *Newport corporation online product catalogue*, November 2011. `http://www.newport.com/`.

[184] R. De L. Kronig: *On the theory of dispersion of x-rays.* J. Opt. Soc. Am., 12(6):547–556, 1926.

[185] *NI LabVIEW 8.6 Help (NI Part Number: 371361E-01)*, June 2008. `http://zone.ni.com/reference/en-XX/help/371361E-01/`.

[186] F.J. Harris: *On the use of windows for harmonic analysis with the discrete fourier transform.* Proceedings of the IEEE, 66(1):51–83, 1978.

[187] A. Nuttall: *Some windows with very good sidelobe behavior.* Acoustics, Speech and Signal Processing, IEEE Transactions on, 29(1):84 – 91, 1981.

Acknowledgments

Ein Leben ohne Mops ist möglich, aber sinnlos.

_____

Loriot

Prof. Arno Rauschenbeutel möchte ich für die Möglichkeit danken an einem Teil dieses wunderschönen Experiments gearbeitet haben zu dürfen, einem Experiment, das sowohl durch sein Potenzial fundamentale Physik zu untersuchen, als auch seine Realisierung mittels Fasertechnologie einen besonderen Reiz ausmacht. Die Gespräche mit Arno waren stets lehrreich und inspirierend.

Unserem Projektassistenten Philipp Schneeweiß, genauso wie den Doktoranden Daniel Reitz und Rudolf Mitsch, möchte ich für die Durchsicht meiner schriftlichen Arbeit und hilfreichen Anmerkungen danken. Ebenso möchte ich ihnen danken, dass sie mir eine sehr selbstständige Arbeitsweise ermöglicht haben, durch die ich meinen Erfahrungshorizont erweitern konnte. Daniel möchte ich darüber hinaus danken, dass er sich vor allem im letzten Monat einige meiner Ideen und Überlegungen zum Homodyne-Experiment angehört hat und fruchtbares Feedback zurückgab. Auch Christian Wuttke möchte ich für einige wichtige Leihgaben und ein paar wertvolle Diskussionen zum Homodyne-Experiment danken.

I also want to thank Michael Vanner from Prof. Markus Aspelmayer's group, with whom I had a very interesting and inspiring discussion about heterodyne and homodyne detection.

Unserer Nachbargruppe unter der Leitung von Prof. Schmiedmayer und Prof. Schumm möchte ich sehr herzlich für die vielen Leihgaben danken, ohne die meine Phasenlock-Messungen nicht in der Art hätten realisiert werden können. Vielen Dank für eure Bereitschaft und euer Vertrauen!

Meiner Familie gebührt besonderer Dank für all ihre Liebe und Unterstützung in allen Phasen meines Lebens. Manchmal war es besonders schwer, so lange von meinen Eltern, meiner Schwester Lucia, meinem Schwager Fabian, meinem kleinen Neffen Leo und natürlich auch Labradorhündin Lissy und meinen Kaninchen Ruby und Finchen getrennt zu sein. Daher möchte ich mich auch beim Skype-Team für die Bereitstellung eines Mediums danken, über das ich so gut wie möglich mit ihnen allen in Kontakt bleiben konnte. Ohne die stetige emotionale und finanzielle Unterstützung meiner fürsorglichen Eltern wäre dieser Studien- und Forschungsaufenthalt in Wien nicht möglich gewesen. Es sind die harten Zeiten, in denen man erkennt, auf wen man sich am meisten verlassen kann und was im Leben wirklich wichtig ist!

Zu guter Letzt möchte ich mich von ganzem Herzen bei David bedanken, mit dem ich nicht nur eine tiefe Leidenschaft für Physik teile. Mit ihm habe ich (trotz der 600 km räumlichen Trennung) das letzte Jahr über noch mehr über Physik und die Welt diskutiert, als mit irgend jemandem sonst. Ich bin froh, dass wir jetzt nicht mehr so weit voneinander getrennt sein werden. Danke, dass du mein Leben über alle Maßen bereicherst!

Silvia B. Arroyo Camejo

Curriculum Vitae

Personal data

First name: Silvia
Middle name: Bettina
Family name: Arroyo Camejo
Citizenship: German, Spanish

Address: Sendener Weg 57
13507 Berlin
Germany
E-mail: s.arroyocamejo@ati.ac.at

Education

Since Oct. 2009 **Graduate studies in physics (M.Sc.)**, *University of Vienna, Department of Physics*, Vienna, Austria

March 2009 - September 2009 **Graduate visiting student in physics**, *Massachusetts Institute of Technology, Department of Physics*, Cambridge, Massachusetts, USA

October 2005 - March 2009 **Undergraduate studies in physics (B.Sc.)**, *Humboldt University Berlin, Department of Physics*, Berlin, Germany

July 2005 **Abitur (German university entrance qualification)**, *Canisius-Kolleg (private, humanistic high school)*, Berlin, Germany, Main subjects: physics, chemistry

Practical work experience

Since Dec. 2010 **Graduate student**, *Vienna University of Technology, Institute of Atomic and Subatomic Physics, Group of Prof. A. Rauschenbeutel,* Vienna, Austria

March 2009 - Sept. 2009 **Graduate research assistant**, *MIT-Harvard University Center for Ultracold Atoms, Experimental Atomic Physics Group of Prof. V. Vuletic*, Cambridge, Massachusetts, USA

March 2008 - February 2009 **Undergraduate student**, *Humboldt University Berlin, Department of Physics, Nano Optics Group of Prof. O. Benson*, Berlin, Germany

Nov. 2006 - April 2007 **Undergraduate research assistant**, *Helmholtz Center Berlin for Materials and Energy (former : Hahn-Meitner-Institute), Department of Silicon Photovoltaic, Group of Dr. K. Lips*, Berlin, Germany

October 2005 - March 2008 **Undergraduate research assistant**, *Hahn-Meitner-Institute, Department of Solar Energy, Group of Dr. M. Kunst and Prof. H. Tributsch*, Berlin, Germany

March 2005 - Sept. 2005 **High school student**, *Hahn-Meitner-Institute, Department of Solar Energy, Group of Dr. M. Kunst and Prof. H. Tributsch*, Berlin, Germany

Teaching experience

March 2010 - July 2010 **Graduate teaching fellow**, *University of Vienna, Faculty of Physics*, Vienna, Austria
Lecture: "Theoretical Physics II: Quantum Mechanics" (Prof. R. Bertlmann)

Oct. 2005 - March 2007 **Organizer of special "Seminar for extraordinarily interested students"**, *supported by Prof. D. Ebert and Prof. M. Müller-Preußker, Humboldt University Berlin*, Germany

Honors and awards

2010	**Performance Scholarship for the academic year 2009/2010** Awarded by the Austrian Federal Minister for Science and Research, granted in recognition of extraordinary academic achievements
2005	**Book Prize 2005 of the German Physical Society (DPG)** Awarded "For excellent accomplishments in the subject of physics"
July 2004 - June 2005	**Honorary member of the German Physical Society (DPG)** Awarded by the German Physical Society in connection with the Student Prize 2004
2004	**Student Prize 2004 of the Physical Society of Berlin (PGzB)** Awarded "For excellent achievements in the A-level in physics"
1997	**First Prize in the category of chamber music of strings** Awarded from the German music competition "Jugend musiziert"

Schools, workshops and internships

Sept. 2010	**DPG-School on Nanophotonics meets Quantum Optics**, *The German Physical Society (DPG), Physikzentrum Bad Honnef*, Germany
Sept. 2010	**Complex Quantum Systems Summer School**, *University of Vienna, Department of Physics*, Vienna, Austria
March 2007	**Four-week research and study visit granted by the Austrian Academy of Sciences**, *Groups of Prof. A. Zeilinger and Prof. R. Bertlmann, Institute for Quantum Optics and Quantum Information, University of Vienna, Vienna, Austria*
Sept. 2006	**Invitation to workshop "Cognitive Science"**, *Research groups of Prof. A. Zeilinger and Prof. R. Bertlmann,* Traunkirchen, Austria

Publications

[1] **Skurrile Quantenwelt**, *Springer-Verlag*, Heidelberg, Germany, 3rd reprint (2006)

[2] **Skurrile Quantenwelt**, *Fischer-Verlag*, Frankfurt, Germany, 1st edition (2007)

[3] **Il bizzarro mondo dei quanti,** *Springer-Verlag Italia*, Milan, Italy, 1st edition (2008)

[4] THẾ GIỚI LƯỢNG TỬ KỲ BÍ , *Tre Publishing House*, Ho Chi Minh City, Vietnam, 2nd edition (2008)

[5] シルヴィアの量子力学 , *Iwanami Shoten Publishing*, Tokyo, Japan, 1st edition (2009)

[6] **Το κορισακι τα κβαντα,** *Alexandria Publications*, Athens, Greece, 1st edition (2010)

Talks

June 2011	**"Narrow-band few photon detection for EIT with Cs" Greenhorn Meeting 2011**, Institute of Laser Physics and Center for Optical Quantum Technologies, Hamburg, Germany
Nov. 11, 2010	**"God doesn't play dice! Quantum physics - future technology or science fiction?"**, *Invitation to public panel discussion,* 7th Faculty of the University of Graz and Club Future of the Bureau of Economy of the City of Graz**,** Austria
March 14, 2007	**Open discussion on the book "Skurrile Quantenwelt"**, *Department of Physics*, University of Vienna, Austria
June 11, 2005	**Public talk on "The photoelectric Effect: From its Discovery to Applications"**, *Lange Nacht der Wissenschaften 2005*, Hahn-Meitner-Institute, Berlin-Wannsee, Germany